

# Uniform Forward-modeling Analysis of Ultracool Dwarfs. II. Atmospheric Properties of 55 Late-T Dwarfs

Zhoujian Zhang (张周健)<sup>1,6</sup>, Michael C. Liu<sup>1</sup>, Mark S. Marley<sup>2,3</sup>, Michael R. Line<sup>4</sup>, and William M. J. Best<sup>5</sup>, Institute for Astronomy, University of Hawaii at Manoa, Honolulu, HI 96822, USA
2 NASA Ames Research Center, Mail Stop 245-3, Moffett Field, CA 94035, USA
3 The University of Arizona, Tucson, AZ 85721, USA
4 School of Earth & Space Exploration, Arizona State University, Tempe, AZ 85287, USA
5 Department of Astronomy, University of Texas at Austin, Austin, TX 78712, USA
Received 2020 August 8; revised 2021 April 29; accepted 2021 May 5; published 2021 November 3

#### **Abstract**

We present a large uniform forward-modeling analysis for 55 late-T (T7-T9) dwarfs, using low-resolution  $(R \approx 50-250)$  near-infrared (1.0-2.5  $\mu$ m) spectra and cloudless Sonora-Bobcat model atmospheres. We derive the objects' effective temperatures, surface gravities, metallicities, radii, masses, and bolometric luminosities using our newly developed Bayesian framework, and use the resulting population properties to test the model atmospheres. We find (1) our objects' fitted metallicities are 0.3–0.4 dex lower than those of nearby stars; (2) their ages derived from spectroscopic parameters are implausibly young (10 Myr-0.4 Gyr); (3) their fitted effective temperatures show a similar spread to empirical temperature scales at a given spectral type but are  $\sim$ 50–200 K hotter for  $\geq$ T8 dwarfs; and (4) their spectroscopically inferred masses are unphysically small (mostly 1–8  $M_{\text{Jup}}$ ). These suggest the Sonora-Bobcat assumptions of cloudless and chemical-equilibrium atmospheres do not adequately reproduce late-T dwarf spectra. We also find a gravity and metallicity dependence of effective temperature as a function of spectral type. Combining the resulting parameter posteriors of our sample, we quantify the degeneracy between the fitted surface gravity and metallicity such that an increase in Z combined with a  $3.4 \times$  increase in logg results in a spectrum that has similar fitted parameters. We note the systematic difference between the late-T dwarf spectra and Sonora-Bobcat models is on average  $\approx$ 2%-4% of the objects' peak J-band fluxes over the 1.0-2.5  $\mu$ m range, implying modeling systematics will exceed measurement uncertainties when analyzing data with *J*-band  $S/N \gtrsim 50$ . Using our large, high-quality sample, we examine the spectral-fitting residuals as a function of wavelength and atmospheric properties to discern how to improve the model assumptions. Our work constitutes the largest analysis of brown dwarf spectra using multimetallicity models and the most systematic examination of ultracool model atmospheres to date.

*Unified Astronomy Thesaurus concepts:* Brown dwarfs (185); T dwarfs (1679); Stellar atmospheres (1584); Exoplanet atmospheres (487)

Supporting material: figure sets

#### 1. Introduction

Characterization of ultracool dwarf spectra is essential to understanding the physical and chemical processes in the atmospheres of brown dwarfs and exoplanets. Such processes govern these objects' appearance and evolution, and the emergent spectra encode signatures of their formation pathways (e.g., Burrows et al. 2001; Fortney et al. 2008; Marley & Robinson 2015). However, spectroscopic analysis of substellar objects can be challenging given the numerous complex processes and interactions in ultracool atmospheres.

As brown dwarfs evolve to cooler effective temperatures, substantial changes in atmospheric chemistry drive the emergence and disappearance of various atomic and molecular spectral features. The transition from M to L spectral type is marked by increasing strength of alkali lines (e.g., Na and K) and metal hydride bands (e.g., FeH and CrH), and the disappearance of TiO and VO due to the formation of titanium-bearing condensates (e.g., CaTiO<sub>3</sub>; Burrows & Sharp 1999; Lodders 2002). During the M/L transition, clouds of iron and silicate grains (e.g., MgSiO<sub>3</sub> and Mg<sub>2</sub>SiO<sub>4</sub>) form

and cause the objects' emergent spectra to become redder toward later-L subtypes (Burrows & Sharp 1999; Marley et al. 2002). The hallmark of the transition from L to T spectral type is the emergence of CH<sub>4</sub> absorption, along with the strengthening of the H<sub>2</sub>O bands. The cool temperatures of the L/T transition ( $T_{\rm eff} \approx 1200\text{--}1400 \text{ K}$ ) apparently lead to cloud patchiness, condensation below the photosphere, and dissipation (e.g., Saumon & Marley 2008; Marley et al. 2010), resulting in brighter J-band emission and bluer J-K colors of early-T dwarfs as compared to late-L dwarfs (e.g., Knapp et al. 2004; Liu et al. 2006; Dupuy & Liu 2012). The transition from T to Y spectral type is defined by the emergence of NH<sub>3</sub> absorption in the near-infrared, along with the formation of new condensates (e.g., Na<sub>2</sub>S, KCl, and H<sub>2</sub>O) given the cold atmosphere temperature ( $\leq 600$  K; Cushing et al. 2011; Morley et al. 2012). An alternative interpretation of the L-T-Y evolution does not rely on clouds but rather on a thermochemical instability (e.g., Tremblin et al. 2015, 2016, 2017, 2019). Such an instability can trigger local compositional convection, drive chemical abundances (e.g., CO/CH<sub>4</sub> and N<sub>2</sub>/NH<sub>3</sub>) out of equilibrium, and reduce the vertical temperature gradient in the atmospheres.

Efforts have been devoted to describing the above complicated processes via models of ultracool atmospheres (e.g.,

<sup>&</sup>lt;sup>6</sup> Visiting Astronomer at the Infrared Telescope Facility, which is operated by the University of Hawaii under contract 80HQTR19D0030 with the National Aeronautics and Space Administration.

Baraffe et al. 1998, 2003; Chabrier et al. 2000; Burrows et al. 2002, 2006; Marley et al. 2002, 2010, 2017; Saumon & Marley 2008; Allard et al. 2012; Morley et al. 2012; Tremblin et al. 2015, 2016; Mollière et al. 2019; Phillips et al. 2020). Characterization of brown dwarfs is commonly conducted by comparing grids of such precomputed, forward models to observations. Synthetic model spectra have been quite successful in predicting the spectral morphology of brown dwarfs and giant planets, but inconsistencies between data and grid models have long been noticed (e.g., Cushing et al. 2008; Stephens et al. 2009; Leggett et al. 2017; Zhang et al. 2020), indicating that the assumptions of these models (e.g., cloud properties, equilibrium chemistry, and radiative convective equilibrium) should be improved. Recently, we have conducted a forward-modeling analysis using cloudless Sonora-Bobcat models (Marley et al. 2017, 2021) for three benchmark late-T dwarfs, HD 3651B, GJ 570D, and Ross 458C (Zhang et al. 2021, referred to as "Paper I" hereinafter). Comparing our spectral-fitting results to those derived from these objects' bolometric luminosities, their primary stars' ages and metallicities, and the Sonora-Bobcat evolutionary models, we identified potential shortcomings of model predictions of these three objects. However, such analysis is hampered by the small census of known benchmarks with high-quality spectroscopy, meaning an insufficient diversity in surface gravity and metallicity at a given effective temperature (especially for  $\leq 1000 \text{ K}$ ).

The atmospheric retrieval technique is an alternative approach for inferring brown dwarf properties, which is not limited to the physical assumptions made by grid models and has the freedom to explore more physical (and unphysical) conditions of ultracool atmospheres by using many more free parameters (e.g., Line et al. 2015, 2017; Burningham et al. 2017; Zalesky et al. 2019; Gonzales et al. 2020). Aiming to find models that almost exactly explain the observed spectra, retrieval can robustly test whether the physical assumptions made within grid models are reasonable. However, when an object has a peculiar spectrum, this data-driven method might converge to atmospheric compositions and thermal structures that are not physically self-consistent (e.g., Zalesky et al. 2019).

Studying large samples of brown dwarfs can help surpass the aforementioned limitations of both forward-modeling and retrieval methods, so that fundamental properties of the ultracool population can be robustly investigated. In addition, forward-modeling analysis of an ensemble of brown dwarfs can uncover the discrepancies between data and models, providing feedback about the strength and weakness of current modeling. Thanks to the wide coverage and depth of imaging sky surveys, including Pan-STARRS1 (Chambers et al. 2016), the Two Micron All Sky Survey (2MASS; Skrutskie et al. 2006), the UKIRT Infrared Deep Sky Survey (UKIDSS; Lawrence et al. 2007), and the Wide-field Infrared Survey Explorer (WISE, Wright et al. 2010; CatWISE, Eisenhardt et al. 2020; Marocco et al. 2021), we now have a large census of brown dwarfs in the field and in young associations (e.g., Kirkpatrick et al. 1999, 2011; Luhman 2006; Lodieu et al. 2007; Burningham et al. 2008, 2010b, 2013; Luhman et al. 2009; Luhman & Mamajek 2012; Lodieu 2013; Best et al. 2015, 2017, 2018, 2020a; Gagné et al. 2018; Zhang et al. 2018a; Meisner et al. 2020). Most notably, the sample of ultracool dwarfs with nearinfrared spectra is large (≥20 objects in each spectral subtype from M6 to T8; e.g., Burgasser 2014; Filippazzo et al. 2016;

Manjavacas et al. 2019), enabling ensemble analyses instead of the more common single-object studies.

In this paper, we apply our forward-modeling framework constructed and validated in Paper I to 55 T7-T9 dwarfs  $(T_{\rm eff} \approx 600-1200 \text{ K})$ . Late-T dwarfs likely lack optically thick clouds in their near-infrared photospheres (though optically thin, sulfide clouds might exist there; e.g., Morley et al. 2012). Therefore, choosing late-T dwarfs helps simplify the model parameter space and can validate cloud-free models, which serve as the starting point for the more complex cloudy models. We compare our objects' low-resolution near-infrared spectra to cloudless Sonora-Bobcat models with both solar and nonsolar metallicities. Our forward-modeling analysis uses the Bayesian framework Starfish (developed by Czekala et al. 2015 and updated by Gully-Santiago et al. 2017; see Paper I), which accounts for uncertainties from model interpolation, as well as correlated (data-model) residuals due to instrumental effects and modeling systematics, thereby providing robust physical parameters and more realistic error estimates than the traditional ( $\chi^2$ -based) methods adopted in most previous work. Our work is the largest analysis of brown dwarf spectra using multimetallicity models and altogether the most systematic test of any set of ultracool model atmospheres

We aim to investigate the physical properties of late-T dwarfs and examine the model atmospheres through detailed comparisons between data and models. We start with a description of our sample (Section 2) and present our methodology and the results of the forward-modeling analysis (Section 3). We identify known and candidate binaries in our sample and exclude them from our subsequent analysis (Section 4). We then study the inferred atmospheric properties of late-T dwarfs (Section 5) and use them to investigate the performance of the cloudless Sonora–Bobcat models (Section 6). Finally, we provide a summary and a brief discussion of further work (Section 7).

#### 2. Observations

## 2.1. Sample of T7-T9 Dwarfs

We construct our sample of late-T dwarfs by using the catalog of ultracool dwarfs by Best et al. (2018) and selecting all T7–T9 objects with prism-mode ( $R \approx 50-250$ ) spectra taken from the SpeX spectrograph (Rayner et al. 2003) mounted on the NASA Infrared Telescope Facility (IRTF). These lowresolution spectra are from our own observations (Section 2.2), the SpeX Prism Library (Burgasser 2014; Burgasser & Splat Development Team 2017), and the literature (e.g., Burgasser et al. 2004, 2006a, 2010a; Best et al. 2015), leading to a total of 55 late-T dwarfs. In this sample, 54 objects have parallaxes (van Leeuwen 2007; Burgasser et al. 2008b; Dupuy & Liu 2012; Leggett et al. 2012; Gaia Collaboration et al. 2016b, 2016a, 2018; Kirkpatrick et al. 2019; Best et al. 2020b) and the only remaining object, WISE J024512.62-345047.8 (WISE 0245-3450, T8; Mace et al. 2013a), is part of our astrometric monitoring program. Four objects in our sample are co-moving companions to either stars or brown dwarfs: HD 3651B (T7.5; Mugrauer et al. 2006; Luhman et al. 2007), GJ 570D (T7.5; Burgasser et al. 2000), Ross 458C (T8; Goldman et al. 2010; Scholz 2010b), and ULAS J141623.94 +134836.3 (ULAS 1416+1348, T7.5; Burningham et al. 2010a; Scholz 2010a), for which we adopt the parallaxes of their primary hosts from Gaia DR2 (Gaia Collaboration et al. 2016b, 2018). The first three benchmark objects have been analyzed in Paper I and here we simply keep them in our sample. Our sample contains 90% of the known T7–T9 dwarfs that have distances  $\leq$ 25 pc, *J*-band magnitudes  $\leq$ 17.5 mag, and declinations from  $-40^{\circ}$  to  $+70^{\circ}$ . Information about our sample's spectroscopy, astrometry, and photometry is listed in Tables 1, 2, and 3, respectively.

## 2.2. IRTF/SpeX Spectroscopy

We obtain near-infrared spectra of 16 T7–T9 dwarfs in our sample using IRTF (Table 1). We use SpeX in prism mode with either the 0."5 slit ( $R \approx 80$ –250) or the 0."8 slit ( $R \approx 50$ –160). For each target, we take at least six exposures in a standard ABBA pattern and contemporaneously observe a nearby A0V standard star within 0.1 airmass for telluric correction. We reduce the data using version 4.1 of the Spextool software package (Cushing et al. 2004). Our resulting spectra are reported with vacuum wavelengths and have typical S/N  $\approx 50$  per pixel in the J band.

Combining all available IRTF/SpeX spectra, we find 42 objects in our sample have spectra observed using the 0.75 slit and 15 objects using the 0.78 slit, with two objects having spectra observed using both slit widths. Therefore, we have in total 57 near-infrared spectra for 55 objects. We flux-calibrate all spectra using the objects'  $H_{\rm MKO}$  magnitudes, which are either observed (e.g., Knapp et al. 2004; Lawrence et al. 2012; Kirkpatrick et al. 2019) or synthesized from other bands by Best et al. (2021). The WFCAM H-band filter and the corresponding zero-point flux are from Hewett et al. (2006) and Lawrence et al. (2007), respectively.

## 3. Forward-modeling Analysis

#### 3.1. Methodology

In Paper I, we constructed and validated a forward-modeling framework using the Bayesian inference tool Starfish (Czekala et al. 2015; Gully-Santiago et al. 2017) and the Sonora–Bobcat models (Marley et al. 2017; Marley et al. 2021, submitted), which assume cloudless and chemical-equilibrium atmospheres. Our framework is customized to the parameter space relevant to late-T dwarfs—[600, 1200] K in effective temperature  $T_{\rm eff}$ , [3.25, 5.5] dex in logarithmic surface gravity logg, and [-0.5, +0.5] dex in bulk metallicity Z (before removal of any species by condensation)—and to near-infrared (0.8–2.5  $\mu$ m) spectra taken using the prism mode of IRTF/SpeX. Here we summarize our methods and refer readers to Paper I and Czekala et al. (2015) for more details.

We start our analysis by training Starfish's spectral emulator to generate a probability distribution of model spectra for an arbitrary set of grid parameters. Starfish propagates the resulting interpolation uncertainties into the inferred posteriors and is thereby fundamentally different from linear interpolation adopted by traditional ( $\chi^2$ -based) forward-modeling analyses (e.g., Rice et al. 2010; Zhang et al. 2020). We first trim the cloudless Sonora–Bobcat models over the aforementioned grid parameter space and wavelength range, and then downgrade

their spectral resolution using two different Gaussian kernels, which correspond to the 0.75 slit and the 0.88 slit of SpeX. The convolution also accounts for the wavelength-dependent spectral resolution of the SpeX prism mode (Rayner et al. 2003). We conduct principal component analysis and train Gaussian processes on these processed models, leading to spectral emulators tailored to spectra obtained with the 0.75 and 0.78 slits.

We determine six physical parameters: effective temperature  $T_{\rm eff}$ , logarithmic surface gravity logg, metallicity Z, radial velocity  $v_r$ , projected rotational velocity  $v\sin i$ , and logarithmic solid angle  $\log \Omega = \log(R/d)^2$ , where i, R, and d are the inclination of the rotation axis, the radius, and the distance, respectively. As in Paper I, we assume uniform priors of [600, 1200] K in  $T_{\text{eff}}$ , [3.25, 5.5] dex in logg, [-0.5, +0.5] dex in Z,  $(-\infty, +\infty)$  for both  $v_r$  and  $\log\Omega$ , and  $[0, v_{max}]$  for  $v\sin i$ . We determine  $v_{\text{max}}$  using the objects' distances and fitted  $\{\log g, \log \Omega\}$  in each step of the spectral-fitting process by assuming the rotationally induced oblateness is within the stability limit. For the only object in our sample (WISE 0245-3450) without a parallax, we use the theoretical relation between the oblateness and the equatorial rotational velocity based on the cloudless Sonora-Bobcat models (see Figure 1) and adopt  $v_{\text{max}} = 300 \text{ km s}^{-1}$ .

We also determine three hyperparameters  $\{a_N, a_G, \ell\}$  as part of our spectral-fitting process. These characterize the final covariance matrix, which contains both diagonal and off-diagonal components. The latter account for correlated data —model residuals due to instrumental effects and modeling systematics, leading to more realistic error estimates than a covariance matrix with only diagonal components. We adopt the same hyperparameter priors as in Paper I, but we assume a uniform prior of [425,  $1115 \times 5$ ] km s<sup>-1</sup> in  $\ell$  for the 0.18 spectra in our sample. This is slightly different from the [820,  $1840 \times 5$ ] km s<sup>-1</sup> we use for 0.15 spectra, given the different instrumental line spread functions (LSFs) for these two slit widths (see Appendix of Paper I).

We use emcee (Foreman-Mackey et al. 2013) to fit our objects' 1.0–2.5  $\mu$ m spectra with 48 walkers. We terminate the Markov Chain Monte Carlo (MCMC) fitting process after 10<sup>5</sup> iterations, since such a number of iterations exceeds 50 times the autocorrelation length of all the fitted parameters. To complete our forward-modeling analysis, we add the following systematic uncertainties into the resulting parameter posteriors: 20 K in  $T_{\text{eff}}$ , 0.2 dex in logg, 0.12 dex in Z, 180 km s<sup>-1</sup> in  $v_{\text{r}}$ ,  $40 \, \mathrm{km \, s^{-1}}$  in  $v \mathrm{sin} i$ , and  $[0.05^2 + (0.4 \sigma_{H_{\mathrm{MKO}}})^2]^{1/2}$  dex in  $\log \Omega$ , where  $\sigma_{H_{\mathrm{MKO}}}$  is the H-band magnitude uncertainty. These systematic errors were determined in Paper I by (1) fitting the original Sonora-Bobcat model atmospheres themselves using our forward-modeling framework to quantify the uncertainties introduced by Starfish's spectral emulator, (2) incorporating the uncertainty in the wavelength calibration of the SpeX prism data into the systematics of  $v_r$ , and (3) incorporating the uncertainty in the flux calibration of the spectra (due to H-band magnitude errors) into the systematics of  $log\Omega$ . We note all these added uncertainties are smaller than or comparable to the formal fitting errors of the physical parameters (see Table 6).

In addition, we flux-calibrate the objects' spectra using the H-band magnitudes in this work, and conducting this process using photometry in different bands will alter our resulting  $\log \Omega$  posteriors (e.g., Figure 8 of Line et al. 2015). Each late-T dwarf in our sample has similar photometric uncertainties

The five late-T dwarfs with such properties not included in our sample are Gl 229B (T7; Nakajima et al. 1995), WISEPA J052844.51–330823.9 (T7; Kirkpatrick et al. 2011), WISE J214706.78–102924.0 (T7.5; Mace et al. 2013a), WISEPA J085716.25+560407.6 (T8; Kirkpatrick et al. 2011), and WISEPA J143602.19–181421.8 (T8; Kirkpatrick et al. 2011).

Table 1Sample of T7–T9 Dwarfs: Spectroscopy

				IRTI	F/SpeX Spectra			Referen	ices	
Object	Type <sup>a</sup>	SpT	Slit	J-band S/N <sup>b</sup>	Obs. Date <sup>c</sup>	A0V Star <sup>c</sup>	Discovery	Type	SpT	Spectra
	_		(")		(UT)					
HD 3651B	C	T7.5	0.5	73		•••	10	10	12	11
WISE J004024.88+090054.8		T7	0.5	80	•••	•••	34	•••	34	38
WISE J004945.61+215120.0		T8.5	0.5	78			34	•••	34	38
234 4 55 400501004 2222402		ma.	0.8	35	2012 Jan 20	HD 9711	34	•••	34	40
2MASS J00501994–3322402		T7	0.5	61			5	•••	6	8
WISEPA J012333.21+414203.9		T7	0.8	60	2017 Oct 22	HD 1561	25	•••	25	40
WISEPC J022322.39–293258.1		T7.5	0.5	50			25	•••	25	38
WISE J024124.73–365328.0		T7	0.8	57	2017 Nov 15	HD 18546	29	•••	39	40
WISE J024512.62–345047.8		T8	0.5	27	•••		34	•••	34	38
PSO J043.5395+02.3995		T8	0.5	107	•••	•••	26, 28	•••	26	38
WISE J032547.72+083118.2		T7	0.5	66	•••	•••	34	•••	34	38
2MASSI J0415195-093506	В	T8 T8.5	0.5	176 24	•••	•••	3 27	24	6 25	38
WISEPA 1050002 05 122242 2	В	18.5 T8	0.5	13			25	24	25 25	38
WISEPA J050003.05-122343.2			0.5					•••		38
WISE J052126.29+102528.4		T7.5	0.8	79 40	2017 Mar 13	HD 35036	33	•••	33	40
UGPS J052127.27+364048.6		T8.5	0.8	40	2017 Oct 21	HD 31069	22	•••	22	40
WISE J061437.73+095135.0		T7	0.8	94	2017 Nov 2	HD 41076	34	•••	34	40
WISEPA J062309.94-045624.6		T8	0.5	14	•••	•••	25	•••	25	38
UGPS J072227.51-054031.2		T9	0.5	79	•••	•••	19	•••	23	38
2MASSI J0727182+171001		T7	0.5	106	•••	•••	3	•••	6	8
2MASS J07290002–3954043		T8 pec	0.5	52	•••	•••	13	•••	13	13
2MASS J09393548-2448279		T8	0.5	50	•••	•••	5	•••	6	8
ULAS J102940.52+093514.6	D.O.	T8	0.5	45	•••	•••	32	•••	32	38
WISE J103907.73–160002.9	В?	T7.5	0.5	29	•••	•••	34	•••	34	38
WISE J105257.95–194250.2		T7.5	0.5	67	•••	•••	35 5	•••	35	38
2MASS J11145133–2618235		T7.5	0.5	29	•••	•••	34	•••	6	8
WISE J112438.12–042149.7		T7	0.5	81 31	•••	•••		•••	34	38
2MASSI J1217110-031113		T7.5 T7	0.5	21			1 35		6	8
WISE J125448.52-072828.4		T7	0.5	33		•••	34		35 34	38
WISE J125715.90+400854.2	С	T8	0.5	33 43			34 18			38
Ross 458C	C	T8	0.5	43 27	2015 Jul 7	HD 116960	25	18	23 25	40
WISEPA J132233.66–234017.1	С	(sd) T7.5	0.5 0.5	48		•••			23 14	38 38
ULAS J141623.94+134836.3	C	(su) 17.3 T7		39		•••	17, 21 25	17, 21	25	38
WISEPC J145715.03+581510.2 GJ 570D	С	T7.5	0.5 0.5	39 37		•••	23	2	6	36 4
PSO J224.3820+47.4057	C	T7	0.8	40			37		37	37
SDSS J150411.63+102718.4	В?	T7	0.8	49	2017 May 12	HD 132072	9		9	40
2MASSI J1553022+153236	В	T7	0.8	141	2017 May 12	HD 132072	3	7	6	16
SDSS J162838.77+230821.1	ь	T7	0.3	53		•••	9		9	38
WISEPA J165311.05+444423.9		T8	0.8	33			25		25	38
WISEPA J171104.60+350036.8	В	T8	0.5	20			25	31	25	38
WISEFA J1/1104.00+330030.8	ь	10	0.3	34			25	31	25	31
WISEPA J174124.26+255319.5		Т9	0.8	106	2017 Mar 15	HD 165029	25, 28		25	40
WISE J180901.07+383805.4		T7.5	0.8	27	2017 Iviai 13 	HD 103029	30		34	38
			0.5				2.5		34	40
WISE J181329.40+283533.3 WISEPA J185215.78+353716.3		T8 T7	0.5	46 115	2017 Jun 27 2011 Apr 20	HD 174567 HD 165029	34 25		25	40
WISEPA J195905.66–333833.7		T8	0.5	38	2017 Apr 20 2017 Jun 13	HD 194982	25		25	40
WISE J200050.19+362950.1		T8	0.5	67	2017 Jun 13 2017 Jun 13	HD 191225	36		36	40
WISEPC J215751.38+265931.4		T7	0.8	70	2017 Jul 13 2017 Jul 10	HD 210290	25		25	40
WISEPC J213/31.38+203931.4 WISEPC J220922.10-273439.5		T7	0.8	64	2017 Jul 10 2017 Jul 19	HD 202025	25 25		25 25	40
WISEPC J220922.10-273439.5 WISEPC J221354.69+091139.4		T7	0.5	74	2017 Jul 19 	HD 202023	25		25	38
WISEPC J222623.05+044003.9		T8	0.5	69			25 25		25 25	38
WISEPC J222523.03+044003.9 WISEPC J225540.74-311841.8		T8	0.5	43			25 25		25 25	38
WISEPC J225340.74–311841.8 WISEPC J231939.13–184404.3		T7.5	0.5				25 25		25 25	38
ULAS J232123.79+135454.9		T7.5	0.3	26 45	2017 Jul 19	 HD 210501	20		15	40
WISEPC J234026.62-074507.2	В?	17.5 T7	0.8	43 99	2017 Jul 19 	HD 210501	20 25		25	38
	D!									
WISEPC J234841.10-102844.4		T7	0.5	71	•••	•••	25	•••	25	38

#### Notes

References. (1) Burgasser et al. (1999), (2) Burgasser et al. (2000), (3) Burgasser et al. (2002), (4) Burgasser et al. (2004), (5) Tinney et al. (2005), (6) Burgasser et al. (2006b), (7) Burgasser et al. (2006c), (8) Burgasser et al. (2006a), (9) Chiu et al. (2006), (10) Mugrauer et al. (2006), (11) Burgasser (2007), (12) Luhman et al. (2007), (13) Looper et al. (2007), (14) Burgasser et al. (2010b), (15) Burmingham et al. (2010b), (16) Burgasser et al. (2010a), (17) Burmingham et al. (2010a), (18) Goldman et al. (2010), (19) Lucas et al. (2010), (20) Scholz (2010b), (21) Scholz (2010a), (22) Burmingham et al. (2011), (23) Cushing et al. (2011), (24) Gelino et al. (2011), (25) Kirkpatrick et al. (2011), (26) Liu et al. (2011a), (27) Mainzer et al. (2011), (28) Scholz et al. (2011), (29) Kirkpatrick et al. (2012), (30) Luhman et al. (2012), (31) Liu et al. (2012), (32) Burmingham et al. (2013), (33) Bihain et al. (2013), (34) Mace et al. (2013a), (35) Thompson et al. (2013), (36) Cushing et al. (2014), (37) Best et al. (2015), (38) Burgasser & Splat Development Team (2017), (39) Tinney et al. (2018), and (40) this work.

a "B": resolved binaries; "B?": binarity likely but not confirmed (Section 4.2); "C": companions to stars or brown dwarfs. The remaining objects are single field dwarfs.

b Signal-to-noise ratio around the *J*-band peak (1.2–1.3  $\mu$ m) of the object's spectra.

<sup>&</sup>lt;sup>c</sup> For spectra taken from our own observations, we show the observation date and the A0V telluric standard star.

Table 2 Sample of T7-T9 Dwarfs: Astrometry

Object	Type <sup>a</sup>	SpT	R.A. <sup>b</sup> (hh:mm:ss.ss)	Decl.b (dd:mm:ss.s)	$\mu_{\alpha}\cos\delta$ (mas yr <sup>-1</sup> )	$\mu_{\delta}$ (mas yr $^{-1}$ )	Parallax (mas)	References
IID 2651D	С	T7.5						( 7
HD 3651B WISE J004024.88+090054.8	C	17.3 T7	00:39:18.91 00:40:24.89	-21:15:16.8 -09:00:54.5	$-462.06 \pm 0.11$ $-53.90 \pm 2.80$	$-369.81 \pm 0.06$ $-62.60 \pm 2.30$	$89.79 \pm 0.06$ $71.40 \pm 2.70$	6, 7 9
WISE J004024.88+090034.8 WISE J004945.61+215120.0		T8.5	00:49:45.65	-09.00.34.3 -21:51:19.7	$-33.90 \pm 2.80$ $-483.20 \pm 1.40$	$-62.60 \pm 2.30$ $-46.50 \pm 1.40$	$139.90 \pm 2.50$	8
2MASS J00501994–3322402		T7	00:50:21.05	-21.31.19.7 $-33:22:28.9$	$-483.20 \pm 1.40$ $1150.50 \pm 2.20$	$-40.30 \pm 1.40$ $939.10 \pm 2.10$	$94.60 \pm 2.40$	3
		T7	01:23:33.25	-33.22.28.9 $-41:42:03.9$	$601.10 \pm 1.30$	$88.80 \pm 1.30$	$39.40 \pm 2.40$ $39.40 \pm 2.40$	9
WISEPA J012333.21+414203.9 WISEPC J022322.39-293258.1		T7.5	02:23:22.38	-41:42:03.9 -29:32:57.3	$780.20 \pm 1.10$	$-535.10 \pm 1.50$	$80.70 \pm 2.60$	8
WISE J024124.73–365328.0		17.3 T7	02:41:24.75	-29:32:37.3 -36:53:28.1	$780.20 \pm 1.10$ $242.00 \pm 1.50$	$-333.10 \pm 1.30$ $148.40 \pm 1.40$	$52.40 \pm 2.70$	8
		T8	02:41:24.73	-30:33:28.1 $-34:50:47.8$	242.00 ± 1.30 	146.40 ± 1.40 	32.40 ± 2.70 	···
WISE J024512.62–345047.8		T8					$146.10 \pm 1.50$	
PSO J043.5395+02.3995		18 T7	02:54:09.56 03:25:47.73	-02:23:58.6 $-08:31:18.2$	$2562.61 \pm 0.15$ $116.20 \pm 1.80$	$221.95 \pm 1.34$ $-38.10 \pm 1.70$	$78.50 \pm 3.00$	8 8
WISE J032547.72+083118.2				-08:31:18.2 -09:35:00.4		$-38.10 \pm 1.70$ $535.90 \pm 1.20$		
2MASSI J0415195-093506	ъ	T8	04:15:21.27		$2214.30 \pm 1.20$		$175.20 \pm 1.70$	3 8
WISEPA 1050003 05 122242 2	В	T8.5	04:58:53.91	-64:34:52.6	$207.70 \pm 1.20$	$291.20 \pm 1.20$	$109.20 \pm 3.60$	
WISEPA J050003.05–122343.2		T8	05:00:03.04	-12:23:43.2	$-533.70 \pm 1.70$	$490.50 \pm 1.80$	$84.60 \pm 2.20$	9
WISE J052126.29+102528.4		T7.5	05:21:26.31	-10:25:28.4	$215.50 \pm 5.60$	$-418.30 \pm 2.80$	$141.50 \pm 5.10$	9
UGPS J052127.27+364048.6		T8.5	05:21:27.42	-36:40:43.6	$569.00 \pm 0.90$	$-1511.00 \pm 1.00$	$122.20 \pm 1.60$	8
WISE J061437.73+095135.0		T7	06:14:37.75	-09:51:35.2	$387.50 \pm 1.70$	$-156.30 \pm 1.50$	$56.80 \pm 2.00$	9
WISEPA J062309.94-045624.6		T8	06:23:09.93	-04:56:24.5	$-906.30 \pm 1.80$	$168.80 \pm 1.60$	$86.50 \pm 1.70$	9
UGPS J072227.51-054031.2		T9	07:22:27.28	-05:40:29.8	$-904.14 \pm 1.71$	$352.03 \pm 1.21$	$242.80 \pm 2.40$	5
2MASSI J0727182+171001		T7	07:27:19.16	-17:09:51.3	$1045.50 \pm 1.10$	$-763.70 \pm 1.00$	$112.50 \pm 0.90$	3
2MASS J07290002–3954043		T8 pec	07:28:59.50	-39:53:45.4	$-566.60 \pm 5.30$	$1643.40 \pm 5.50$	$126.30 \pm 8.30$	4
2MASS J09393548-2448279		T8	09:39:35.93	-24:48:39.0	$573.40 \pm 2.30$	$-1044.70 \pm 2.50$	$187.30 \pm 4.60$	2
ULAS J102940.52+093514.6		T8	10:29:40.52	-09:35:14.1	$-419.40 \pm 2.00$	$-142.60 \pm 1.80$	$68.50 \pm 1.70$	9
WISE J103907.73–160002.9	В?	T7.5	10:39:07.74	-16:00:03.0	$-197.60 \pm 2.20$	$-120.30 \pm 2.30$	$45.20 \pm 1.90$	9
WISE J105257.95–194250.2		T7.5	10:52:57.95	-19:42:50.2	$317.90 \pm 2.20$	$-314.90 \pm 2.00$	$67.90 \pm 2.20$	9
2MASS J11145133–2618235		T7.5	11:14:48.75	-26:18:27.9	$-3021.50 \pm 1.80$	$-389.50 \pm 2.10$	$179.20 \pm 1.40$	3
WISE J112438.12-042149.7		T7	11:24:38.11	-04:21:49.6	$-569.10 \pm 2.40$	$68.90 \pm 3.00$	$57.50 \pm 3.40$	9
2MASSI J1217110-031113		T7.5	12:17:10.28	-03:11:12.2	$-1054.39 \pm 1.70$	$75.58 \pm 1.84$	$91.70 \pm 2.20$	1, 8
WISE J125448.52-072828.4		T7	12:54:48.51	-07:28:28.3	$1.40 \pm 2.70$	$-133.80 \pm 2.90$	$41.30 \pm 2.70$	9
WISE J125715.90+400854.2		T7	12:57:15.92	-40:08:54.2	$294.90 \pm 1.60$	$167.90 \pm 1.40$	$57.10 \pm 1.80$	9
Ross 458C	C	T8	13:00:41.64	-12:21:14.6	$-632.15 \pm 0.50$	$-36.02 \pm 0.19$	$86.86 \pm 0.15$	6, 7
WISEPA J132233.66–234017.1		T8	13:22:33.63	-23:40:17.1	$-348.31 \pm 1.47$	$391.62 \pm 1.57$	$77.50 \pm 4.20$	8
ULAS J141623.94+134836.3	C	(sd) T7.5	14:16:23.97	-13:48:36.1	$85.69 \pm 0.69$	$129.07 \pm 0.47$	$107.56 \pm 0.30$	6, 7
WISEPC J145715.03+581510.2		T7	14:57:15.02	-58:15:10.2	$-488.60 \pm 4.90$	$-65.80 \pm 4.90$	$46.70 \pm 5.70$	9
GJ 570D	C	T7.5	14:57:15.84	-21:22:08.1	$1031.40 \pm 0.17$	$-1723.65 \pm 0.13$	$170.01 \pm 0.09$	6, 7
PSO J224.3820+47.4057		T7	14:57:31.68	-47:24:20.2	$139.80 \pm 3.00$	$-84.50 \pm 2.30$	$49.50 \pm 3.00$	9
SDSS J150411.63+102718.4	B?	T7	15:04:11.81	-10:27:15.4	$373.60 \pm 1.90$	$-369.20 \pm 2.10$	$46.10 \pm 1.50$	3
2MASSI J1553022+153236	В	T7	15:53:01.93	-15:32:38.8	$-385.90 \pm 0.70$	$166.20 \pm 0.90$	$75.10 \pm 0.90$	3
SDSS J162838.77+230821.1		T7	16:28:38.99	-23:08:17.9	$412.30 \pm 0.80$	$-443.00 \pm 0.70$	$75.10 \pm 0.90$	3
WISEPA J165311.05+444423.9		T8	16:53:11.03	-44:44:22.7	$-76.00 \pm 1.90$	$-398.20 \pm 2.40$	$75.70 \pm 1.90$	9
WISEPA J171104.60+350036.8	В	T8	17:11:04.59	-35:00:36.8	$-156.30 \pm 1.10$	$-71.20 \pm 1.20$	$40.30 \pm 2.40$	8
WISEPA J174124.26+255319.5		T9	17:41:24.23	-25:53:19.2	$-505.34 \pm 1.11$	$-1472.61 \pm 1.28$	$214.30 \pm 2.80$	8
WISE J180901.07+383805.4		T7.5	18:09:01.07	-38:38:05.2	$-590.70 \pm 2.60$	$-506.70 \pm 2.30$	$52.30 \pm 2.30$	9
WISE J181329.40+283533.3		T8	18:13:29.40	-28:35:33.3	$-208.90 \pm 2.10$	$-468.10 \pm 2.90$	$73.60\pm2.00$	9
WISEPA J185215.78+353716.3		T7	18:52:15.82	-35:37:16.2	$254.40 \pm 3.00$	$-288.00 \pm 3.00$	$66.40 \pm 2.90$	9
WISEPA J195905.66-333833.7		T8	19:59:05.65	-33:38:33.8	$-8.60 \pm 1.00$	$-193.20 \pm 1.10$	$85.30 \pm 2.20$	8
WISE J200050.19+362950.1		T8	20:00:50.19	-36:29:50.1	$2.20 \pm 3.30$	$368.30 \pm 4.20$	$131.20 \pm 2.90$	9
WISEPC J215751.38+265931.4		T7	21:57:51.35	-26:59:31.3	$65.80 \pm 1.30$	$-100.50 \pm 1.60$	$62.80 \pm 2.20$	9
WISEPC J220922.10-273439.5		T7	22:09:22.09	-27:34:39.9	$-765.10 \pm 2.00$	$-440.90 \pm 2.20$	$72.40 \pm 3.80$	9
WISEPC J221354.69+091139.4		T7	22:13:54.70	-09:11:39.4	$-116.20 \pm 1.50$	$-35.40 \pm 1.80$	$52.10\pm3.10$	9
WISEPC J222623.05+044003.9		T8	22:26:23.06	-04:40:03.3	$-283.17 \pm 3.83$	$-463.55 \pm 5.08$	$54.40 \pm 5.90$	8
WISEPC J225540.74-311841.8		T8	22:55:40.76	-31:18:42.0	$300.20 \pm 1.50$	$-162.10 \pm 2.20$	$70.70 \pm 4.20$	8
WISEPC J231939.13-184404.3		T7.5	23:19:39.15	-18:44:04.4	$74.00 \pm 1.40$	$131.20 \pm 1.40$	$85.10 \pm 3.10$	9
ULAS J232123.79+135454.9		T7.5	23:21:23.83	-13:54:53.3	$78.70 \pm 1.20$	$-561.60 \pm 1.40$	$83.60 \pm 2.40$	8
WISEPC J234026.62-074507.2	B?	T7	23:40:26.62	-07:45:08.5	$152.80\pm0.95$	$-250.12 \pm 1.25$	$47.80 \pm 3.10$	8
WISEPC J234841.10-102844.4		T7	23:48:41.12	-10:28:44.1	$620.80 \pm 2.10$	$146.20 \pm 1.90$	$67.60 \pm 3.80$	9

## Notes.

References. (1) Tinney et al. (2003), (2) Burgasser et al. (2008b), (3) Dupuy & Liu (2012), (4) Faherty et al. (2012), (5) Leggett et al. (2012), (6) Gaia Collaboration et al. (2016b), (7) Gaia Collaboration et al. (2018), (8) Kirkpatrick et al. (2019), and (9) Best et al. (2020b).

a "B": resolved binaries; "B?": binarity likely but not confirmed (Section 4.2); "C": companions to stars or brown dwarfs. The remaining objects are single field dwarfs.

b Coordinates are provided at epoch J2000 with equinox J2000.

Table 3
Sample of T7–T9 Dwarfs: Photometry

				Near-inf	rared MKO Photo	metry		Al	WISE Photometr	<u>y</u>	Spitz	er/IRAC Photom	etry
Object	Type <sup>a</sup>	SpT	Y <sub>MKO</sub> (mag)	$J_{ m MKO}$ (mag)	H <sub>MKO</sub> (mag)	K <sub>MKO</sub> (mag)	References	W1 (mag)	W2 (mag)	References	[3.6] (mag)	[4.5] (mag)	References
HD 3651B	С	T7.5	$17.12 \pm 0.06$	$16.16 \pm 0.03$	$16.68 \pm 0.04$	$16.87 \pm 0.05$	4, 26	•••			$15.38 \pm 0.04$	$13.62 \pm 0.02$	8
VISE J004024.88+090054.8		T7	$17.15 \pm 0.02$	$16.13 \pm 0.01$	$16.56 \pm 0.02$	$16.55 \pm 0.05$	12	$15.99 \pm 0.06$	$13.83 \pm 0.05$	19	$15.07 \pm 0.02$	$13.76 \pm 0.02$	17
WISE J004945.61+215120.0		T8.5	$17.29 \pm 0.17$	$16.44 \pm 0.16$	$16.72 \pm 0.02$	$16.80 \pm 0.17$	24, 26	$15.92 \pm 0.06$	$13.03 \pm 0.03$	19	$15.01 \pm 0.02$	$13.04 \pm 0.02$	17
MASS J00501994-3322402		T7	$16.85 \pm 0.10$	$15.65 \pm 0.10$	$16.04 \pm 0.10$	$15.91 \pm 0.10$	8	$15.60 \pm 0.04$	$13.58 \pm 0.03$	19	$14.87 \pm 0.02$	$13.59 \pm 0.02$	24
WISEPA J012333.21+414203.9		T7	$18.10 \pm 0.05$	$16.99 \pm 0.02$	$17.25 \pm 0.05$	$17.25 \pm 0.06$	25, 26	$16.84 \pm 0.08$	$14.95 \pm 0.07$	19	$16.12 \pm 0.03$	$14.84 \pm 0.02$	24
WISEPC J022322.39-293258.1		T7.5	$18.08 \pm 0.07$	$17.10 \pm 0.05$	$17.30 \pm 0.11$	$17.59 \pm 0.08$	10, 26	$16.87 \pm 0.08$	$14.02 \pm 0.04$	19	$15.81 \pm 0.03$	$14.01 \pm 0.02$	10
WISE J024124.73-365328.0b		T7	$17.73 \pm 0.05$	$16.72 \pm 0.01$	$17.04 \pm 0.07$	$17.27 \pm 0.05$	16, 24, 27	$16.86 \pm 0.08$	$14.35 \pm 0.04$	19	$15.74 \pm 0.03$	$14.35 \pm 0.02$	24
WISE J024512.62-345047.8		Т8	$18.65 \pm 0.11$	$17.77 \pm 0.09$	$18.27 \pm 0.10$	$18.05 \pm 0.11$	17, 26	$17.03 \pm 0.10$	$14.50 \pm 0.05$	19	$16.05 \pm 0.03$	$14.59 \pm 0.02$	17
PSO J043.5395+02.3995		Т8	$17.00 \pm 0.01$	$15.92 \pm 0.01$	$16.29 \pm 0.02$	$16.73 \pm 0.05$	12	$15.81 \pm 0.05$	$12.76 \pm 0.03$	19	$14.69 \pm 0.02$	$12.70 \pm 0.02$	10
VISE J032547.72+083118.2		T7	$17.14 \pm 0.09$	$16.29 \pm 0.07$	$16.19 \pm 0.08$	$16.39 \pm 0.09$	26	$15.35 \pm 0.04$	$13.53 \pm 0.03$	19	$14.70 \pm 0.02$	$13.59 \pm 0.02$	17
2MASSI J0415195-093506		Т8	$16.39 \pm 0.06$	$15.32 \pm 0.03$	$15.70 \pm 0.03$	$15.83 \pm 0.03$	2, 26	$15.14 \pm 0.04$	$12.29 \pm 0.03$	19	$14.26 \pm 0.02$	$12.37 \pm 0.02$	24
VISEPA J045853.89+643452.9	В	T8.5	$18.02 \pm 0.09$	$17.13 \pm 0.07$	$17.45 \pm 0.11$	$17.74 \pm 0.10$	9, 26	$16.44 \pm 0.07$	$13.02 \pm 0.03$	19	$15.08 \pm 0.02$	$12.98 \pm 0.02$	10
WISEPA J050003.05-122343.2	ь	T8	$18.69 \pm 0.07$	$17.88 \pm 0.02$	$18.13 \pm 0.12$	$18.07 \pm 0.08$	12, 26	$17.45 \pm 0.15$	$13.98 \pm 0.04$	19	$15.95 \pm 0.03$	$14.00 \pm 0.02$	10
VISE J052126.29+102528.4		T7.5	$15.71 \pm 0.05$	$14.87 \pm 0.02$	$15.27 \pm 0.05$	$15.00 \pm 0.05$	25, 26	$14.11 \pm 0.03$	$12.29 \pm 0.02$	19			
JGPS J052127.27+364048.6b		T8.5	$18.08 \pm 0.05$	$16.94 \pm 0.02$	$17.28 \pm 0.04$	$17.32 \pm 0.09$	13, 27	$14.40 \pm 0.03$	$13.00 \pm 0.02$	19	$14.94 \pm 0.02$	$13.58 \pm 0.02$	24
VISE J061437.73+095135.0		T7	$17.54 \pm 0.05$	$16.44 \pm 0.02$	$16.66 \pm 0.05$	$16.51 \pm 0.05$	25, 26	$16.62 \pm 0.11$	$14.24 \pm 0.05$	19	$15.48 \pm 0.02$	$13.36 \pm 0.02$ $14.09 \pm 0.02$	17
WISEPA J062309.94-045624.6		T8	$18.04 \pm 0.06$	$17.10 \pm 0.02$	$17.34 \pm 0.07$	$17.27 \pm 0.09$	25, 26	$16.84 \pm 0.09$	$13.81 \pm 0.04$	19	$15.49 \pm 0.03$	$13.74 \pm 0.02$	10
JGPS J072227.51-054031.2		T9	$17.37 \pm 0.02$	$16.52 \pm 0.02$	$16.90 \pm 0.02$	$17.27 \pm 0.09$ $17.07 \pm 0.08$	7	$15.25 \pm 0.05$	$12.20 \pm 0.02$	19	$14.30 \pm 0.02$	$13.74 \pm 0.02$ $12.22 \pm 0.02$	24
2MASSI J0727182+171001		T7	$17.37 \pm 0.02$ $16.16 \pm 0.06$	$15.19 \pm 0.03$	$15.67 \pm 0.02$	$17.67 \pm 0.08$ $15.69 \pm 0.03$	2, 11	$15.29 \pm 0.03$ $15.19 \pm 0.04$	$12.20 \pm 0.02$ $12.96 \pm 0.03$	19	$14.46 \pm 0.02$	$13.02 \pm 0.02$	24
MASS J07290002-3954043		T8 pec	$16.60 \pm 0.09$	$15.66 \pm 0.08$	$16.05 \pm 0.10$	$16.50 \pm 0.03$	26	$15.19 \pm 0.04$ $15.29 \pm 0.03$	$12.90 \pm 0.03$ $12.97 \pm 0.02$	19	$14.40 \pm 0.02$ $14.47 \pm 0.01$	$13.02 \pm 0.02$ $12.95 \pm 0.01$	23
							5						23
MASS J09393548-2448279		T8	$16.47 \pm 0.09$	$15.61 \pm 0.09$	$15.96 \pm 0.09$	$16.83 \pm 0.09$		$14.91 \pm 0.03$	$11.64 \pm 0.02$	19 19	$13.77 \pm 0.02$	$11.62 \pm 0.02$	18
TLAS J102940.52+093514.6	D.O.	T8	$18.24 \pm 0.02$	$17.28 \pm 0.01$	$17.63 \pm 0.01$	$17.64 \pm 0.02$	14	$16.78 \pm 0.12$	$14.38 \pm 0.07$		$16.08 \pm 0.03$	$14.46 \pm 0.02$	
VISE J103907.73–160002.9	B?	T7.5	$18.19 \pm 0.03$	$16.89 \pm 0.02$	$17.19 \pm 0.04$	$17.09 \pm 0.07$	16, 26	$16.48 \pm 0.07$	$14.18 \pm 0.05$	19	$15.87 \pm 0.03$	$14.21 \pm 0.02$	24
VISE J105257.95–194250.2		T7.5	$17.72 \pm 0.05$	$16.83 \pm 0.02$	$17.08 \pm 0.05$	$17.00 \pm 0.05$	25, 26	$16.58 \pm 0.08$	$14.11 \pm 0.04$	19	$15.66 \pm 0.03$	$14.22 \pm 0.02$	18
MASS J11145133–2618235		T7.5	$16.36 \pm 0.05$	$15.52 \pm 0.05$	$15.82 \pm 0.05$	$16.54 \pm 0.05$	8	$15.25 \pm 0.04$	$12.27 \pm 0.02$	19	$14.19 \pm 0.02$	$12.35 \pm 0.02$	24
VISE J112438.12-042149.7		T7	$17.35 \pm 0.05$	$16.37 \pm 0.02$	$16.77 \pm 0.05$	$16.64 \pm 0.06$	25, 26	$16.45 \pm 0.08$	$14.05 \pm 0.05$	19	$15.37 \pm 0.02$	$14.10 \pm 0.02$	17
MASSI J1217110-031113		T7.5	$16.58 \pm 0.03$	$15.56 \pm 0.03$	$15.98 \pm 0.03$	$15.92 \pm 0.03$	1	$15.27 \pm 0.04$	$13.21 \pm 0.03$	19	$14.75 \pm 0.02$	$13.29 \pm 0.02$	24
VISE J125448.52-072828.4		T7	$18.41 \pm 0.06$	$17.30 \pm 0.01$	$17.63 \pm 0.03$	$17.40 \pm 0.07$	18, 26	$16.78 \pm 0.10$	$14.85 \pm 0.08$	19	$16.33 \pm 0.04$	$14.82 \pm 0.02$	18
VISE J125715.90+400854.2		T7	$18.14 \pm 0.06$	$16.89 \pm 0.02$	$17.14 \pm 0.06$	$17.18 \pm 0.06$	25, 26	$16.67 \pm 0.08$	$14.43 \pm 0.05$	19	$15.92 \pm 0.03$	$14.49 \pm 0.02$	17
Ross 458C	C	T8	$17.72 \pm 0.03$	$16.69 \pm 0.02$	$17.01 \pm 0.04$	$16.90 \pm 0.06$	12	$16.04 \pm 0.06$	$13.85 \pm 0.04$	19	$15.28 \pm 0.01$	$13.77 \pm 0.01$	23
WISEPA J132233.66-234017.1		T8	$17.74 \pm 0.12$	$16.75 \pm 0.11$	$16.65 \pm 0.14$	$17.02 \pm 0.40$	26	$16.73 \pm 0.09$	$13.96 \pm 0.04$	19	$15.67 \pm 0.03$	$13.89 \pm 0.02$	10
JLAS J141623.94+134836.3	C	(sd) T7.5	$18.16 \pm 0.03$	$17.26\pm0.02$	$17.58 \pm 0.03$	$18.43 \pm 0.09$	12, 26	$15.99 \pm 0.19$	$12.78 \pm 0.04$	19	$14.74 \pm 0.02$	$12.80 \pm 0.02$	24
WISEPC J145715.03+581510.2		T7	$17.81 \pm 0.06$	$16.79 \pm 0.02$	$17.14 \pm 0.06$	$17.21 \pm 0.06$	25, 26	$16.66 \pm 0.06$	$14.42 \pm 0.04$	19	$15.85 \pm 0.03$	$14.44 \pm 0.02$	24
GJ 570D	C	T7.5	$15.78 \pm 0.10$	$14.82\pm0.05$	$15.28 \pm 0.05$	$15.52 \pm 0.05$	8	$14.93 \pm 0.04$	$12.13 \pm 0.02$	19	$13.88 \pm 0.02$	$12.15 \pm 0.02$	24
PSO J224.3820+47.4057		T7	$18.01 \pm 0.06$	$17.11 \pm 0.02$	$17.43 \pm 0.06$	$17.08 \pm 0.06$	21, 25, 26	$16.62 \pm 0.06$	$14.65 \pm 0.04$	19	•••	•••	
DSS J150411.63+102718.4	B?	T7	$17.63 \pm 0.02$	$16.51 \pm 0.01$	$16.99 \pm 0.05$	$17.12 \pm 0.08$	12	$16.22 \pm 0.06$	$14.06 \pm 0.04$	19	$15.50 \pm 0.03$	$14.06 \pm 0.02$	24
MASSI J1553022+153236	В	T7	$16.37 \pm 0.06$	$15.34 \pm 0.03$	$15.76 \pm 0.03$	$15.94 \pm 0.03$	2	$15.29 \pm 0.04$	$13.03 \pm 0.03$	19	$14.51 \pm 0.02$	$13.13 \pm 0.02$	24
DSS J162838.77+230821.1		T7	$17.27 \pm 0.03$	$16.25 \pm 0.03$	$16.63 \pm 0.03$	$16.72 \pm 0.03$	3	$16.27 \pm 0.05$	$13.92 \pm 0.04$	19	$15.44 \pm 0.03$	$13.94 \pm 0.02$	24
VISEPA J165311.05+444423.9		T8	$18.11 \pm 0.06$	$17.08 \pm 0.02$	$17.60 \pm 0.05$	$17.07 \pm 0.06$	25, 26	$16.49 \pm 0.05$	$13.82 \pm 0.03$	19	$15.67 \pm 0.03$	$13.87 \pm 0.02$	10
VISEPA J171104.60+350036.8	В	T8	$18.55 \pm 0.14$	$17.63 \pm 0.13$	$18.06 \pm 0.14$	$18.10 \pm 0.14$	26	$17.80 \pm 0.16$	$14.63 \pm 0.04$	19	$16.46 \pm 0.04$	$14.62 \pm 0.02$	10
VISEPA J174124.26+255319.5		T9	$17.10 \pm 0.05$	$16.18 \pm 0.02$	$16.31 \pm 0.04$	$17.02 \pm 0.20$	15, 26	$15.30 \pm 0.04$	$12.35 \pm 0.02$	19	$14.43 \pm 0.02$	$12.39 \pm 0.02$	10
VISE J180901.07+383805.4		T7.5	$18.23 \pm 0.06$	$17.39 \pm 0.02$	$17.70 \pm 0.06$	$17.32 \pm 0.07$	25, 26	$17.59 \pm 0.13$	$14.98 \pm 0.06$	19	$16.49 \pm 0.04$	$14.90 \pm 0.02$	17
VISE J181329.40+283533.3		T8	$17.86 \pm 0.05$	$16.91 \pm 0.02$	$17.11 \pm 0.06$	$16.93 \pm 0.06$	25, 26	$15.58 \pm 0.04$	$14.04 \pm 0.04$	19	$15.82 \pm 0.03$	$14.19 \pm 0.02$	17
VISEPA J185215.78+353716.3		T7	$17.41 \pm 0.05$	$16.32\pm0.02$	$16.73 \pm 0.06$	$16.52 \pm 0.06$	25, 26	$15.95 \pm 0.05$	$14.14 \pm 0.04$	19	$15.58 \pm 0.03$	$14.19\pm0.02$	10
VISEPA J195905.66-333833.7		T8	$17.67 \pm 0.09$	$16.71 \pm 0.07$	$17.18\pm0.05$	$16.93 \pm 0.09$	10, 26	$16.15 \pm 0.06$	$13.84\pm0.04$	19	$15.36 \pm 0.02$	$13.79\pm0.02$	17
/ISE J200050.19+362950.1		T8	$16.31 \pm 0.05$	$15.44\pm0.01$	$15.85 \pm 0.01$	$16.13 \pm 0.04$	13, 20, 26	$15.08 \pm 0.06$	$12.69 \pm 0.03$	19	$14.22 \pm 0.02$	$12.68\pm0.02$	23
VISEPC J215751.38+265931.4		T7	$18.00\pm0.05$	$17.04\pm0.02$	$17.49\pm0.04$	$17.35\pm0.06$	25, 26	$16.99 \pm 0.11$	$14.49\pm0.05$	19	$16.01 \pm 0.03$	$14.44\pm0.02$	10
VISEPC J220922.10-273439.5		T7	$17.53\pm0.05$	$16.55\pm0.02$	$16.91\pm0.06$	$17.31\pm0.06$	25, 26	$16.31 \pm 0.08$	$13.86\pm0.04$	19	$15.48\pm0.03$	$13.90\pm0.02$	10
VISEPC J221354.69+091139.4		T7	$17.81\pm0.05$	$16.76\pm0.02$	$17.11\pm0.06$	$17.12\pm0.06$	25, 26	$16.58\pm0.08$	$14.65\pm0.06$	19	$15.79\pm0.03$	$14.56\pm0.02$	10
VISEPC J222623.05+044003.9		T8	$18.04 \pm 0.03$	$16.90\pm0.02$	$17.45\pm0.07$	$17.24 \pm 0.09$	12	$16.86 \pm 0.11$	$14.51\pm0.06$	19	$16.12 \pm 0.03$	$14.54\pm0.02$	10
VISEPC J225540.74-311841.8		T8	$18.38\pm0.02$	$17.33\pm0.01$	$17.66\pm0.03$	$17.42\pm0.05$	22, 26	$16.55\pm0.08$	$14.16\pm0.05$	19	$15.91 \pm 0.03$	$14.21\pm0.02$	10
VISEPC J231939.13-184404.3		T7.5	$18.56\pm0.06$	$17.56\pm0.02$	$17.95 \pm 0.05$	$18.27\pm0.08$	10, 26	$16.67 \pm 0.09$	$13.82 \pm 0.04$	19	$15.92 \pm 0.03$	$13.95 \pm 0.02$	10
JLAS J232123.79+135454.9		T7.5	$17.92 \pm 0.03$	$16.72 \pm 0.03$	$17.15 \pm 0.03$	$17.16 \pm 0.01$	6	$16.94 \pm 0.12$	$14.11 \pm 0.06$	19	$15.86 \pm 0.03$	$14.19 \pm 0.02$	24
	B?	T7	$17.20 \pm 0.06$	$16.08 \pm 0.03$	$16.41 \pm 0.04$	$16.51 \pm 0.06$	26	$15.93 \pm 0.06$	$13.60 \pm 0.04$	19	$15.19 \pm 0.02$	$13.62 \pm 0.02$	10

Table 3 (Continued)

				Near-inf	rared MKO Photo	metry		Al	WISE Photometry	ý	Spitze	er/IRAC Photome	try
Object	Type <sup>a</sup>	SpT	Y <sub>MKO</sub> (mag)	$J_{ m MKO}$ (mag)	H <sub>MKO</sub> (mag)	K <sub>MKO</sub> (mag)	References	W1 (mag)	W2 (mag)	References	[3.6] (mag)	[4.5] (mag)	References
WISEPC J234841.10-102844.4		T7	$17.69 \pm 0.05$	$16.62 \pm 0.02$	$16.99 \pm 0.06$	$16.84 \pm 0.06$	25, 26	$16.65 \pm 0.09$	$14.38 \pm 0.05$	19	$15.87 \pm 0.03$	$14.36 \pm 0.02$	10

#### Notes.

<sup>&</sup>lt;sup>a</sup> "B": resolved binaries; "B?": binarity likely but not confirmed (Section 4.2); "C": companions to stars or brown dwarfs. The remaining objects are single field dwarfs.

b We calculate synthetic photometry for WISE J024124.73–365328.0 ( $Y_{MKO}$  and  $X_{MKO}$ ) and UGPS J052127.27+364048.6 ( $Y_{MKO}$ ) using their SpeX prism spectra and the approach described in Best et al. (2021). **References.** (1) Leggett et al. (2002), (2) Knapp et al. (2004), (3) Chiu et al. (2006), (4) Luhman et al. (2007), (5) Leggett et al. (2009), (6) Burningham et al. (2010b), (7) Lucas et al. (2010), (8) Leggett et al. (2010), (9) Gelino et al. (2011), (10) Kirkpatrick et al. (2011), (11) Dupuy & Liu (2012), (12) Lawrence et al. (2012), (13) UKIDSS Consortium (2012), (14) Burningham et al. (2013), (15) Dupuy & Kraus (2013), (16) McMahon et al. (2013), (17) Mace et al. (2013a), (18) Thompson et al. (2013), (19) Cutri et al. (2014), (20) Cushing et al. (2014), (21) Best et al. (2015), (22) Edge et al. (2016), (23) Leggett et al. (2017), (24) Kirkpatrick et al. (2019), (25) Best et al. (2020b), (26) Best et al. (2021), and (27) this work.

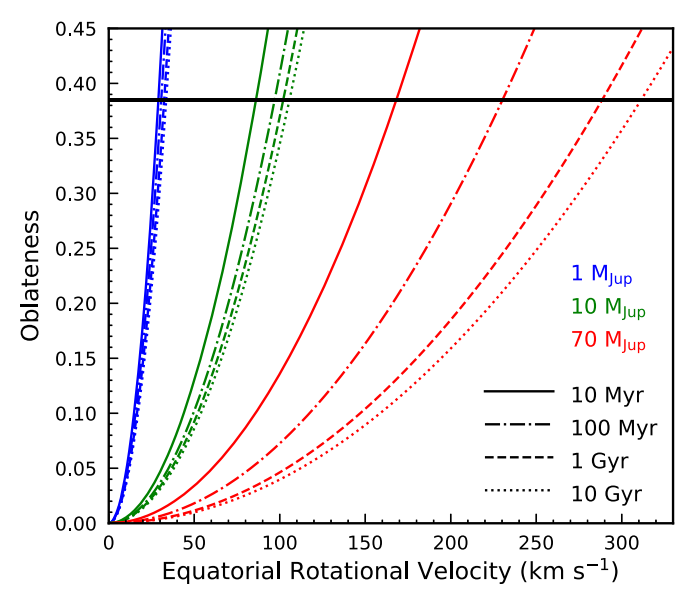


Figure 1. Rotation-induced oblateness as a function of equatorial rotational velocity  $v_{\rm rot}$  with different ages and masses, based on the solar-metallicity cloudless Sonora–Bobcat evolutionary models. We compute oblateness as  $f=2Cv_{\rm rot}^2/3gR$  (e.g., Barnes & Fortney 2003), where  $\{g,R\}$  are derived from the evolutionary models and C=0.9669 corresponds to the n=1.5 polytrope representative of fully convective brown dwarfs (e.g., Burrows & Liebert 1993). We use the black horizontal line to mark the critical oblateness ( $f_{\rm crit}=0.385$ ) below which objects are rotationally stable and have  $v_{\rm rot} \leq 300$  km s<sup>-1</sup>. These theoretical relations are only slightly changed using the Sonora–Bobcat models with nonsolar metallicities (i.e., Z=-0.5 and +0.5). A 10 Gyr old 70  $M_{\rm Jup}$  object can induce the same oblateness if it has a 0.5 dex lower metallicity but  $\approx 20$  km s<sup>-1</sup> higher  $v_{\rm rot}$ . Such an effect due to nonsolar metallicity diminishes with younger ages and lower masses.

among the J, H, and K bands. Therefore, the objects'  $\log\Omega$  posteriors, derived using spectra calibrated by  $J_{\rm MKO}$  or  $K_{\rm MKO}$ , will have different median values but similar uncertainties as compared to those inferred in this work using  $H_{\rm MKO}$ . As a reference, Table 4 lists the shifts ( $\Delta\log\Omega$ ) that our fitted  $\log\Omega$  values would be changed by if our objects' spectra were instead flux-calibrated using the J or K band. Our derived spectroscopic radii, masses, and bolometric luminosities (see Section 3.2) would be accordingly increased by  $0.5\Delta\log\Omega$ ,  $\Delta\log\Omega$ , and  $\Delta\log\Omega$  in the logarithmic scale, respectively. We do not incorporate these small shifts (which are mostly smaller than the uncertainties from the spectral fitting) into the systematic errors, so our spectroscopically inferred properties are all tied to the objects' H-band photometry.

#### 3.2. Results

Figure 2 presents the resulting parameter posteriors of our late-T dwarfs and compares the observed data with Sonora–Bobcat model spectra interpolated at the physical parameters drawn from the MCMC samples. These observed data and fitted model spectra of our entire sample are summarized in Figure 3. We list the fitted physical parameters and uncertainties in Table 4.8 We further use the objects' parallaxes and their fitted  $\log g$  and  $\log \Omega$  to derive their radii (R) and masses (M). We also

compute the bolometric luminosity  $(L_{bol})$  of each object by integrating its observed 1.0–2.5  $\mu$ m SpeX spectrum combined with the fitted model spectra at shorter and longer wavelengths spanning  $0.4-50 \mu m$ . We have incorporated uncertainties in the observed spectral fluxes, parallaxes, and fitted physical parameters into our resulting  $L_{bol}$  values in a Monte Carlo fashion. Such computed  $L_{bol}$  are not necessarily equal to those derived from the objects'  $T_{\rm eff}$  and R posteriors via the Stefan-Boltzmann law, given the mismatch between the observed spectra and fitted models in the 1.0–2.5  $\mu$ m wavelengths. We confirm our objects' bolometric luminosities computed from these two approaches are all consistent within the uncertainties. For HD 3651B, GJ 570D, and Ross 458C, we adopt the more accurate  $L_{\text{bol}}$  derived in our Paper I using their primary stars' ages and metallicities and the Sonora-Bobcat evolutionary models. We compare our computed  $L_{bol}$  with literature values in Appendix A and calculate bolometric corrections for T7–T9 dwarfs in Appendix B. The derived physical properties (R, M,and  $L_{\text{bol}}$ ) of our objects are summarized in Table 5.

We summarize the typical parameter uncertainties in Table 6 and find the resulting  $\{T_{\rm eff}, \log g, Z\}$  uncertainties of our sample are about a third to a half of the Sonora–Bobcat model grid spacing, the same as our finding in Paper I for the three late-T benchmarks, HD 3651B, GJ 570D, and Ross 458C. The fitted models generally match well the observed spectra, and we discuss the data–model comparison in Section 6.

Some of our spectroscopically inferred physical parameters of late-T dwarfs can be under- or overestimated relative to their true values, given that our set of models assume cloudless and chemical-equilibrium atmospheres. In Paper I, we analyzed three late-T benchmarks and compared the fitted parameters to those derived from their bolometric luminosities, their primary stars' metallicities and ages, and the Sonora-Bobcat evolutionary models. Assuming the evolutionary-based parameters were more robust, we found the accuracy of our forward-modeling results exhibited two outcomes. For HD 3651B and GJ 570D, our spectral fits produced reliable  $T_{\rm eff}$  and R, but underestimated  $\log g$ and Z by  $\approx 1.1-1.3$  dex and  $\approx 0.3-0.4$  dex, respectively. For Ross 458C, our spectral fit produced reliable logg and Z, but overestimated  $T_{\rm eff}$  by  $\approx$ 120 K and underestimated R by  $\approx$ 0.4  $R_{\rm Jup}$ (or a factor of  $\approx$ 1.6). Underestimation of the spectroscopically inferred logg and/or R further led to unphysically small masses of these objects. The late-T dwarfs in our sample might have their fitted parameters biased by amounts similar to those for the benchmarks, and in Sections 5 and 6, we demonstrate that the spectroscopically inferred parameters of this ensemble of late-T dwarfs are useful for assessing the model atmospheres.

We also conduct a forward-modeling analysis following the traditional approach, where we use linear interpolation to generate the model spectrum between grid points and adopt a diagonal covariance matrix (defined by observed flux uncertainties) to evaluate free parameters. We describe the details in Appendix C and present the results in Figure 20 and Table 9. Our Starfish analysis produces generally consistent physical parameters but with more realistic error estimates than those of the traditional approach. We therefore adopt the Starfish-based properties as the final results of our atmospheric model analysis and use them for subsequent discussions.

In the rest of this section, we study the impact of the data S/N and spectral resolution on our forward-modeling analysis (Section 3.2.1) and investigate the correlations among the inferred physical parameters (Section 3.2.2).

<sup>&</sup>lt;sup>8</sup> The spectroscopically inferred radial velocities and projected rotational velocities in our analysis cannot be well constrained due to the low spectral resolution of the data. These physical parameters ( $v_r$  and  $v\sin i$ ) are in fact coupled with the model systematics but have no correlations with, and therefore no impact on, the other physical parameters (Figure 5; also see Section 4.2 of Paper I).

 Table 4

 Starfish-based Forward-modeling Analysis: Fitted Parameters of T7–T9 Dwarfs

											Additiv System	ve $\log\Omega$ matics <sup>a</sup>
Object	Slit (")	$T_{\rm eff}$ (K)	logg (dex)	Z (dex)	$(\text{km s}^{v_r})$	$v\sin i \ (\text{km s}^{-1})$	$log\Omega$ (dex)	$a_N$	$\log a_G$ (dex)	$\ell$ (km s <sup>-1</sup> )	J band (dex)	K band (dex)
HD 3651B	0.5	818 <sup>+28</sup> (19)	$3.94^{+0.29}_{-0.28}^{+0.29}_{(0.20)}^{(0.20)}$	$-0.22^{+0.16\;(+0.11)}_{-0.16\;(-0.10)}$	$-318^{+202}_{-202}^{(95)}_{(96)}$	27 <sup>+27</sup> <sub>-27</sub> (20) (18)	$-19.543^{+0.072}_{-0.070} \stackrel{(0.051)}{_{(0.046)}}$	$1.06^{+0.04}_{-0.04}$	$-34.64^{+0.11}_{-0.11}$	$8114_{-1015}^{+751}$	+ 0.049	-0.029
WISE 0040+0900	0.5	883 <sup>+30</sup> (23) -30 (22)	$4.07^{+0.30}_{-0.29}  {}^{(0.22)}_{(0.22)}$	$-0.34^{+0.15}_{-0.15}  {}^{(+0.09)}_{(-0.09)}$	$-398^{+199}_{-199}{}^{(88)}_{(85)}$	33+31 (26)	$-19.676^{+0.072}_{-0.070}^{(0.052)}_{(0.047)}$	$1.03^{+0.04}_{-0.04}$	$-34.68^{+0.11}_{-0.10}$	$8153^{+725}_{-1020}$	+ 0.038	-0.015
WISE 0049+2151	0.5	$753^{+26}_{-26} {}^{(16)}_{(16)}$	$3.47^{+0.26}_{-0.22} \stackrel{(0.19)}{_{(0.14)}}$	$-0.24^{+0.18}_{-0.17}^{(+0.14)}_{(-0.12)}$	$-180^{+209}_{-209}^{(107)}_{(110)}$	$15^{+15}_{-15}_{(10)}^{(10)}$	$-19.348^{+0.069}_{-0.069} \stackrel{(0.045)}{_{(0.048)}}$	$1.04^{+0.04}_{-0.04}$	$-34.50^{+0.12}_{-0.11}$	$6848^{+1065}_{-907}$	-0.067	-0.016
	0.8	$756^{+27}_{-28}{}^{(19)}_{(19)}$	$3.58^{+0.28}_{-0.27}^{+0.28}_{(0.19)}^{(0.21)}$	$-0.23^{+0.18}_{-0.17}^{(+0.14)}_{(-0.12)}$	$-91^{+243}_{-245}^{(166)}_{(168)}$	$16^{+17}_{-16}{}^{(12)}_{(11)}$	$-19.390^{+0.073}_{-0.072}$	$1.05^{+0.04}_{-0.04}$	$-34.66^{+0.08}_{-0.07}$	$5454^{+90}_{-190}$	-0.035	-0.055
2MASS 0050-3322	0.5	$947^{+23}_{-24}{}^{(12)}_{(13)}$	$4.06^{+0.26}_{-0.26}_{(0.18)}^{(0.16)}$	$-0.11^{+0.15}_{-0.15} {}^{(+0.09)}_{(-0.08)}$	$-665^{+204}_{-204}^{(96)}_{(98)}$	$30^{+28}_{-30} {}^{(21)}_{(20)}$	$-19.593^{+0.069}_{-0.069}  {}^{(0.026)}_{(0.027)}$	$1.08^{+0.05}_{-0.05}$	$-34.54^{+0.07}_{-0.07}$	$1809^{+416}_{-288}$	-0.002	+ 0.007
WISE 0123+4142	0.8	$1023^{+26}_{-26}{}^{(17)}_{(17)}$	$4.13^{+0.32}_{-0.31}^{+0.32}_{(0.24)}^{(0.25)}$	$-0.31^{+0.15}_{-0.15} {}^{(+0.10)}_{(-0.09)}$	$-147^{+227}_{-226}^{(140)}_{(142)}$	$32^{+32}_{-32}{}^{(25)}_{(21)}$	$-20.290^{+0.064}_{-0.064}{}^{(0.032)}_{(0.032)}$	$0.83^{+0.04}_{-0.04}$	$-35.66^{+0.08}_{-0.08}$	$5246_{-410}^{+238}$	-0.004	+ 0.029
WISE 0223-2932	0.5	$787^{+31}_{-32} \stackrel{(23)}{_{(25)}}$	$4.15^{+0.30}_{-0.29} \stackrel{(0.21)}{_{(0.21)}}$	$-0.33^{+0.15}_{-0.15}  {}^{(+0.09)}_{(-0.09)}$	$-387^{+211}_{-211}^{(113)}_{(110)}$	$32^{+31}_{-32} \stackrel{(25)}{_{(21)}}$	$-19.739^{+0.096}_{-0.091} \stackrel{(0.069)}{_{(0.060)}}$	$1.04^{+0.04}_{-0.04}$	$-35.23^{+0.11}_{-0.10}$	$8371^{+598}_{-989}$	-0.063	+ 0.020
WISE 0241-3653	0.8	909 <sup>+25</sup> (15) -25 (14)	$3.93^{+0.26}_{-0.26} {}^{(0.17)}_{(0.18)}$	$-0.34^{+0.14}_{-0.14}  {}^{(+0.07)}_{(-0.07)}$	$-134^{+213}_{-212}^{(116)}_{(114)}$	$29^{+27}_{-29}{}^{(20)}_{(19)}$	$-19.927^{+0.064}_{-0.065} \stackrel{(0.029)}{_{(0.030)}}$	$0.66^{+0.04}_{-0.04}$	$-35.50^{+0.08}_{-0.08}$	$5439^{+100}_{-207}$	-0.009	-0.003
WISE 0245-3450	0.5	$804^{+25}_{-25}{}^{(15)}_{(15)}$	$3.43^{+0.25}_{-0.18} {}^{(0.16)}_{(0.11)}$	$-0.36^{+0.15}_{-0.14}  {}^{(+0.10)}_{(-0.08)}$	$-9^{+228}_{-227}^{(144)}_{(139)}$	$152^{+104}_{-106}$ (103)	$-20.084^{+0.074}_{-0.074}_{(0.038)}^{(0.036)}$	$1.00^{+0.04}_{-0.04}$	$-36.06^{+0.14}_{-0.13}$	$6579^{+1643}_{-1677}$	-0.017	+ 0.070
PSO J043+02	0.5	$798^{+28}_{-28}{}^{(19)}_{(20)}$	$4.15^{+0.30}_{-0.30}$ (0.22)	$-0.11^{+0.18}_{-0.17}  {}^{(+0.13)}_{(-0.12)}$	$-60^{+202}_{-203}^{(94)}_{(93)}$	$30^{+29}_{-30} {}^{(22)}_{(20)}$	$-19.380^{+0.074}_{-0.072}^{+0.074}_{(0.051)}^{+0.073}_{(0.051)}$	$1.02^{+0.04}_{-0.04}$	$-34.24^{+0.10}_{-0.10}$	$7984_{-912}^{+798}$	+ 0.017	-0.059
WISE 0325+0831	0.5	873 <sup>+28</sup> (19) -27 (19)	$3.42^{+0.25}_{-0.17} \stackrel{(0.18)}{_{(0.10)}}$	$-0.13^{+0.22}_{-0.20}{}^{(+0.20)}_{(-0.15)}$	$-248^{+202}_{-201}$ (93)	$17^{+17}_{-17}_{(11)}^{(11)}$	$-19.493^{+0.072\ (0.043)}_{-0.071\ (0.038)}$	$1.06^{+0.04}_{-0.04}$	$-34.35^{+0.11}_{-0.11}$	$8482^{+512}_{-819}$	-0.156	-0.122
2MASS 0415-0935	0.5	793 <sup>+28</sup> (19)	$4.07^{+0.28}_{-0.28}  {}^{(0.20)}_{(0.20)}$	$-0.13^{+0.18}_{-0.18}  ^{(+0.14)}_{(-0.13)}$	$-180^{+195}_{-195}^{(76)}_{(76)}$	$29^{+28}_{-29}^{(22)}_{(19)}$	$-19.135^{+0.074}_{-0.072}  \substack{(0.051) \\ (0.051)}$	$1.06^{+0.04}_{-0.04}$	$-33.75^{+0.09}_{-0.10}$	$8227^{+644}_{-797}$	+ 0.032	+ 0.001
WISE 0458+6434	0.5	$743^{+32}_{-33} \stackrel{(25)}{_{(27)}}$	$3.91^{+0.36}_{-0.34} \stackrel{(0.30)}{_{(0.27)}}$	$-0.32^{+0.19}_{-0.17}  {}^{(+0.15)}_{(-0.11)}$	$-1121^{+256}_{-257}^{(186)}_{(183)}$	$23^{+25}_{-23} \stackrel{(19)}{_{(15)}}$	$-19.651^{+0.101}_{-0.096}  \substack{(0.076) \\ (0.071)}$	$1.02^{+0.04}_{-0.04}$	$-34.93^{+0.11}_{-0.11}$	$8234_{-1008}^{+683}$	-0.019	+0.194
WISE 0500-1223	0.5	727 <sup>+46</sup> <sub>-53</sub> (49)	$4.13^{+0.43}_{-0.41} \stackrel{(0.36)}{_{(0.34)}}$	$-0.38^{+0.17}_{-0.12}  {}^{(+0.13)}_{(-0.08)}$	$-242^{+324}_{-326} \stackrel{(275)}{_{(267)}}$	28 <sup>+34</sup> <sub>-28</sub> (28)	$-19.910^{+0.182}_{-0.138} \stackrel{(0.168)}{(0.112)}$	$1.07^{+0.04}_{-0.04}$	$-35.50^{+0.14}_{-0.13}$	$8045^{+819}_{-1273}$	-0.018	+0.217
WISE 0521+1025	0.8	846 <sup>+25</sup> (15) -24 (14)	$3.36^{+0.22}_{-0.11} \stackrel{(0.11)}{(0.06)}$	$-0.29^{+0.16}_{-0.15}  {}^{(+0.10)}_{(-0.09)}$	$-184^{+220}_{-220}$ (128)	15 <sup>+16</sup> <sub>-15</sub> (10)	$-19.003^{+0.064}_{-0.064} \stackrel{(0.031)}{(0.034)}$	$0.90^{+0.04}_{-0.04}$	$-33.80^{+0.07}_{-0.07}$	$5482^{+70}_{-148}$	-0.005	+ 0.026
UGPS 0521+3640	0.8	$781^{+29}_{-29}{}^{(22)}_{(21)}$	$4.50^{+0.30}_{-0.30}_{(0.22)}^{(0.22)}$	$-0.23^{+0.18}_{-0.19} {\scriptstyle{(0.15)}\atop{(0.15)}}$	$-165^{+255}_{-257}^{(182)}_{(181)}$	$39^{+35}_{-39} \stackrel{(30)}{(26)}$	$-19.783^{+0.077}_{-0.075} \stackrel{(0.058)}{_{(0.051)}}$	$0.75^{+0.04}_{-0.04}$	$-35.11^{+0.07}_{-0.07}$	$5481^{+70}_{-145}$	+ 0.049	+ 0.073
WISE 0614+0951	0.8	956 <sup>+26</sup> (17)	$4.21^{+0.28}_{-0.29} \stackrel{(0.20)}{_{(0.20)}}$	$-0.01^{+0.17}_{-0.17}  {}^{(+0.13)}_{(-0.11)}$	$-743^{+217}_{-218}{}^{(123)}_{(124)}$	37 <sup>+34</sup> (29) -37 (25)	$-19.902^{+0.064}_{-0.065} \stackrel{(0.033)}{_{(0.034)}}$	$0.93^{+0.04}_{-0.04}$	$-35.06^{+0.07}_{-0.07}$	$5470^{+79}_{-169}$	-0.003	+0.029
WISE 0623-0456	0.5	$743^{+53}_{-51} \stackrel{(49)}{(47)}$	$4.70^{+0.47}_{-0.42} \stackrel{(0.44)}{_{(0.36)}}$	$-0.32^{+0.18}_{-0.16}  ^{(+0.15)}_{(-0.11)}$	$-167^{+303}_{-301}^{(243)}_{(245)}$	$60^{+70}_{-55} \stackrel{(69)}{_{(40)}}$	$-19.610^{+0.167}_{-0.156} \stackrel{(0.158)}{(0.145)}$	$1.06^{+0.04}_{-0.04}$	$-34.98^{+0.14}_{-0.14}$	$7939^{+895}_{-1365}$	-0.056	+0.116
UGPS 0722-0540	0.5	680 <sup>+26</sup> (16)	$3.60^{+0.30}_{-0.28} \stackrel{(0.24)}{_{(0.21)}}$	$-0.06^{+0.21}_{-0.20}  {}^{(+0.17)}_{(-0.16)}$	$-28^{+204}_{-204}^{(96)}_{(98)}$	$14^{+15}_{-14} {}^{(10)}_{(9)}$	$-19.225^{+0.075}_{-0.072} \stackrel{(0.056)}{_{(0.048)}}$	$0.99^{+0.04}_{-0.04}$	$-34.40^{+0.08}_{-0.08}$	$8744^{+329}_{-599}$	+ 0.031	-0.040
2MASS 0727+1710	0.5	896 <sup>+26</sup> (17)	$3.93^{+0.25}_{-0.25} \stackrel{\text{(0.15)}}{\text{(0.16)}}$	$-0.22^{+0.14}_{-0.14}  {}^{(+0.07)}_{(-0.07)}$	$-0^{+203}_{-203} \stackrel{(95)}{(96)}$	27 <sup>+26</sup> <sub>-27</sub> (20)	$-19.326^{+0.063}_{-0.063} \stackrel{(0.035)}{(0.037)}$	$1.07^{+0.05}_{-0.05}$	$-34.19^{+0.09}_{-0.08}$	$3206_{-366}^{+447}$	+ 0.027	-0.029
2MASS 0729-3954	0.5	806 <sup>+41</sup> <sub>-42</sub> (38)	$4.51^{+0.32}_{-0.34} \stackrel{(0.24)}{_{(0.28)}}$	$-0.40^{+0.14}_{-0.10}^{+0.09}_{(-0.06)}$	$-197^{+225}_{-222}^{(137)}_{(131)}$	50+48 (46) (34)	$-19.263^{+0.124}_{-0.113} \stackrel{(0.110)}{(0.093)}$	$1.04^{+0.04}_{-0.04}$	$-34.10^{+0.12}_{-0.11}$	$7538^{+1048}_{-1128}$	-0.004	+0.075
2MASS 0939-2448	0.5	$656^{+41}_{-34} \stackrel{(35)}{(28)}$	$4.74^{+0.33}_{-0.30} \stackrel{(0.27)}{_{(0.20)}}$	$-0.41^{+0.15}_{-0.09}  {}^{(+0.11)}_{(-0.06)}$	$-84^{+243}_{-238}$ (165)	$74^{+63}_{-61} \stackrel{(62)}{_{(50)}}$	$-18.749^{+0.129}_{-0.152} \stackrel{(0.109)}{(0.138)}$	$1.11^{+0.05}_{-0.04}$	$-33.97^{+0.09}_{-0.08}$	$3623^{+460}_{-381}$	-0.000	+ 0.010
ULAS 1029+0935	0.5	$794^{+26}_{-26}^{(17)}_{(17)}$	$3.61^{+0.30}_{-0.28} \stackrel{(0.23)}{_{(0.20)}}$	$-0.24^{+0.19}_{-0.18}  ^{(+0.15)}_{(-0.13)}$	$-287^{+214}_{-214}^{(118)}_{(119)}$	$19^{+19}_{-19} \stackrel{(13)}{_{(12)}}$	$-19.860^{+0.065}_{-0.066} \stackrel{(0.041)}{(0.043)}$	$1.00^{+0.04}_{-0.04}$	$-35.30^{+0.11}_{-0.10}$	$8620^{+424}_{-754}$	-0.004	-0.043
WISE 1039-1600	0.5	847 <sup>+29</sup> (21)	$3.74^{+0.31}_{-0.29} \stackrel{(0.24)}{(0.21)}$	$-0.38^{+0.15}_{-0.12}  {}^{(+0.10)}_{(-0.07)}$	$-359^{+235}_{-235}^{(153)}_{(151)}$	$27^{+26}_{-27}^{(21)}_{(17)}$	$-19.803^{+0.073}_{-0.072} \stackrel{(0.050)}{(0.049)}$	$1.04^{+0.04}_{-0.04}$	$-35.06^{+0.13}_{-0.13}$	$6024^{+1816}_{-1537}$	-0.059	+ 0.064
WISE 1052-1942	0.5	821+30 (23)	$3.83^{+0.30}_{-0.29} \stackrel{(0.23)}{_{(0.22)}}$	$-0.39^{+0.15}_{-0.11}  {}^{(+0.10)}_{(-0.07)}$	$-298^{+228}_{-226}^{(144)}_{(143)}$	$24^{+25}_{-24}{}^{(19)}_{(16)}$	$-19.772^{+0.080}_{-0.077} \stackrel{(0.060)}{(0.052)}$	$1.08^{+0.04}_{-0.04}$	$-34.92^{+0.10}_{-0.10}$	8433+549	-0.005	+ 0.033
2MASS 1114-2618	0.5	$729^{+60}_{-55}^{(59)}_{(49)}$	$4.52^{+0.42}_{-0.42} \stackrel{(0.35)}{_{(0.38)}}$	$-0.40^{+0.15}_{-0.10}  {}^{(+0.11)}_{(-0.07)}$	$-130^{+262}_{-262}$ (191)	49 <sup>+57</sup> <sub>-49</sub> (57) (33)	$-18.986^{+0.189}_{-0.182} \stackrel{(0.179)}{_{(0.178)}}$	$1.07^{+0.05}_{-0.05}$	$-33.80^{+0.07}_{-0.07}$	$2150^{+316}_{-264}$	-0.002	-0.001
WISE 1124-0421	0.5	879 <sup>+28</sup> (20) -29 (21)	$4.18^{+0.29}_{-0.28} \stackrel{(0.21)}{_{(0.20)}}$	$-0.38^{+0.14}_{-0.12}  {}^{(+0.08)}_{(-0.07)}$	$-566^{+198}_{-197}^{(83)}_{(82)}$	$40^{+35}_{-40} \stackrel{(30)}{(27)}$	$-19.736^{+0.073}_{-0.071} \stackrel{(0.050)}{(0.042)}$	$1.07^{+0.04}_{-0.04}$	$-34.92^{+0.11}_{-0.11}$	$8479^{+518}_{-906}$	-0.004	+ 0.040
2MASS 1217-0311	0.5	886 <sup>+24</sup> (14) -24 (13)	$3.98^{+0.26}_{-0.27} \stackrel{(0.17)}{_{(0.18)}}$	$-0.00^{+0.16}_{-0.16} \stackrel{(0.11)}{_{(0.11)}}$	$-164^{+220}_{-221}^{(127)}_{(127)}$	$30^{+28}_{-30} \stackrel{(22)}{(20)}$	$-19.437^{+0.059}_{-0.059} \stackrel{(0.029)}{(0.028)}$	$1.02^{+0.05}_{-0.05}$	$-34.22^{+0.07}_{-0.06}$	$1698^{+209}_{-181}$	+ 0.017	-0.025
WISE 1254-0728	0.5	$936^{+32}_{-32} \stackrel{(24)}{_{(25)}}$	$3.98^{+0.32}_{-0.32} \stackrel{(0.24)}{_{(0.25)}}$	$-0.15^{+0.20}_{-0.18}^{+0.16}_{(-0.13)}$	$-2^{+258}_{-259} \stackrel{(184)}{_{(187)}}$	28 <sup>+29</sup> <sub>-28</sub> (22) (19)	$-20.220^{+0.072}_{-0.071} \stackrel{(0.028)}{(0.048)}$	$1.09^{+0.04}_{-0.04}$	$-35.62^{+0.14}_{-0.14}$	$6486^{+1626}_{-1624}$	-0.012	+ 0.098
WISE 1257+4008	0.5	933+34 (27)	$4.83^{+0.41}_{-0.40} \stackrel{(0.37)}{_{(0.35)}}$	$-0.06^{+0.19}_{-0.18}  ^{(+0.14)}_{(-0.14)}$	$-397^{+223}_{-224}^{(135)}_{(135)}$	67 <sup>+65</sup> <sub>-58</sub> (63) (45)	$-20.067^{+0.083}_{-0.080} \stackrel{(0.062)}{_{(0.055)}}$	$1.05^{+0.04}_{-0.04}$	$-35.05^{+0.11}_{-0.11}$	8328 <sup>+618</sup> <sub>-1014</sub>	-0.004	+ 0.067
Ross 458C	0.5	804 <sup>+30</sup> <sub>-29</sub> (21)	$4.09^{+0.31}_{-0.33} \stackrel{(0.23)}{_{(0.28)}}$	$-0.13^{+0.20}_{-0.23}^{+0.20}_{(0.20)}^{(0.17)}$	$-276^{+217}_{-217}^{(125)}_{(119)}$	28 <sup>+30</sup> <sub>-28</sub> (23) (19)	$-19.727^{+0.075}_{-0.076} \stackrel{(0.054)}{(0.057)}$	$0.93^{+0.04}_{-0.04}$	$-34.67^{+0.09}_{-0.09}$	8541 <sup>+471</sup> <sub>-747</sub>	+ 0.068	-0.135
WISE 1322-2340	0.5	822+34 (28)	$3.98^{+0.34}_{-0.32} \stackrel{(0.28)}{_{(0.25)}}$	$-0.38^{+0.15}_{-0.12}  ^{(0.20)}_{(-0.08)}$	$-132^{+281}_{-284} \stackrel{(213)}{(225)}$	$30^{+31}_{-30} \stackrel{(25)}{(20)}$	$-19.558^{+0.109}_{-0.101} \stackrel{(0.083)}{(0.063)}$	$1.08^{+0.05}_{-0.05}$	$-33.91^{+0.04}_{-0.04}$	$825^{+8}_{-4}$	-0.198	+ 0.068
ULAS 1416+1348	0.5	695 <sup>+33</sup> (27) 695 <sup>-32</sup> (25)	$5.21^{+0.26}_{-0.25} \stackrel{(0.19)}{_{(0.15)}}$	$-0.39^{+0.14}_{-0.11}  ^{(+0.09)}_{(-0.07)}$	$-348^{+218}_{-218}$ (123)	$108^{+74}_{-78} {}^{(74)}_{(74)}$	$-19.555^{+0.105}_{-0.107} \stackrel{(0.093)}{(0.097)}$	$1.09^{+0.04}_{-0.04}$	$-35.36^{+0.11}_{-0.10}$	$8504^{+509}_{-910}$	+ 0.030	+ 0.274
WISE 1457+5815	0.5	882 <sup>+30</sup> (23) 882 <sup>-31</sup> (24)	$4.27^{+0.33}_{-0.31} \stackrel{(0.26)}{_{(0.24)}}$	$-0.31^{+0.15}_{-0.15} \stackrel{(+0.09)}{(-0.09)}$	$-308^{+209}_{-209}^{(109)}_{(106)}$	$44^{+40}_{-44} \stackrel{(36)}{(29)}$	$-19.918^{+0.078}_{-0.075} \stackrel{(0.057)}{(0.049)}$	$0.97^{+0.04}_{-0.04}$	$-35.30^{+0.13}_{-0.12}$	$8274^{+659}_{-1029}$	-0.005	
GJ 570D	0.5	828 <sup>+25</sup> <sub>-26</sub> (16)	$3.90^{+0.25}_{-0.25} \stackrel{(0.16)}{_{(0.15)}}$	$-0.33^{+0.14}_{-0.14} \stackrel{(+0.08)}{_{(-0.08)}}$	$-431^{+213}_{-212} \stackrel{(114)}{(115)}$	$26^{+25}_{-26}$ (18)	$-19.012^{+0.067}_{-0.066} \stackrel{(0.049)}{(0.037)}$	$1.04^{+0.05}_{-0.05}$	$-33.79^{+0.08}_{-0.08}$	$2714_{-372}^{+437}$	+ 0.010	+ 0.086 + 0.014
PSO J224+47	0.8	$930^{+27}_{-27}$ (18)	$3.62^{+0.30}_{-0.29} \stackrel{(0.23)}{_{(0.22)}}$	$-0.12^{+0.20}_{-0.19} {}^{(0.16)}_{(0.15)}$	$-426^{+242}_{-241}$ (164)	$19^{+19}_{-19} \stackrel{(14)}{(12)}$	$-20.102^{+0.066}_{-0.066} \stackrel{(0.037)}{(0.035)}$	$1.08^{+0.04}_{-0.04}$	$-35.52^{+0.10}_{-0.09}$	5337 <sup>+175</sup> <sub>-354</sub>	+ 0.019	+ 0.084

Table 4 (Continued)

											Additive System	•
Object	Slit (")	$T_{\rm eff}$ (K)	logg (dex)	Z (dex)	$(\operatorname{km s}^{v_{\rm r}})$	$v\sin i$ $(\text{km s}^{-1})$	$\frac{log\Omega}{(dex)}$	$a_N$	$\log a_G$ (dex)	$\ell$ (km s <sup>-1</sup> )	J band (dex)	K band (dex)
SDSS 1504+1027	0.8	937 <sup>+26</sup> (17)	$3.82^{+0.29}_{-0.28}$ (0.21)	$-0.39^{+0.15}_{-0.11}  {}^{(+0.09)}_{(-0.07)}$	$-817^{+225}_{-226}^{(136)}_{(139)}$	27 <sup>+25</sup> (20)	$-19.972^{+0.063}_{-0.063} \stackrel{(0.032)}{_{(0.033)}}$	$0.91^{+0.04}_{-0.04}$	$-35.28^{+0.09}_{-0.08}$	$5208^{+264}_{-422}$	+ 0.070	-0.041
2MASS 1553+1532	0.5	$885^{+27}_{-27}{}^{(18)}_{(18)}$	$4.10^{+0.25}_{-0.25} \stackrel{(0.15)}{_{(0.15)}}$	$-0.30^{+0.14}_{-0.14}^{(+0.07)}_{(-0.07)}$	$-183^{+188}_{-189}{}^{(59)}_{(59)}$	$40^{+34}_{-40}  {}^{(28)}_{(27)}$	$-19.350^{+0.066}_{-0.066} {}^{(0.042)}_{(0.039)}$	$1.01^{+0.04}_{-0.04}$	$-34.25^{+0.10}_{-0.10}$	$8263_{-883}^{+650}$	+ 0.014	-0.039
SDSS 1628+2308	0.8	$910^{+26}_{-26}{}^{(17)}_{(17)}$	$4.21^{+0.28}_{-0.28} \stackrel{(0.19)}{_{(0.19)}}$	$-0.05^{+0.18}_{-0.17}^{+0.18}_{(0.12)}^{+0.14}$	$-298^{+227}_{-229}^{(136)}_{(145)}$	$36^{+32}_{-36} {}^{(26)}_{(24)}$	$-19.781^{+0.062}_{-0.062} {}^{(0.036)}_{(0.036)}$	$1.03^{+0.04}_{-0.04}$	$-34.97\substack{+0.08 \\ -0.08}$	$5413^{+118}_{-236}$	+ 0.030	-0.068
WISE 1653+4444	0.5	$800^{+30}_{-30}_{(22)}^{(22)}$	$4.10^{+0.34}_{-0.36}$ (0.28)	$-0.01^{+0.22}_{-0.21}^{(+0.19)}_{(-0.18)}$	$-343^{+229}_{-230}^{(141)}_{(145)}$	$27^{+29}_{-27}{}^{(23)}_{(18)}$	$-19.950^{+0.078}_{-0.078} {}^{(0.054)}_{(0.057)}$	$1.07^{+0.04}_{-0.04}$	$-35.22\substack{+0.10 \\ -0.10}$	$8530^{+486}_{-811}$	+ 0.130	+ 0.206
WISE 1711+3500	0.5	$817^{+46}_{-52}{}^{(41)}_{(46)}$	$3.80^{+0.47}_{-0.38}  {}^{(0.43)}_{(0.33)}$	$-0.26^{+0.27}_{-0.20}{}^{(+0.25)}_{(-0.15)}$	$-499^{+448}_{-435}  {}^{(403)}_{(386)}$	$27^{+30}_{-27}{}^{(26)}_{(16)}$	$-20.122^{+0.141\ (0.114)}_{-0.122\ (0.092)}$	$1.18^{+0.05}_{-0.05}$	$-34.58\substack{+0.05 \\ -0.05}$	$824_{-3}^{+7}$	+ 0.047	+0.161
	0.8	$821^{+26}_{-26}{}^{(16)}_{(17)}$	$3.61^{+0.27}_{-0.26} {}^{(0.19)}_{(0.18)}$	$-0.42^{+0.14}_{-0.08}  {}^{(+0.08)}_{(-0.05)}$	$-546^{+231}_{-232}^{(146)}_{(147)}$	$21^{+21}_{-21}_{(14)}^{(15)}$	$-20.083^{+0.085}_{-0.084}^{+0.085}_{(0.038)}^{+0.085}$	$0.98^{+0.04}_{-0.04}$	$-35.94^{+0.10}_{-0.09}$	$5306^{+198}_{-368}$	-0.008	+ 0.102
WISE 1741+2553	0.8	$719^{+26}_{-26}{}^{(16)}_{(17)}$	$3.91^{+0.27}_{-0.28}  {}^{(0.19)}_{(0.20)}$	$-0.04^{+0.18\;(+0.13)}_{-0.17\;(-0.12)}$	$-118^{+219}_{-219}_{(127)}^{(127)}$	$21^{+22}_{-21}{}^{(16)}_{(14)}$	$-19.150^{+0.073\ (0.054)}_{-0.071\ (0.045)}$	$0.88^{+0.04}_{-0.04}$	$-34.41^{+0.05}_{-0.05}$	$5526_{-76}^{+36}$	-0.072	-0.210
WISE 1809+3838	0.8	$838^{+31}_{-31} \stackrel{(24)}{_{(24)}}$	$3.63^{+0.31}_{-0.29} \stackrel{(0.24)}{_{(0.21)}}$	$-0.31^{+0.19}_{-0.17}{}^{(+0.15)}_{(-0.12)}$	$-261^{+292}_{-296}{}^{(232)}_{(234)}$	$21^{+20}_{-21}$ (14)	$-19.997^{+0.078~(0.055)}_{-0.077~(0.053)}$	$1.14_{-0.04}^{+0.04}$	$-35.33^{+0.10}_{-0.10}$	$5272^{+224}_{-456}$	-0.019	+ 0.082
WISE 1813+2835	0.5	$811^{+30}_{-30} {}^{(22)}_{(22)}$	$4.20^{+0.33}_{-0.34}  {}^{(0.27)}_{(0.28)}$	$-0.05^{+0.22}_{-0.22}^{+0.19}_{(0.18)}$	$-107^{+214}_{-214}^{(117)}_{(115)}$	$35^{+34}_{-35} \stackrel{(30)}{(23)}$	$-19.761^{+0.079}_{-0.079} \stackrel{(0.054)}{_{(0.055)}}$	$0.92^{+0.04}_{-0.04}$	$-34.73^{+0.09}_{-0.09}$	$8526^{+480}_{-737}$	-0.004	+ 0.058
WISE 1852+3537	0.5	$899^{+27}_{-27}{}^{(18)}_{(18)}$	$3.97^{+0.27}_{-0.27} {\scriptstyle{(0.18)}\atop{(0.19)}}$	$-0.21^{+0.15}_{-0.15}  {}^{(+0.09)}_{(-0.09)}$	$-175^{+210~(108)}_{-210~(110)}$	$29^{+28}_{-29}{}^{(21)}_{(20)}$	$-19.761^{+0.068}_{-0.067} {}^{(0.037)}_{(0.039)}$	$1.06^{+0.04}_{-0.04}$	$-34.94^{+0.14}_{-0.12}$	$6118^{+1211}_{-957}$	-0.005	+ 0.028
WISE 1959-3338	0.5	$812^{+28}_{-28}{}^{(19)}_{(19)}$	$3.92^{+0.29}_{-0.29} {\scriptstyle{(0.21)}\atop{(0.21)}}$	$-0.10^{+0.20}_{-0.18}  {}^{(+0.16)}_{(-0.13)}$	$-47^{+207}_{-207}^{(102)}_{(105)}$	$24^{+25}_{-24}{}^{(18)}_{(16)}$	$-19.746^{+0.073}_{-0.072} \stackrel{(0.049)}{_{(0.048)}}$	$0.98^{+0.04}_{-0.04}$	$-35.04^{+0.11}_{-0.11}$	$8097^{+748}_{-994}$	+ 0.048	+ 0.095
WISE 2000+3629	0.5	$810^{+27}_{-27}{}^{(19)}_{(19)}$	$3.67^{+0.27}_{-0.27} {\scriptstyle{(0.19)}\atop{(0.18)}}$	$-0.36^{+0.16}_{-0.14}{}^{(+0.11)}_{(-0.09)}$	$-367^{+200~(88)}_{-200~(89)}$	$21^{+21}_{-21}_{(13)}^{(15)}$	$-19.207^{+0.068\;(0.046)}_{-0.068\;(0.046)}$	$0.95^{+0.04}_{-0.04}$	$-33.93^{+0.10}_{-0.10}$	$8254_{-846}^{+634}$	+ 0.035	-0.113
WISE 2157+2659	0.8	$860^{+26}_{-26}{}^{(16)}_{(16)}$	$3.79^{+0.27}_{-0.27}^{+0.18}_{(0.19)}$	$-0.28^{+0.15}_{-0.15}  {}^{(+0.09)}_{(-0.09)}$	$-176^{+219}_{-220}^{(123)}_{(130)}$	$22^{+21}_{-22}^{(15)}_{(14)}$	$-19.994^{+0.063}_{-0.063} \stackrel{(0.034)}{_{(0.037)}}$	$0.93^{+0.04}_{-0.04}$	$-35.65^{+0.07}_{-0.07}$	$5468^{+80}_{-170}$	+ 0.047	+ 0.100
WISE 2209-2734	0.8	$801^{+49}_{-46}{}^{(46)}_{(42)}$	$4.54^{+0.32}_{-0.36}^{+0.32}_{(0.32)}$	$-0.43^{+0.14}_{-0.07}^{(+0.08)}_{(-0.04)}$	$-142^{+235}_{-234}^{(155)}_{(145)}$	$56^{+54}_{-52} {}^{(54)}_{(38)}$	$-19.630^{+0.134}_{-0.129} \stackrel{(0.121)}{_{(0.123)}}$	$0.91^{+0.04}_{-0.04}$	$-35.07^{+0.08}_{-0.07}$	$5351^{+165}_{-292}$	-0.002	+ 0.054
WISE 2213+0911	0.5	$908^{+29}_{-30} {}^{(21)}_{(22)}$	$4.19^{+0.28}_{-0.28}  {}^{(0.20)}_{(0.19)}$	$-0.31^{+0.14}_{-0.14}  {}^{(+0.07)}_{(-0.08)}$	$-89^{+195}_{-195}^{(79)}_{(78)}$	$38^{+34}_{-38} \stackrel{(28)}{_{(25)}}$	$-19.957^{+0.073}_{-0.073} {\scriptstyle{(0.047)}\atop{(0.047)}}$	$1.01^{+0.04}_{-0.04}$	$-35.36\substack{+0.11 \\ -0.11}$	$8195^{+706}_{-1059}$	-0.002	+ 0.035
WISE 2226+0440	0.5	$829^{+26}_{-26}$ (18)	$3.78^{+0.28}_{-0.28} \stackrel{(0.19)}{_{(0.21)}}$	$-0.26^{+0.16}_{-0.16}{}^{(+0.11)}_{(-0.11)}$	$-120^{+206}_{-206}^{(101)}_{(103)}$	$25^{+24}_{-25}$ (18)	$-19.879^{+0.071}_{-0.070}$	$1.05^{+0.04}_{-0.04}$	$-35.30\substack{+0.11 \\ -0.10}$	$8024_{-1008}^{+788}$	+ 0.052	+ 0.085
WISE 2255-3118	0.5	$790^{+28}_{-27}{}^{(19)}_{(18)}$	$3.66^{+0.32}_{-0.30} \stackrel{(0.25)}{_{(0.23)}}$	$-0.21^{+0.20}_{-0.19}^{(+0.16)}_{(-0.14)}$	$-921^{+224}_{-224}{}^{(138)}_{(133)}$	$19^{+20}_{-19}_{(12)}^{(14)}$	$-19.868^{+0.071}_{-0.070}$	$1.07^{+0.04}_{-0.04}$	$-35.26^{+0.12}_{-0.11}$	$7523^{+1072}_{-1177}$	-0.013	+ 0.056
WISE 2319-1844	0.5	$782^{+39}_{-41} \stackrel{(33)}{_{(36)}}$	$4.46^{+0.34}_{-0.33} \stackrel{(0.27)}{_{(0.27)}}$	$-0.37^{+0.15}_{-0.13}^{(+0.11)}_{(-0.08)}$	$-533^{+237}_{-238}{}^{(155)}_{(161)}$	$39^{+39}_{-39} \stackrel{(35)}{_{(26)}}$	$-19.969^{+0.117}_{-0.106}  {}^{(0.108)}_{(0.090)}$	$1.01^{+0.04}_{-0.04}$	$-35.68^{+0.13}_{-0.13}$	$8258^{+667}_{-1066}$	-0.005	+ 0.189
ULAS 2321+1354	0.8	$822^{+29}_{-28}  {}^{(21)}_{(20)}$	$4.20^{+0.30\;(0.22)}_{-0.31\;(0.23)}$	$-0.18^{+0.20~(0.17)}_{-0.20~(0.16)}$	$-485^{+244~(167)}_{-244~(164)}$	$33^{+32}_{-33} \stackrel{(26)}{_{(22)}}$	$-19.770^{+0.071}_{-0.071} {\scriptstyle{(0.051)}\atop{(0.049)}}$	$0.88^{+0.04}_{-0.04}$	$-34.95^{+0.09}_{-0.09}$	$5041^{+367}_{-488}$	+ 0.033	-0.067
WISE 2340-0745	0.5	$918^{+31}_{-32} \stackrel{(23)}{_{(24)}}$	$4.53^{+0.30}_{-0.29} \stackrel{(0.22)}{_{(0.21)}}$	$-0.29^{+0.14}_{-0.14}^{(+0.08)}_{(-0.08)}$	$-199^{+194}_{-194}_{(74)}^{(75)}$	66 <sup>+54</sup> <sub>-57</sub> (51)	$-19.711^{+0.075}_{-0.072} \stackrel{(0.055)}{_{(0.049)}}$	$1.06^{+0.04}_{-0.04}$	$-34.73^{+0.10}_{-0.10}$	$8431^{+548}_{-881}$	-0.003	+ 0.031
WISE 2348-1028	0.5	900 <sup>+28</sup> (19) -28 (20)	$4.09^{+0.30\;(0.23)}_{-0.30\;(0.22)}$	$-0.15^{+0.18}_{-0.17}  {}^{(+0.13)}_{(-0.11)}$	$-127^{+205}_{-205}{}^{(100)}_{(101)}$	$31^{+30}_{-31}{}^{(24)}_{(21)}$	$-19.877^{+0.070\ (0.042)}_{-0.070\ (0.043)}$	$1.02^{+0.04}_{-0.04}$	$-34.99\substack{+0.12 \\ -0.11}$	$7297^{+1181}_{-1226}$	-0.004	+ 0.045

Notes. We report the median and  $1\sigma$  uncertainties for each fitted parameter with systematic errors incorporated (Section 3.1). The formal  $1\sigma$  errors of parameters directly obtained from the spectral-fitting process are shown in parentheses.

<sup>&</sup>lt;sup>a</sup> The small shifts to be added to our fitted  $\log\Omega$  if the objects' observed spectra are flux-calibrated by their  $J_{MKO}$  or  $K_{MKO}$  photometry rather than by  $H_{MKO}$  used in this work (see Section 3.1).

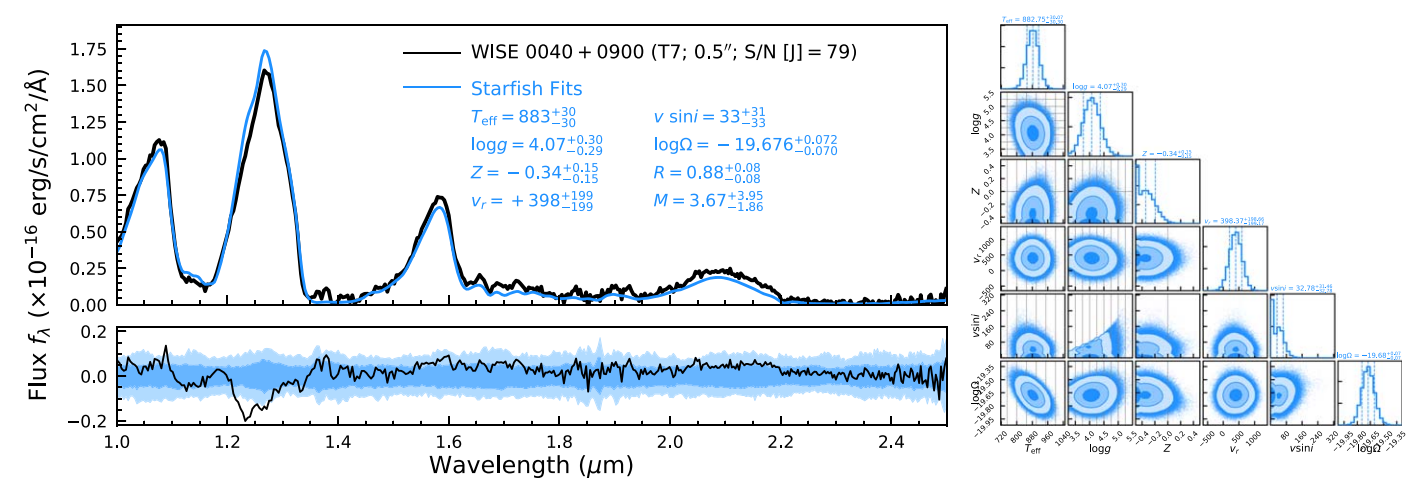


Figure 2. Starfish-based forward-modeling results of our late-T dwarf sample. Left: The upper panel shows the observed spectrum (black) of each object and the median Sonora–Bobcat model spectra of those interpolated at parameters drawn from the MCMC chains (blue). The object's name, its spectral type, the slit width and *J*-band S/N (median S/N in 1.2–1.3 μm) of its spectrum, and the inferred physical parameters are in the upper right corner. The lower panel shows the residual (data –model; black), with the blue shadows being the  $1\sigma$  and  $2\sigma$  dispersions of  $5 \times 10^4$  draws from Starfish's full covariance matrix. Right: Posteriors of the six physical parameters  $\{T_{\rm eff}, \log g, Z, v_r, v \sin i, \log \Omega\}$  derived from the Starfish-based forward-modeling analysis. We use gray vertical and horizontal lines to mark the  $\{T_{\rm eff}, \log g, Z\}$  grid points of the cloudless Sonora–Bobcat models. Figures of the spectral-fitting results for our entire sample (55 late-T dwarfs with 57 spectra) are accessible online.

(The complete figure set (57 images) is available.)

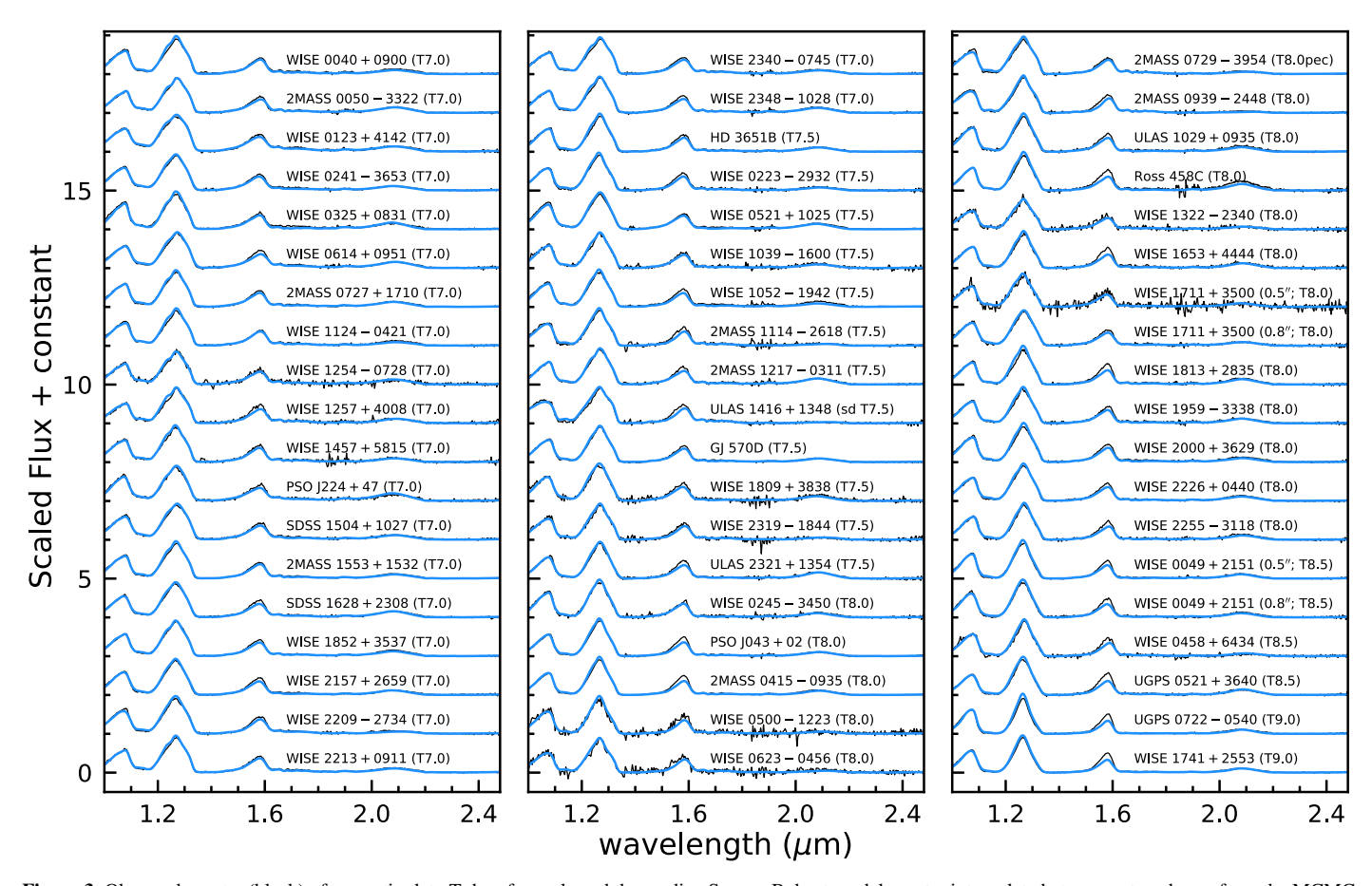


Figure 3. Observed spectra (black) of our entire late-T dwarf sample and the median Sonora-Bobcat model spectra interpolated at parameters drawn from the MCMC chains (blue).

Table 5
Starfish-based Forward-modeling Analysis: Derived Properties of T7–T9 Dwarfs

								$q_{(\lambda\lambda)}$ (	uantities	
Object	Slit (")	$R \atop (R_{\rm Jup})$	$M \over (M_{ m Jup})$	$\log(L_{ m bol}/L_{\odot}) \ ({ m dex})$	Age (Myr)	$\epsilon_J$ (%)	$q_Y$ (%)	$q_J$ $(\%)$	$q_H$ (%)	<i>q<sub>K</sub></i> (%)
HD 3651B	0.5	$0.81^{+0.07}_{-0.06}$	$2.33^{+2.27}_{-1.14}$	$-5.569^{+0.026}_{-0.029}$	$38^{+76}_{-25}$	$2.6^{+0.4}_{-0.3}$	$3\pm4$	$-9 \pm 4$	$17\pm 8$	$11\pm24$
WISE 0040+0900	0.5	$0.88^{+0.08}_{-0.08}$	$3.67^{+3.95}_{-1.86}$	$-5.347^{+0.045}_{-0.043}$	$50^{+195}_{-34}$	$2.6^{+0.3}_{-0.3}$	$6 \pm 4$	$-8 \pm 3$	$11 \pm 8$	$27 \pm 18$
WISE 0049+2151	0.5	$0.65^{+0.06}_{-0.05}$	$0.51^{+0.42}_{-0.19}$	$-5.895^{+0.039}_{-0.039}$	$8_{-4}^{+13}$	$2.8^{+0.4}_{-0.3}$	$3 \pm 4$	$-7 \pm 4$	$23 \pm 9$	$15 \pm 26$
	0.8	$0.62^{+0.06}_{-0.05}$	$0.59^{+0.57}_{-0.27}$	$-5.918^{+0.041}_{-0.039}$	$12^{+23}_{-7}$	$2.6^{+0.3}_{-0.2}$	$6 \pm 4$	$-8 \pm 3$	$27 \pm 7$	$24 \pm 19$
2MASS 0050-3322	0.5	$0.73^{+0.06}_{-0.06}$	$2.45^{+2.04}_{-1.13}$	$-5.397^{+0.039}_{-0.038}$	$40^{+105}_{-25}$	$1.9^{+0.2}_{-0.1}$	$-1 \pm 2$	$-2\pm1$	$10 \pm 3$	$6 \pm 7$
WISE 0123+4142	0.8	$0.79^{+0.08}_{-0.07}$	$3.32^{+3.67}_{-1.72}$	$-5.191^{+0.060}_{-0.058}$	$41^{+168}_{-28}$	$2.3^{+0.2}_{-0.2}$	$3\pm3$	$-4\pm2$	$11 \pm 4$	$9 \pm 12$
WISE 0223-2932	0.5	$0.72^{+0.09}_{-0.07}$	$2.95^{+3.43}_{-1.55}$	$-5.718^{+0.054}_{-0.051}$	$91^{+318}_{-63}$	$2.5^{+0.3}_{-0.3}$	$1 \pm 4$	$-7 \pm 3$	$21 \pm 8$	$19 \pm 28$
WISE 0241-3653	0.8	$0.90^{+0.09}_{-0.08}$	$2.75_{-1.29}^{+2.44}$	$-5.287^{+0.057}_{-0.054}$	$26^{+47}_{-17}$	$2.1^{+0.2}_{-0.2}$	$4\pm2$	$-5 \pm 2$	$13 \pm 4$	$3\pm13$
WISE 0245–3450 <sup>a</sup>	0.5				$6^{+8}_{-3}$	$2.0_{-0.3}^{+0.4}$	$6 \pm 3$	$-4 \pm 3$	$10 \pm 7$	$16 \pm 17$
PSO J043+02	0.5	$0.60^{+0.05}_{-0.05}$	$2.09^{+2.06}_{-1.04}$	$-5.856^{+0.034}_{-0.034}$	$92^{+311}_{-62}$	$3.1^{+0.4}_{-0.4}$	$-1 \pm 5$	$-6 \pm 4$	$26 \pm 9$	$1 \pm 31$
WISE 0325+0831	0.5	$0.99^{+0.09}_{-0.09}$	$1.04^{+0.81}_{-0.33}$	$-5.265^{+0.047}_{-0.046}$	$5^{+7}_{-2}$	$2.8^{+0.4}_{-0.3}$	$8 \pm 4$	$-6 \pm 4$	$16 \pm 9$	$2 \pm 19$
2MASS 0415-0935	0.5	$0.67^{+0.06}_{-0.05}$	$2.10^{+1.96}_{-1.02}$	$-5.779^{+0.036}_{-0.033}$	$68^{+202}_{-45}$	$3.2^{+0.4}_{-0.3}$	$-3 \pm 6$	$-7 \pm 4$	$27 \pm 9$	$17 \pm 27$
WISE 0458+6434	0.5	$0.59^{+0.08}_{-0.06}$	$1.16^{+1.64}_{-0.65}$	$-6.002^{+0.058}_{-0.054}$	$44^{+137}_{-32}$	$3.7^{+0.5}_{-0.5}$	$7 \pm 6$	$-10 \pm 5$	$25 \pm 12$	$-32 \pm 68$
WISE 0500-1223	0.5	$0.57^{+0.13}_{-0.08}$	$1.76^{+4.65}_{-1.19}$	$-6.070^{+0.058}_{-0.052}$	$106^{+549}_{-85}$	$3.8^{+0.6}_{-0.5}$	$10 \pm 7$	$-10 \pm 6$	$27 \pm 12$	$-3 \pm 69$
WISE 0521+1025	0.8	$0.96^{+0.08}_{-0.08}$	$0.87^{+0.58}_{-0.23}$	$-5.350^{+0.045}_{-0.043}$	$4_{-1}^{+5}$	$2.1^{+0.2}_{-0.2}$	$9\pm2$	$-7 \pm 2$	$11 \pm 5$	$17 \pm 11$
UGPS 0521+3640	0.8	$0.45^{+0.04}_{-0.04}$	$2.61^{+2.58}_{-1.29}$	$-6.139^{+0.037}_{-0.035}$	$470^{+696}_{-343}$	$3.6^{+0.3}_{-0.3}$	$2 \pm 5$	$-9 \pm 4$	$33 \pm 7$	$-3 \pm 22$
WISE 0614+0951	0.8	$0.85^{+0.07}_{-0.07}$	$4.75_{-2.29}^{+4.30}$	$-5.242^{+0.042}_{-0.040}$	$73^{+207}_{-49}$	$2.3^{+0.2}_{-0.2}$	$4\pm3$	$-6 \pm 2$	$17 \pm 5$	$4 \pm 11$
WISE 0623-0456	0.5	$0.78^{+0.17}_{-0.13}$	$13.18^{+31.26}_{-9.44}$	$-5.755^{+0.060}_{-0.049}$	$738^{+2701}_{-592}$	$3.4^{+0.6}_{-0.5}$	$7 \pm 6$	$-7 \pm 5$	$20 \pm 11$	$37 \pm 39$
UGPS 0722-0540	0.5	$0.43^{+0.04}_{-0.03}$	$0.30^{+0.30}_{-0.14}$	$-6.422^{+0.045}_{-0.042}$	$19^{+40}_{-12}$	$3.7^{+0.4}_{-0.3}$	$2 \pm 6$	$-17 \pm 6$	$33 \pm 13$	$18 \pm 36$
2MASS 0727+1710	0.5	$0.83^{+0.06}_{-0.06}$	$2.40^{+1.91}_{-1.07}$	$-5.381^{+0.031}_{-0.029}$	$29^{+46}_{-18}$	$1.9^{+0.2}_{-0.2}$	$3\pm3$	$-4 \pm 2$	$11 \pm 4$	$13 \pm 10$
2MASS 0729-3954	0.5	$0.80^{+0.14}_{-0.11}$	$8.41^{+12.40}_{-5.19}$	$-5.602^{+0.075}_{-0.069}$	$402^{+749}_{-318}$	$2.9^{+0.4}_{-0.4}$	$7 \pm 4$	$-9 \pm 4$	$13 \pm 9$	$14 \pm 37$
2MASS 0939-2448	0.5	$0.97^{+0.16}_{-0.16}$	$21.97^{+28.09}_{-12.97}$	$-5.768^{+0.066}_{-0.063}$	$1288^{+2492}_{-773}$	$3.0^{+0.3}_{-0.3}$	$7 \pm 3$	$-9 \pm 3$	$23 \pm 7$	$37 \pm 42$
ULAS 1029+0935	0.5	$0.74^{+0.06}_{-0.06}$	$0.91^{+0.91}_{-0.43}$	$-5.682^{+0.040}_{-0.038}$	$12^{+26}_{-7}$	$3.0^{+0.4}_{-0.3}$	$6 \pm 5$	$-10 \pm 4$	$21 \pm 10$	$27 \pm 21$
WISE 1039-1600	0.5	$1.20^{+0.12}_{-0.11}$	$3.20^{+3.58}_{-1.61}$	$-5.157^{+0.050}_{-0.046}$	$16^{+37}_{-10}$	$2.7^{+0.5}_{-0.4}$	$5 \pm 4$	$-6 \pm 3$	$13 \pm 8$	$19 \pm 20$
WISE 1052–1942	0.5	$0.83^{+0.08}_{-0.07}$	$1.85^{+2.07}_{-0.94}$	$-5.508^{+0.044}_{-0.042}$	$24^{+54}_{-16}$	$3.1^{+0.4}_{-0.4}$	$6 \pm 5$	$-5 \pm 4$	$25 \pm 9$	$40 \pm 22$
2MASS 1114-2618	0.5	$0.77^{+0.19}_{-0.15}$	$8.41^{+21.51}_{-6.28}$	$-5.800^{+0.062}_{-0.049}$	$519^{+1576}_{-444}$	$3.5^{+0.3}_{-0.3}$	$7 \pm 4$	$-9 \pm 3$	$23 \pm 6$	$24 \pm 30$
WISE 1124-0421	0.5	$1.02^{+0.11}_{-0.10}$	$6.27^{+6.67}_{-3.15}$	$-5.227^{+0.063}_{-0.058}$	$74^{+242}_{-50}$	$2.3^{+0.3}_{-0.3}$	$6 \pm 4$	$-7 \pm 3$	$6 \pm 7$	$30 \pm 18$
2MASS 1217-0311	0.5	$0.90^{+0.07}_{-0.06}$	$3.09^{+2.59}_{-1.44}$	$-5.326^{+0.036}_{-0.035}$	$36^{+67}_{-23}$	$2.5^{+0.2}_{-0.2}$	$0\pm 2$	$-4 \pm 2$	$16 \pm 4$	$4\pm8$
WISE 1254-0728	0.5	$0.81^{+0.09}_{-0.08}$	$2.58^{+2.75}_{-1.33}$	$-5.327^{+0.064}_{-0.060}$	$31^{+97}_{-22}$	$2.5^{+0.5}_{-0.4}$	$0 \pm 4$	$-2 \pm 3$	$12 \pm 7$	$-9 \pm 19$
WISE 1257+4008	0.5	$0.70^{+0.07}_{-0.06}$	$13.37^{+21.47}_{-8.05}$	$-5.444^{+0.043}_{-0.041}$	$709^{+2137}_{-461}$	$3.1^{+0.4}_{-0.4}$	$-3 \pm 6$	$-7 \pm 4$	$19 \pm 9$	$1 \pm 26$
Ross 458C	0.5	$0.68^{+0.06}_{-0.06}$	$2.30^{+2.32}_{-1.20}$	$-5.605^{+0.032}_{-0.036}$	$77^{+314}_{-56}$	$4.2^{+0.5}_{-0.4}$	$0 \pm 7$	$-11 \pm 6$	$32 \pm 11$	$37 \pm 18$
WISE 1322-2340	0.5	$0.93^{+0.14}_{-0.11}$	$3.26^{+4.72}_{-1.81}$	$-5.424^{+0.066}_{-0.064}$	$42^{+135}_{-30}$	$6.2^{+0.4}_{-0.4}$	$3 \pm 4$	$-6 \pm 3$	$16 \pm 7$	$-4 \pm 29$
ULAS 1416+1348	0.5	$0.67^{+0.09}_{-0.08}$	$29.63^{+19.69}_{-13.25}$	$-6.013^{+0.052}_{-0.049}$	$4544^{+3342}_{-2424}$	$3.3^{+0.4}_{-0.4}$	$7 \pm 5$	$-8 \pm 4$	$22 \pm 9$	$1 \pm 95$
WISE 1457+5815	0.5	$1.02^{+0.17}_{-0.14}$	$7.85^{+10.37}_{-4.29}$	$-5.229^{+0.122}_{-0.105}$	$110^{+281}_{-79}$	$2.3^{+0.4}_{-0.3}$	$4 \pm 4$	$-6 \pm 3$	$14 \pm 7$	$12 \pm 21$
GJ 570D	0.5	$0.79^{+0.06}_{-0.06}$	$2.03^{+1.71}_{-0.92}$	$-5.544^{+0.028}_{-0.031}$	$31^{+52}_{-20}$	$2.0^{+0.2}_{-0.2}$	$2\pm3$	$-4 \pm 2$	$16 \pm 4$	$5 \pm 14$
PSO J224+47	0.8	$0.78^{+0.08}_{-0.07}$	$1.02^{+1.00}_{-0.47}$	$-5.378^{+0.063}_{-0.059}$	$8^{+18}_{-5}$	$2.4^{+0.3}_{-0.3}$	$6\pm3$	$-6 \pm 3$	$14 \pm 6$	$-11 \pm 12$
SDSS 1504+1027	0.8	$0.97^{+0.08}_{-0.07}$	$2.47^{+2.41}_{-1.20}$	$-5.161^{+0.040}_{-0.039}$	$16^{+32}_{-10}$	$2.4^{+0.3}_{-0.2}$	$5\pm3$	$-5\pm2$	$13 \pm 5$	$10 \pm 14$
2MASS 1553+1532	0.5	$1.21^{+0.10}_{-0.09}$	$7.56^{+6.28}_{-3.42}$	$-5.072^{+0.032}_{-0.030}$	$56^{+158}_{-35}$	$2.0^{+0.2}_{-0.2}$	$3\pm3$	$-6 \pm 3$	$12 \pm 6$	$16 \pm 16$
SDSS 1628+2308	0.8	$0.74^{+0.06}_{-0.05}$	$3.57^{+3.11}_{-1.68}$	$-5.453^{+0.031}_{-0.028}$	$84^{+233}_{-56}$	$2.2^{+0.2}_{-0.2}$	$2\pm3$	$-5 \pm 2$	$17 \pm 5$	$6 \pm 11$
WISE 1653+4444	0.5	$0.60^{+0.06}_{-0.05}$	$1.84^{+2.16}_{-1.02}$	$-5.837^{+0.042}_{-0.039}$	$76^{+324}_{-56}$	$3.6^{+0.5}_{-0.4}$	$2\pm6$	$-8 \pm 5$	$32 \pm 10$	$18 \pm 26$
WISE 1711+3500	0.5	$0.93^{+0.18}_{-0.13}$	$2.17^{+5.07}_{-1.29}$	$-5.439^{+0.076}_{-0.070}$	$22^{+122}_{-16}$	$10.3^{+0.7}_{-0.6}$	$6 \pm 7$	$-8 \pm 5$	$22 \pm 12$	$-7 \pm 44$
NHOE 1511 - 2552	0.8	$0.98^{+0.12}_{-0.10}$	$1.58^{+1.51}_{-0.73}$	$-5.395^{+0.068}_{-0.064}$	$10^{+19}_{-6}$	$2.2^{+0.3}_{-0.2}$	$3\pm3$	$-5 \pm 2$	$15 \pm 6$	$0 \pm 19$
WISE 1741+2553	0.8	$0.54^{+0.05}_{-0.04}$	$0.94^{+0.85}_{-0.45}$	$-6.137^{+0.043}_{-0.039}$	$49^{+91}_{-32}$	$2.6^{+0.2}_{-0.2}$	$3\pm3$	$-11 \pm 3$	$32 \pm 6$	$8 \pm 20$
WISE 1809+3838	0.8	$0.83^{+0.09}_{-0.08}$	$1.19^{+1.28}_{-0.57}$	$-5.491^{+0.051}_{-0.049}$	$11^{+25}_{-7}$	$3.1^{+0.4}_{-0.3}$	$5\pm4$	$-8 \pm 4$	$20 \pm 8$	$28 \pm 19$
WISE 1813+2835	0.5	$0.77^{+0.08}_{-0.07}$	$3.78^{+4.24}_{-2.03}$	$-5.609^{+0.041}_{-0.039}$	$108^{+336}_{-79}$	$4.1^{+0.5}_{-0.4}$	$5 \pm 7$	$-14 \pm 6$	$28 \pm 11$	$19 \pm 27$
WISE 1852+3537	0.5	$0.86^{+0.08}_{-0.07}$	$2.76^{+2.44}_{-1.31}$	$-5.343^{+0.049}_{-0.048}$	$33^{+61}_{-21}$	$2.2^{+0.4}_{-0.3}$	$1\pm3$	$-2 \pm 2$	$14 \pm 6$	$22 \pm 13$
WISE 1959–3338	0.5	$0.68^{+0.06}_{-0.06}$	$1.54^{+1.46}_{-0.75}$	$-5.716^{+0.043}_{-0.040}$	$36^{+73}_{-24}$	$2.8^{+0.4}_{-0.3}$	$4\pm4$	$-8 \pm 4$	$20 \pm 9$	$11 \pm 21$
WISE 2000+3629	0.5 0.8	$0.82^{+0.07}_{-0.06}$ $0.69^{+0.06}_{-0.05}$	$1.26^{+1.17}_{-0.60}$ $1.20^{+1.07}_{-0.57}$	$-5.558^{+0.038}_{-0.036}  -5.609^{+0.043}_{-0.042}$	$13_{-8}^{+26} \\ 18_{-12}^{+34}$	$3.1^{+0.4}_{-0.3}$ $2.2^{+0.2}_{-0.2}$	$6 \pm 5$ $3 \pm 3$	$-10 \pm 4$ $-6 \pm 2$	$20 \pm 9$ $20 \pm 5$	$28 \pm 23$ $10 \pm 15$
WISE 2157+2659 WISE 2209_2734	0.8	$0.69_{-0.05}^{+0.16}$ $0.91_{-0.13}^{+0.16}$	$1.20_{-0.57}^{+0.57}$ $12.19_{-8.09}^{+18.62}$	$-5.609_{-0.042}^{+0.065}$ $-5.496_{-0.061}^{+0.065}$	433 <sup>+944</sup> <sub>-345</sub>	$2.2_{-0.2}$ $2.6_{-0.2}^{+0.3}$	$3 \pm 3$ $6 \pm 3$	$-6 \pm 2$ $-6 \pm 2$	$20 \pm 3$ $15 \pm 6$	
WISE 2209–2734			12.19 <sub>-8.09</sub> 176+4.87	5 212+0.061	$74^{+228}_{-49}$	$2.0_{-0.2}^{+0.3}$ $2.1_{-0.2}^{+0.3}$				$23 \pm 25$
WISE 2213+0911 WISE 2226±0440	0.5 0.5	$0.87_{-0.08}^{+0.10} \\ 0.91_{-0.11}^{+0.14}$	$4.76_{-2.35}^{+4.87} 2.05_{-1.03}^{+2.06}$	$-5.312^{+0.061}_{-0.058}$ $-5.434^{+0.106}$		$2.1_{-0.2}^{+0.3}$ $2.6_{-0.3}^{+0.3}$	$3 \pm 4$	$-6 \pm 3$ $-6 \pm 3$	$12 \pm 6$ $19 \pm 8$	$17 \pm 16$ $19 \pm 20$
WISE 2226+0440	0.5	$0.91^{+0.01}_{-0.11}$ $0.71^{+0.08}_{-0.07}$	$0.95^{+1.04}_{-0.47}$	$-5.434^{+0.106}_{-0.093}$ $-5.729^{+0.062}_{-0.061}$	$20^{+39}_{-13} \\ 15^{+35}_{-10}$	$2.0_{-0.3}^{+0.5}$ $3.1_{-0.4}^{+0.5}$	$-1 \pm 4$	$-6 \pm 3$ $-8 \pm 4$		$19 \pm 20$ $24 \pm 23$
WISE 2255–3118 WISE 2319–1844	0.5	$0.71_{-0.07}$ $0.53_{-0.06}^{+0.08}$	$3.25^{+4.96}_{-1.95}$	$-3.729_{-0.061}$ $-6.012_{-0.051}^{+0.052}$	$401^{+699}_{-322}$	$2.8^{+0.4}_{-0.4}$	$1 \pm 5$ $6 \pm 5$	$-6 \pm 4$ $-6 \pm 4$	$24 \pm 10$ $19 \pm 9$	$-10 \pm 47$
ULAS 2321+1354	0.3	$0.53_{-0.06}^{+0.06}$ $0.67_{-0.06}^{+0.06}$	$3.23_{-1.95}$ $2.89_{-1.46}^{+2.79}$	$-5.710^{+0.040}_{-0.040}$	$110^{+311}_{-77}$	$3.3^{+0.4}_{-0.3}$	$3\pm 4$	$-6 \pm 4$ $-8 \pm 3$	$\begin{array}{c} 19 \pm 9 \\ 21 \pm 7 \end{array}$	$-10 \pm 47$ $7 \pm 17$
WISE 2340–0745	0.5	$1.26^{+0.14}_{-0.13}$	$21.96^{+24.26}_{-11.25}$	$-3.710_{-0.040}$ $-4.971_{-0.060}^{+0.064}$	$305^{+503}_{-218}$	$2.2^{+0.3}_{-0.3}$	$1\pm4$	$-6 \pm 3$	$13 \pm 6$	$18 \pm 19$
WISE 4540-0745	0.5	1.20_0.13	21.90 <sub>-11.25</sub>	-4.9/1 <sub>-0.060</sub>	$303_{-218}$	∠.∠_0.3	1 _ 4	$-0 \pm 3$	$13 \pm 0$	10 ± 19

Table 5 (Continued)

								$q_{(\lambda\lambda)}$ Ç	Quantities	
Object	Slit	$R \atop (R_{\rm Jup})$	$M \over (M_{ m Jup})$	$\log(L_{ m bol}/L_{\odot}) \ ({ m dex})$	Age (Myr)	$\epsilon_{J} \ (\%)$	$q_Y \ (\%)$	$q_J$ (%)	$q_H \ (\%)$	$q_K$ (%)
WISE 2348-1028	0.5	$0.74^{+0.08}_{-0.07}$	$2.70^{+2.72}_{-1.35}$	$-5.477^{+0.059}_{-0.056}$	52+219	$2.7^{+0.4}_{-0.3}$	1 ± 4	$-5 \pm 3$	15 ± 7	12 ± 18

Notes. Radii (R) are derived from the objects' parallaxes and spectroscopically inferred  $\log\Omega$ . Mass (M) is derived from R and the fitted  $\log g$ . Bolometric luminosity  $\log(L_{\rm bol}/L_{\odot})$  is derived from integrating the objects'  $1.0-2.5~\mu{\rm m}$  SpeX spectra and fitted model spectra to shorter and longer wavelengths spanning  $0.4-50~\mu{\rm m}$ , with spectra scaled by the measured parallaxes (Section 3.2). Age is derived from the spectroscopically inferred  $T_{\rm eff}$ ,  $\log g$ , and Z, and the cloudless Sonora–Bobcat evolutionary models (Section 5.2). The measure of the data–model discrepancy ( $\epsilon_I$ ) is derived from the fitted hyperparameters  $a_N$  and  $a_G$ , as well as from the objects' J-band peak fluxes (Section 6). The measure of spectral-fitting residuals in the YJHK bands,  $q(\lambda\lambda)$ , is defined in Equation (2) and computed using the objects' observed spectra and their fitted model spectra (Section 6.2).

 Table 6

 Typical Parameter Uncertainties for Our Forward-modeling Analysis

Method	T <sub>eff</sub> (K)	log g (dex)	Z (dex)	$(\text{km s}^{-1})$	$v \sin i (\text{km s}^{-1})$	$\log \Omega$ (dex)	R (R <sub>Jup</sub> )	$M \over (M_{\rm Jup})$
Starfish								
formal	20	0.22	0.102	127	21	0.049	0.06	1.3
adopted	28	0.29	0.154	220	29	0.073	0.08	1.9
Traditional								
formal	3	0.02	0.011	29	20	0.006	0.03	0.2
adopted	3	0.02	0.011	183	20	0.024	0.04	0.3

**Notes.** The formal uncertainties are obtained directly from the spectral-fitting process and the adopted uncertainties are those with systematic errors incorporated (Section 3.1 and Appendix C). We only show the formal uncertainties if they are different from the adopted ones.

## 3.2.1. Impact of S/N and Spectral Resolution

Our near-infrared spectra span a wide range in J-band S/N<sup>9</sup> from 15 to 180 (Table 1), and here we examine the impact of the S/N on the precision of our fitting results. Figure 4 plots the uncertainties of the eight physical parameters  $\{T_{\rm eff}, \log g,$  $Z, v_r, v \sin i, \log \Omega, R, M$  as a function of the *J*-band S/N. The uncertainties of the first six parameters have a significant spread at low S/N, but then shrink to small values at S/N  $\gtrsim$  50. We note the Starfish-derived parameter errors at high S/N (\$\geq 50) are in fact dominated by modeling systematics (instead of measurement uncertainties), which constitute  $\approx$ 2%–4% of the peak J-band flux of the late-T dwarf spectra (see Section 6.1) and cause the parameter precision to be independent of the data S/N in this regime. The precision of R and M depends not only on the S/N of the spectra but also on the parallax uncertainties. The R and M uncertainties of objects with higher-precision parallaxes (e.g., relative uncertainties  $\lesssim$ 5%) have the same dependence on S/N as the first six physical parameters.

We also investigate the impact of spectral resolution, since our sample contains spectra observed with both the 0.75 ( $R \approx 80$ –250) and 0.78 ( $R \approx 50$ –160) slits. As shown in Figure 4, the radial velocity uncertainties derived from the lower-resolution spectra are systematically larger than those from the higher-resolution ones, as expected, but such distinction between the two resolutions is not seen for the other parameters.

Two objects in our sample, WISEPA J171104.60+350036.8 (WISE 1711+3500; Kirkpatrick et al. 2011) WISE J004945.61+215120.0 (WISE 0049+2151; Mace et al. 2013a), have spectra taken with both slits. Comparing results from each object with the two resolutions, we find almost all parameters are consistent within  $0.6\sigma$ . The only exception is the radial velocity of WISE 1711+3500, where the inferred values between the two slits differ by  $2.1\sigma$ . WISE 1711+3500 is a resolved 0".78 T8+T/Y binary (Liu et al. 2012; also see Section 4), so the two slits will exclude different amounts of the integrated light from the system and may cause the discrepant radial velocities. Also, the *J*-band S/N of this object's 0."5 spectrum is quite low ( $\approx$ 20) as compared to that of the 0."8 spectrum (S/N  $\approx$  35), so the radial velocity inferred from the 0".5 spectrum might be less accurate. 10

#### 3.2.2. Parameter Correlations via Stacked Posteriors

We now investigate the correlations between the physical parameters  $\{T_{\rm eff}, \log g, Z, v_{\rm r}, v \sin i, \log \Omega, R, M\}$ . The correlations can shed light on how parameters change when one is under- or overestimated. This information is useful when we examine the results from previous forward-modeling analyses (e.g., Cushing et al. 2008; Stephens et al. 2009), which relied only on solar-metallicity model atmospheres to analyze ultracool dwarfs, which might have subsolar or supersolar metallicities.

<sup>&</sup>lt;sup>a</sup> WISE 0245–3450 lacks a parallax and thus has no radius, mass, or bolometric luminosity results.

<sup>&</sup>lt;sup>9</sup> The median S/N around the *J*-band peak, i.e., 1.2–1.3  $\mu$ m, of the object's spectra.

 $<sup>\</sup>overline{^{10}}$  The *J*-band S/N of WISE 0049+2151 (which does not show the discrepant atmospheric parameters between the two slits) is  $\approx$ 80 for its 0.75 spectrum and  $\approx$ 35 for its 0.78 spectrum.

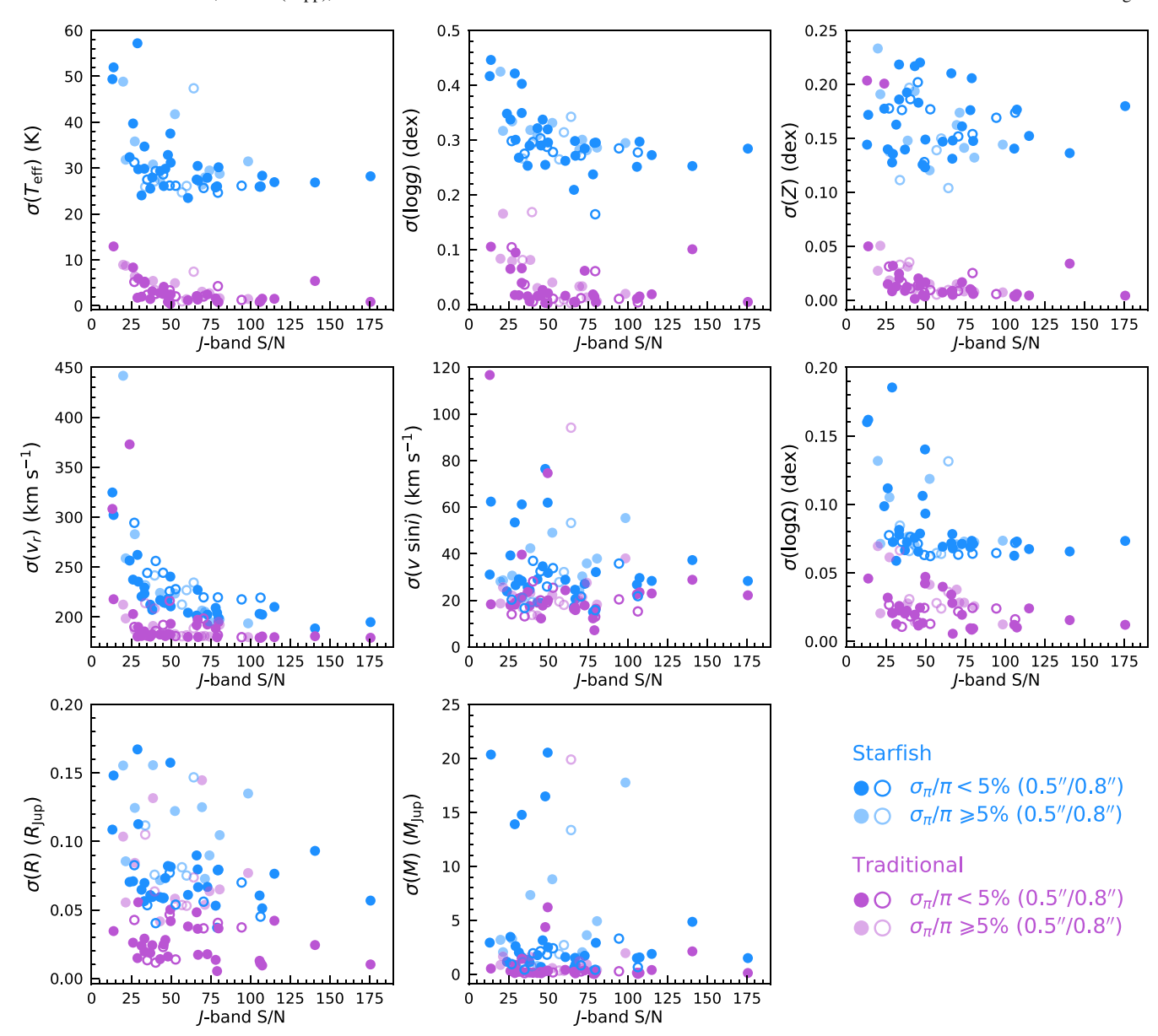


Figure 4. Parameter uncertainties from Starfish (blue) and traditional (purple; Appendix C) forward-modeling analysis as a function of the *J*-band S/N, i.e., the median S/N in 1.2–1.3  $\mu$ m. We use solid circles for results from spectra taken with the 0.75 slit and open circles for the 0.78 slit. The uncertainties of  $\{T_{\rm eff}, \log g, Z, \nu_{\rm r}, \nu \sin i, \log \Omega\}$  have a significant spread at low S/N, but then shrink to lower values at S/N  $\gtrsim$  50. Such trends also hold for the *R* and *M* uncertainties of objects with high-precision parallaxes (e.g.,  $\sigma_{\pi}/\pi < 5\%$ ). The  $\nu_{\rm r}$  uncertainties derived from the lower-resolution spectra (0.78 slit) are systematically larger than those from the higher-resolution ones as expected. Also, the  $\nu_{\rm r}$  uncertainties from both the Starfish and traditional spectral-fitting methods are larger than the 180 km s<sup>-1</sup> uncertainty in the wavelength calibration of the SpeX prism data.

To investigate the parameter correlations, we stack the parameter posteriors of all our late-T dwarfs that are directly from the formal spectral fitting and have no systematic errors incorporated. For each object's chain, we first subtract the median of each posterior so that the chain then represents the deviations of the posteriors from the median values, which we denote as  $\Delta T_{\rm eff}$ ,  $\Delta \log g$ ,  $\Delta Z$ , etc. Then we concatenate all the modified chains to generate the stacked parameter posteriors (Figure 5). We use these stacked posteriors to compute the Pearson correlation coefficients between all pairs of parameters.

We find that four pairs exhibit significant correlations:  $(\Delta T_{\rm eff}, \Delta \log \Omega)$ ,  $(\Delta R, \Delta M)$ ,  $(\Delta \log g, \Delta v \sin i)$ , and  $(\Delta \log g, \Delta Z)$ . The correlations within the first three pairs are expected: (1) the effective temperature and solid angle are naturally correlated due to the Stefan–Boltzmann law; (2) the mass is computed from the radius and surface gravity and has a stronger dependence on radius; and (3) the inferred  $v \sin i$  value of each object is primarily constrained by the prior, which is determined by the surface gravity, solid angle, and distance (Section 3.1 and Equation (2) of Paper I).

The fourth correlation between  $\log g$  and Z is interesting. Conducting an orthogonal distance regression to the modified chains of  $\Delta \log g$  and  $\Delta Z$  using a straight line across the origin, we derive the following relation:

$$\Delta \log g = 3.42 \times \Delta Z. \tag{1}$$

<sup>11</sup> We note the parameter correlation involves the change of the parameters' median values (due to the intrinsic parameter degeneracy). The systematic errors incorporated into our results only slightly inflate the parameter uncertainties (instead of their median values; Section 3.1) and thus have no impact on the parameter correlations that we investigate here.

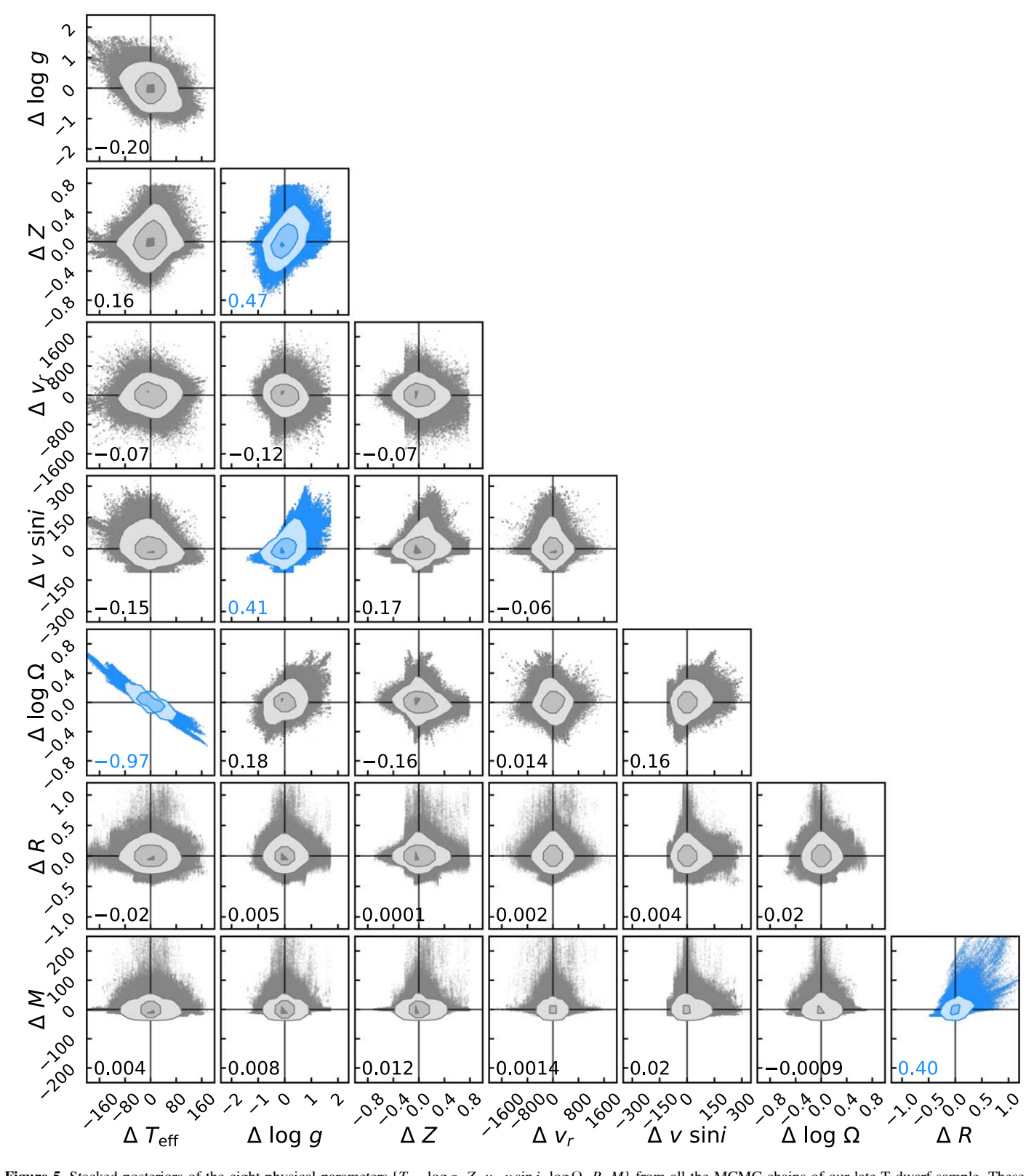
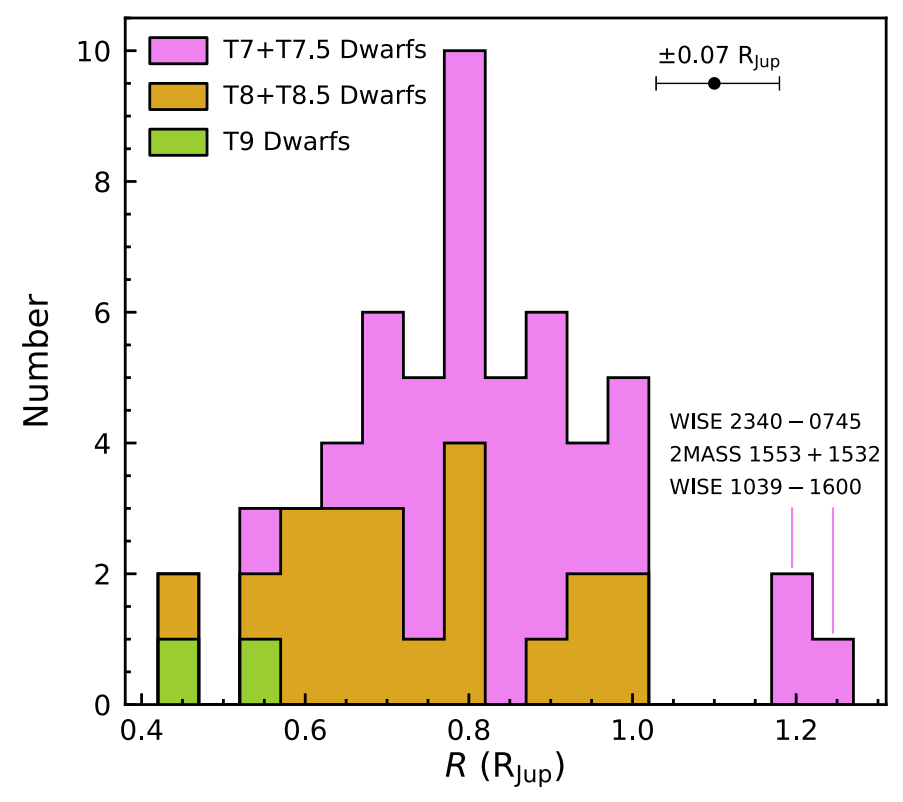


Figure 5. Stacked posteriors of the eight physical parameters  $\{T_{\rm eff}, \log g, Z, v_{\rm r}, v \sin i, \log \Omega, R, M\}$  from all the MCMC chains of our late-T dwarf sample. These chains have been subtracted by their medians, so they represent the deviations of the parameter posteriors from the median values, which we denote as  $\Delta T_{\rm eff}$ ,  $\Delta \log g$ ,  $\Delta Z$ , etc. We stack all the modified chains, generate stacked posteriors, and compute the Pearson correlation coefficients between each pair of parameters and give the coefficient value in the lower left corner of each panel. Most of the parameter pairs have very weak correlations (gray) with the absolute values of their coefficients below 0.2. We find four parameter pairs (blue) with large correlation coefficients (absolute values above 0.4):  $(\Delta T_{\rm eff}, \Delta \log \Omega)$ ,  $(\Delta R, \Delta M)$ ,  $(\Delta \log g, \Delta v \sin i)$ , and  $(\Delta \log g, \Delta Z)$ . The strong correlations within the first three pairs are as expected, while the fourth one suggests a  $\log g - Z$  degeneracy (Equation (1)) in our forward-modeling analysis.



**Figure 6.** Distribution of our derived atmospheric radii for late-T dwarfs (violet for T7 and T7.5, orange for T8 and T8.5, and green for T9). We label the three objects whose radii stand out with large values, among which 2MASS 1553+1532 is a resolved binary and the other two are candidate binaries (Section 4).

The qualitative form of such a  $\log g - Z$  relation has been noted from previous spectroscopic analyses using other model atmospheres (e.g., Burgasser et al. 2006a; Leggett et al. 2007; Liu et al. 2007; Burningham et al. 2009). The cause of this degeneracy is that these two parameters have similar effects on the spectral morphology of cloudless model atmospheres, as either a high (low) logg or a low (high) Z leads to the same suppressed (enhanced) K-band flux in late-T dwarf spectra. In addition, we find that Z has a noticeable correlation only with the logg parameter in our analysis, suggesting that applying the solar-metallicity cloudless Sonora–Bobcat models to late-T dwarfs whose true metallicities are nonsolar can bias  $\log g$  but not the other parameters.

## 4. Binary Systems

Now we examine binary systems in our sample, for which our derived atmospheric model properties will not be reliable. This is because some of the integrated light from these systems might be missing from our prism spectra (depending on their angular separations relative to the 0."5 and 0."8 slit widths), and our spectral-fitting process assumes all objects are single. We first discuss known resolved binaries (Section 4.1) and then identify candidate binaries based on their spectrophotometric properties (Section 4.2). In the end, we exclude six known or likely binaries from our subsequent discussions.

#### 4.1. Resolved Binaries

Three late-T dwarfs in our sample are known to be resolved binaries: 2MASSI J1553022+153236 (2MASS 1553+1532), WISE 1711+3500, and WISEPA J045853.89+643452.9 (WISE 0458+6434). 2MASS 1553+1532 (T7) is a resolved

 $0.''35\,T6.5+T7$  binary (Burgasser et al. 2006c), with a bolometric luminosity ratio of  $0.31\pm0.12\,\mathrm{mag}$  and a mass ratio of  $0.90\pm0.02^{.12}\,\mathrm{Our}$  fitted model spectra of this object match the observed spectrum, but the fitted  $R=1.21^{+0.10}_{-0.09}\,R_{\mathrm{Jup}}$  stands out from our sample (Figure 6) and is larger than the evolutionary model predictions ( $\approx0.75-1.20\,R_{\mathrm{Jup}}$ ; e.g., Burrows et al. 1997; Saumon & Marley 2008; Marley et al. 2021, submitted), as well as the directly measured radii of transiting brown dwarfs, e.g., KELT-1b ( $1.116^{+0.038}_{-0.09}\,R_{\mathrm{Jup}}$ ; Siverd et al. 2012), KOI-205b ( $0.81\pm0.02\,R_{\mathrm{Jup}}$ ; Díaz et al. 2013), and LHS 6343 C ( $0.783\pm0.011\,R_{\mathrm{Jup}}$ ; Montet et al. 2015). The large radius of 2MASS 1553+1532 is in accord with its nearly-equal-brightness binarity. A similar large spectroscopic radius ( $R=1.59^{+0.14}_{-0.09}\,R_{\mathrm{Jup}}$ ) was inferred by Line et al. (2017) based on their retrieval analysis, which also did not account for binarity.

WISE 1711+3500 (T8) is a resolved 0."78 T8+T/Y binary (Liu et al. 2012). The binary has near-infrared (*YJHK*-band) flux ratios of 2.6–3.1 mag, indicating the integrated-light spectra of this system are dominated by the T8 primary. This might explain why its fitted radius  $R = 0.93^{+0.16}_{-0.12} R_{\text{Jup}}$  is not as large as that of the nearly-equal-brightness binary 2MASS 1553+1532.

WISE 0458+6434 (T8.5) is a resolved 0."51 T8.5+T9 binary (Gelino et al. 2011; Burgasser et al. 2012; Leggett et al. 2019)

 $<sup>\</sup>overline{12}$  Burgasser et al. (2006c) estimated the bolometric luminosity of binary components using their Hubble Space Telescope (HST)/NICMOS resolved photometry and a bolometric correction, which they derived as a function of near-infrared colors using the photometry of unresolved T dwarfs in their sample and the *K*-band bolometric correction from Golimowski et al. (2004). Burgasser et al. estimated the mass of the binary components using the objects effective temperatures based on the Golimowski et al. (2004)  $T_{\rm eff}$ –spectral type (SpT) relation, an assumed age of 0.5–5.0 Gyr, and the Burrows et al. (1997) evolutionary models.

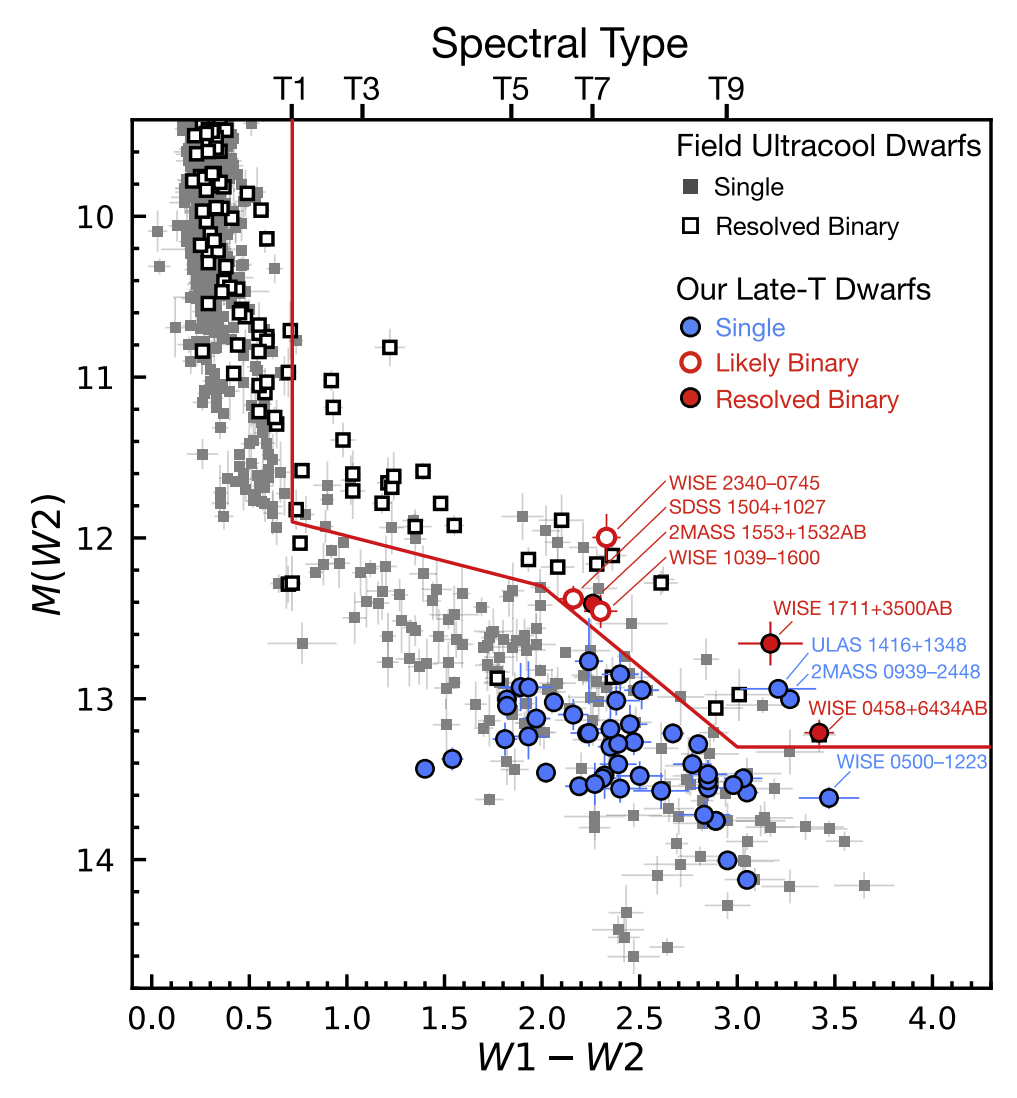


Figure 7. W2-band absolute magnitudes as a function of W1-W2 colors for our late-T dwarfs and field ultracool dwarfs (Best et al. 2020a) whose absolute magnitudes and colors both have S/N > 5. We use red solid circles for resolved late-T binaries in our sample (Section 4.1), red open circles for likely binaries (Section 4.2), and blue solid circles for the rest. For the field objects, we use white squares for resolved ultracool binaries and solid squares for those that are single or have unknown binarity. The upper x-axis shows the corresponding T spectral types based on the median W1-W2 colors of field dwarfs from Best et al. (2018). We draw a line in the diagram to help distinguish the T-type resolved binaries from the others, with the boundary defined by points of (W1 - W2, M(W2)) = (0.72, 9.4), (0.72, 11.9), (2, 12.3), (3, 13.3), and (4.5, 13.3). T-type binaries tend to have brighter magnitudes and redder colors than the boundary in this diagram, but we caution that low-metallicity, high-gravity single objects might occupy the same area as the resolved binaries (Section 4.2).

with near-infrared (*JHK*-band) flux ratios of 1.0–1.1 mag. The fitted model spectra from our analysis do not match the observed spectrum and predict too faint *H*-band fluxes. Also, this object's parameter posteriors are bimodal based on the traditional method (Appendix C), with one peak consistent with the Starfish results and the other peak 160 K cooler in  $T_{\rm eff}$ , 1.5 dex higher in logg, and 0.2 dex higher in *Z*. While the bimodal posteriors might be due to the object's binarity, they are likely caused by the low *J*-band S/N = 24 of the data, which prevents the spectral-fitting process from converging on a unique set of solutions.

We exclude all these three known binaries from our subsequent analysis (Sections 5 and 6).

#### 4.2. Candidate Binaries

Here we choose three criteria to identify candidate binaries in our sample based on their fitted model parameters and observed photometry:

- (1) the fitted R are outliers in the derived radius distribution of our sample (Figure 6) with very large values (e.g.,  $\gtrsim 1.2 R_{\text{Jup}}$ );
- (2) the parameter posteriors derived from either Starfish or traditional forward-modeling analysis are bimodal; or
- (3) the AllWISE photometry is brighter and redder than that of most other objects in our sample, with the critical values shown in Figure 7.

Figure 7 compares the integrated-light photometry of our late-T dwarfs to that of known field dwarfs from Best et al. (2020b), which shows that T-type resolved binaries have distinctly brighter W2-band absolute magnitudes and redder W1-W2 colors than the majority of field dwarfs that are single (or not known to be binaries). We draw a line in Figure 7 to help distinguish the resolved binaries from the others. We caution that this line can also select single objects with highgravity, metal-poor atmospheres, as demonstrated by 2MASS 0939-2448 and ULAS 1416+1348 (discussed further

below). Either high gravity or low metallicity can cause the objects' photospheres to reside at higher pressures, favoring the formation of CH<sub>4</sub> (with strong absorption in W1) over that of CO (with strong absorption in W2; e.g., Liebert & Burgasser 2007; Zahnle & Marley 2014; Leggett et al. 2017). This leads to redder W1–W2 colors and might make such objects have similar AllWISE photometry as binaries.

We select candidate binaries whose properties satisfy at least one of our criteria, and end up with six objects: WISE J103907.73–160002.9 (WISE 1039–1600), WISEPC J234026.62–074507.2 (WISE 2340–0745), WISEPA J050003.05–122343.2 (WISE 0500–1223), 2MASS J09393548–2448279 (2MASS 0939–2448), ULAS 1416+1348, and SDSS J150411.63+102718.4 (SDSS 1504+1027). Based on recent near-infrared adaptive optics imaging (M. Liu 2021, private communication), all these candidates are unresolved down to 0.11, making their potential binarity intriguing.

WISE 1039–1600 (T7.5) and WISE 2340–0745 (T7) are selected by both the first and third criteria, with their spectroscopically inferred radii among the largest in our sample (Figure 6) and their AllWISE photometry being anomalous (Figure 7). The fitted model spectra of these two objects match the observed spectra, so their large radii are unlikely to be caused by poorly fitted models. Also, their kinematics do not support membership in any young associations (based on BANYAN  $\Sigma$ (Gagné et al. 2018) or LACEWING (Riedel et al. 2017); see Zhang et al. 2021) and their fitted logg are consistent with the other late-T dwarfs in our sample. Therefore, we find no evidence of youth that would lead to their large radii (e.g., Burrows et al. 2001; Kirkpatrick et al. 2008; Allers & Liu 2013). In addition, their near-infrared spectra do not exhibit any peculiarities that might result from high-gravity, metal-poor atmospheres. Therefore, we conclude their large atmospheric radii and atypical AllWISE photometry are likely caused by binarity.

WISE 0500–1223 (T7) is selected by the second criterion, i.e., bimodal posteriors from atmospheric model analysis. Similar to those of WISE 0458+6434, the parameter posteriors of this object based on traditional forward-modeling analysis have two peaks, with one consistent with the Starfish results, and the other 120 K cooler in  $T_{\rm eff}$ , 1.5 dex higher in  $\log g$ , and 0.4 dex higher in Z. The W2-band absolute magnitude is fainter than our critical line in Figure 7, although this line is not well established around the  $W1-W2=3.47\pm0.16$  mag of WISE 0500–1223, given that there are too few known binaries with such red colors. While the bimodal posteriors of this object could be caused by binarity, we note the low J-band S/N  $\approx$  13 of the data might also cause this anomaly. We thus suggest a reanalysis of this system using higher-quality data.

The remaining three candidates are all selected by the third criterion, i.e., anomalous AllWISE photometry. 2MASS 0939–2448 (T8) has a metal-poor atmosphere given its broad Y-band and faint K-band spectra. We derive a low metallicity,  $Z=-0.41^{+0.15}_{-0.09}$  dex, which is consistent with past forward-modeling (Burgasser et al. 2006a, 2008b; Leggett et al. 2009) and retrieval analyses (Line et al. 2017). Combining near-infrared and mid-infrared spectra, both Burgasser et al. (2008b) and Leggett et al. (2009) have suggested 2MASS 0939–2448 is an unresolved binary, primarily due to its uncommon brightness in the mid-infrared. However, Dupuy & Liu (2012) suggested that 2MASS 0939–2448 might be a single object with a very red W1–W2 color due to its low metallicity and/or high gravity, given that its near-infrared

absolute magnitudes are not brighter than those of field dwarfs with similar spectral types.

ULAS 1416+1348 (T7.5) is a 9" (85 au) companion (Burningham et al. 2010a; Scholz 2010a) to an L6 dwarf, SDSS J141624.08+134826.7 (Bowler et al. 2010a; Schmidt et al. 2010). 13 Burningham et al. (2010a) noted the unusually red H-W2 and W1-W2 colors of this object and connected these properties to its metal-poor atmosphere. The very blue Y-K color of this companion suggests high gravity and low metallicity, in accord with our derived  $\log g = 5.21^{+0.26}_{-0.25}$  dex and  $Z = -0.39^{+0.14}_{-0.11}$  dex, which are consistent with past spectral analyses (Burgasser et al. 2010b; Line et al. 2017; Gonzales et al. 2020). <sup>14</sup> Kirkpatrick et al. (2019) suggested ULAS 1416 +1348 is an unresolved binary, given that three known late-T subdwarfs (BD +01° 2920B (Pinfield et al. 2012), Wolf 1130C (Mace et al. 2013b), and WISE J083337.82+005214.1 (Pinfield et al. 2014)) have similar positions as field dwarfs in the  $M_H$  versus H-W2 diagram whereas ULAS 1416+1348 is an apparent outlier.

SDSS 1504+1027 (T7) has a normal near-infrared spectrum given its spectral type, and our fitted model spectra match the data (*J*-band S/N of 50 per pixel). Aberasturi et al. (2014) obtained high-spatial-resolution images using HST/WFC3 and did not resolve this object down to a resolution of 0.006-0.142 and a magnitude contrast of 1.5-2.0 mag.

To conclude, we flag WISE 1039–1600, WISE 2340–0745, and SDSS 1504+1027 as likely binaries, and exclude them from our subsequent analysis (Sections 5 and 6) along with the three known binaries discussed in Section 4.1. For the remaining candidates, WISE 0500–1223, 2MASS 0939–2448, and ULAS 1416+1348, we keep them in our analysis, given that their anomalous spectrophotometry is likely caused by low-S/N data or abnormal atmospheres. However, we do not rule out the possibility that these objects are tight unresolved binaries.

#### 5. Atmospheric Properties of Late-T Dwarfs

Here we examine our forward-modeling results on the distributions of metallicities (Section 5.1) and ages (Section 5.2) of late-T dwarfs, as well as their effective temperature–spectral type relation (Section 5.3). We demonstrate the spectral-fitting results for an ensemble of objects can provide useful diagnostics about the physical assumptions made within model atmospheres, by virtue of having a large sample of spectra over a focused spectral type range (as opposed to a smaller sample of objects spanning a wide spectral type range).

 $<sup>\</sup>overline{^{13}}$  The primary has weak TiO and CaH absorption features in the optical, an unusually blue  $J\!-\!K$  color, enhanced FeH 0.99  $\mu\mathrm{m}$  absorption, deep H<sub>2</sub>O absorption features, and thin-disk kinematics (e.g., Bowler et al. 2010a; Schmidt et al. 2010). Bowler et al. (2010a) suggested these features are caused by the object's low metallicity and its less opaque condensate clouds compared to those of the majority of L6 dwarfs (similar to the features of the blue L4.5 dwarf 2MASS J11263991–5003550 as discussed by Burgasser et al. 2008a). The metallicity and age of the system are not well constrained as compared to the three benchmark companions (HD 3651B, GJ 570D, and Ross 458C) studied in Paper I.

<sup>&</sup>lt;sup>14</sup> The best-fit parameters derived by Burgasser et al. (2010b) using the Saumon & Marley (2008) spectral models also favor a weak-mixing atmosphere with vertical diffusion coefficients of  $K_{zz} = 10^4$  cm<sup>2</sup> s<sup>-1</sup>.

#### 5.1. Metallicity Distribution

We investigate the metallicities of 49 late-T dwarfs<sup>15</sup> in our sample (with the other six objects excluded due to their known or likely binarity; Section 4) and compare them to the metallicities of nearby stars. This analysis can in principle assess whether these two populations have similar formation histories but it can also shed light on the accuracy of our fitted atmospheric properties.

Spectroscopic analysis of stellar metallicities and elemental abundances involves (1) measuring the equivalent widths of individual absorption lines and then converting them into abundances using the curve of growth and theoretical line lists (e.g., Edvardsson et al. 1993; Santos et al. 2004; Bond et al. 2006; Ramírez et al. 2013; Soto & Jenkins 2018), or (2) fitting the entire observed spectra using stellar model atmospheres with a range of abundances (e.g., Valenti & Fischer 2005; Jenkins et al. 2008; Petigura & Marcy 2011; Brewer et al. 2016). The abundances of several thousands of nearby (≤100 pc) stars have been studied via high-resolution spectroscopy  $(R \ge 3 \times 10^4)$ . The vast majority of these stars have similar iron content ([Fe/H]) to our Sun (e.g., Figure 4 of Hinkel et al. 2014). While it has been known that different methods, line lists, and spectral resolutions can lead to notable spreads in the derived metallicities and elemental abundances (e.g., Torres et al. 2012; Smiljanic et al. 2014; Hinkel et al. 2016; Ivanyuk et al. 2017), much effort has been made to construct large, homogeneous stellar abundance catalogs (e.g., Hinkel et al. 2014, 2017; Brewer et al. 2016).

In contrast, systematic metallicity analysis of substellar objects has been lacking in most spectroscopic studies. For late-type ultracool dwarfs, direct metallicity measurements from atomic/ molecular absorption features are particularly challenging, given that (1) the spectral continuum required for computing absorption depths is hard to determine due to the presence of very broad molecular bands (e.g., H<sub>2</sub>O and CH<sub>4</sub>) and (2) elemental abundances cannot be entirely tracked by the observed absorption features, as some portions of species might have been perturbed by vertical mixing and/or sequestered into condensates and thereby sinking to below the photosphere (e.g., Fegley & Lodders 1994; Line et al. 2017). Metallicity estimates are viable when using model atmosphere analyses. While there have been previous such studies of one to a few objects (e.g., Saumon et al. 2007; Bowler et al. 2010b; Leggett et al. 2017), many analyses have used models with only the solar metallicity (e.g., Cushing et al. 2008; Del Burgo et al. 2009; Stephens et al. 2009; Liu et al. 2011b; Schneider et al. 2015; Deacon et al. 2017).

Recently, some studies have begun characterizing metallicities for large samples of ultracool dwarfs. Zhang et al. (2017, 2018b) studied 28 M7–L7 subdwarfs with thick-disk or halo membership. They determined the objects' physical properties by visually comparing their optical and near-infrared spectra to BT-Settl model atmospheres (Allard et al. 2011; Allard 2014) and found low [Fe/H] values, spanning -2.5 to -0.5 dex. Leggett et al. (2017) visually compared near-infrared spectra of 20 Y dwarfs to the Tremblin et al. (2015) models, which assume cloudless atmospheres with disequilibrium chemistry and reduced vertical temperature gradients, and found solar-like metallicities with a spread of  $\pm 0.3$  dex.

Line et al. (2017) conducted a retrieval analysis for 11 late-T dwarfs and found notably lower metallicities (spanning -0.4 to 0.1 dex) and higher carbon-to-oxygen ratios (C/O) compared to those of nearby FGK stars. These results are likely related to the sequestration of oxygen into condensates in late-T atmospheres, which then rain out of the photosphere (e.g., Fegley & Lodders 1994; Marley & Robinson 2015), resulting in retrieved metallicities and C/O that are systematically too low and high, respectively. Applying the Line et al. (2017) methodology to 14 late-T and Y dwarfs, Zalesky et al. (2019) derived metallicities that span -0.2 to 0.6 dex, which are consistent with (if not slightly higher than) those of nearby stars.

Our work analyzes 49 late-T dwarfs and thus constitutes the largest homogeneous analysis of brown dwarf metallicities to date. Figure 8 compares the derived metallicities of our late-T dwarfs to those of F0-M4 stars from the Hypatia catalog 16 (Hinkel et al. 2014, 2016, 2017). The latest version of this catalog (of 2019) June, compiling nearly 200 literature studies) contains 6196 stars within 150 pc that have spectroscopically determined [Fe/H] and at least one other element. This compilation of stellar abundance is homogeneous in a sense that Hinkel et al. carefully examined the results reported by different studies for the same element within the same star and normalized all abundances to the same solar scale by Lodders et al. (2009). We only include thin-disk Hypatia stars (5021 objects) in our analysis and find these objects have a median metallicity of Z = 0.04 dex with a  $1\sigma$  confidence interval (i.e., 16th to 84th percentiles) of -0.21 to 0.22 dex. In comparison, our 49 late-T dwarfs have much lower metallicities, spanning -0.43 to  $0.23 \, \text{dex}$  and with a median and mode of  $-0.24 \, \text{dex}$  and -0.40 dex, respectively. We run the Kolmogorov-Smirnov (K-S) test for the metallicities of the Hypatia stars and our late-T dwarfs in a Monte Carlo fashion  $^{17}$  and obtain p-values that are all smaller than  $2 \times 10^{-3}$ , indicating they are not drawn from the same distribution. These two samples' metallicity distributions are largely unchanged when we limit our comparison to ≤25 pc for our late-T dwarfs (47 objects) and the Hypatia stars (590 objects; Figure 8), with the K-S test providing similarly small p-values of <0.02 (with a median of  $2 \times 10^{-7}$ ).

To examine whether the metallicity discrepancy between the late-T and stellar populations is physical, we first analyze the accuracy of our derived Z values. As shown in Figure 9, 30 late-T dwarfs have Z of -0.43 to -0.21 dex, which are  $>1\sigma$  lower than the Hypatia stellar metallicity. Most of these objects have R=0.75-1.2  $R_{\rm Jup}$  from our atmospheric modeling, consistent with the evolutionary model predictions and directly measured radii of transiting brown dwarfs (see Section 4.1). The remaining 19 (= 49 - 30) late-T dwarfs have higher Z of -0.15 to 0.23 dex, which are consistent with those of the Hypatia stars, but most of these objects have unphysically small radii of <0.75  $R_{\rm Jup}$ . Overall, we find a correlation between Z and R, where objects with higher Z in our sample tend to have smaller R from our atmospheric model analysis.

This *Z–R* correlation is in contradiction to the cloudless Sonora–Bobcat evolutionary models, which predict that objects

 $<sup>\</sup>overline{^{15}}$  Among these objects, WISE 0049+2151 has two sets of atmospheric model parameters, derived from 0."5 and 0."8 spectra (Section 3.2.1). These results are consistent, and we use those determined from the higher-S/N 0."5 spectrum.

<sup>16</sup> https://www.hypatiacatalog.com/hypatia

 $<sup>^{17}</sup>$  We generate  $10^4$  distributions of Hypatia stellar metallicities, with each distribution constructed by a random draw from each object's measured Z and errors by assuming a Gaussian distribution. We generate  $10^4$  distributions of our late-T dwarfs' metallicities in the same approach except that we draw each object's metallicity from its atmospheric-based Z posterior. We then run the K-S test for each pair of Hypatia and late-T distributions and compute the corresponding p-values.

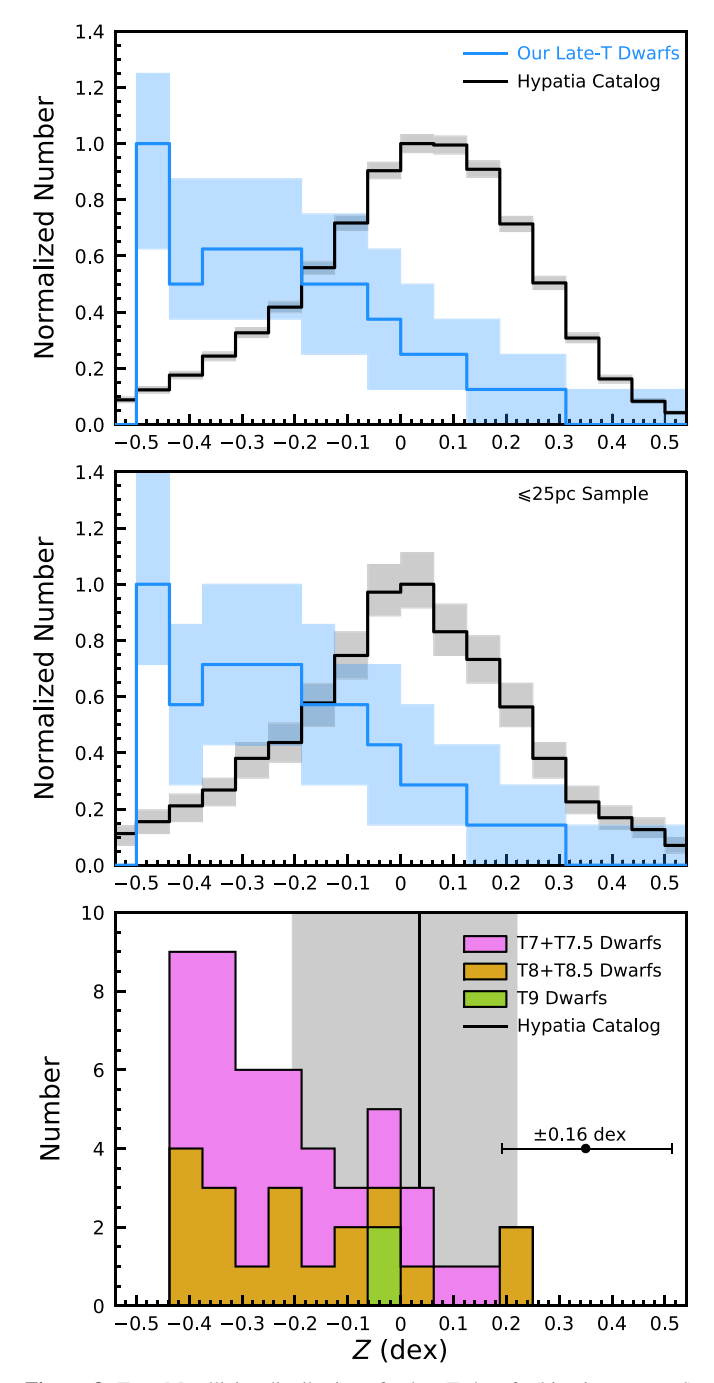


Figure 8. Top: Metallicity distributions for late-T dwarfs (binaries removed) from our atmospheric model analysis and for thin-disk stars from the Hypatia catalog (Hinkel et al. 2014, 2016, 2017). For our late-T dwarfs, we generate  $10^4$  metallicity distributions, each constructed by a random draw from each object's Z posterior. We then plot the median and the  $1\sigma$  confidence interval of these distributions using a blue line and shadow, respectively. The distributions for the Hypatia stars (black) are produced in the same approach except that we assume the metallicity of each star follows a Gaussian distribution. We normalize these two types of distributions so that their peaks correspond to one. Middle: Same format as that of the top but with the late-T and stellar samples constrained to  $\leq 25$  pc. Bottom: The distribution of our late-T dwarfs, with the violet color for T7 and T7.5, orange for T8 and T8.5, and green for T9. Our typical Z uncertainty is shown as a black error bar. We use a vertical black line and gray shadow to mark the median (0.04 dex) and the  $1\sigma$  spread (-0.21 to 0.22 dex) of the Hypatia stars.

with higher metallicities should have increased atmospheric opacity, slower cooling, and thereby larger radii at a given mass and age (also see Burrows et al. 2011). Also, this correlation is

not found in stacked posteriors of atmospheric parameters (Figure 5). Therefore, it is likely not due to the parameter degeneracy within the Sonora–Bobcat models or to our spectral-fitting machinery.

This Z–R trend might be due to the spectroscopically inferred Z or R of our late-T dwarfs being underestimated. As shown in Paper I, the fitted metallicities of the two benchmark companions HD 3651B and GJ 570D are underestimated by  $\approx$ 0.35 dex but their fitted radii are reliable, when compared to the radii derived from the Sonora-Bobcat evolutionary models (using these companions' bolometric luminosities and their primary stars' ages and metallicities). For the other benchmark, Ross 458C, its fitted metallicity is consistent with evolutionary-based results but its fitted radius is underestimated by a factor of  $\approx$ 1.6. Among our sample, some objects with fitted Z < -0.21 dex and  $R \ge 0.75 R_{Jun}$ might be in similar situations to HD 3651B and GJ 570D, while those with fitted  $Z \ge -0.21$  dex and R < 0.75  $R_{Jup}$  might be in a similar situation to Ross 458C. All together, correcting the inaccurate atmospheric parameters of these late-T dwarfs would be the equivalent of shifting their Z toward higher values and/or their R toward larger values, which would alter the Z–R correlation seen in Figure 9. The underestimation of these fitted parameters in our sample suggests the model assumptions of cloudless and chemical-equilibrium atmospheres are not adequate to fully interpret late-T dwarf spectra and should be further improved.

To conclude, many of our late-T dwarfs with low atmospheric Z might have values underestimated by as large as 0.3–0.4 dex, and this can explain the discrepant metallicity distributions between late-T dwarfs and Hypatia stars. Thus, we cannot say more about whether the metallicities of nearby late-T dwarfs and stars are similar. More comprehensive understanding of substellar metallicities would benefit from the continuing discoveries of brown dwarfs as companions to stars or members of nearby associations. These objects can provide independent metallicities from their hosts and are thus metallicity benchmarks for calibrating forward-modeling analyses and improving our understanding of ultracool atmospheres.

## 5.2. Age Distribution

We proceed to studying the ages of our late-T dwarfs. The age distribution of field brown dwarfs is essential to constraining their formation history and initial mass function (e.g., Kirkpatrick et al. 2012; Day-Jones et al. 2013). However, it is challenging to age-date individual field brown dwarfs, given that their ages and masses are degenerate and thus the former cannot be well constrained unless the latter are known independently. Previous work has estimated low-precision ages for large groups of ultracool dwarfs based on their kinematics. Such analysis is conducted in a statistical fashion and assumes the objects' space motions exhibit a larger spread with time due to dynamical evolution (e.g., Wielen 1977). Comparing the tangential or 3D space velocities of late-M, L, and early-T dwarfs to those of earlier-type main-sequence stars, several studies have found that local ultracool dwarfs have slightly smaller velocity dispersions and perhaps younger ages (0.5-4 Gyr; e.g., Dahn et al. 2002; Schmidt et al. 2007; Zapatero Osorio et al. 2007). However, based on the tangential velocities of a large, volume-limited sample of M7-T8 objects within 20 pc, Faherty et al. (2009) suggested the kinematic age of ultracool dwarfs (3-8 Gyr) is indistinguishable from that of earlier-type stars, although the former indeed becomes younger (2-4 Gyr) after excluding thick-disk or halo-like objects with

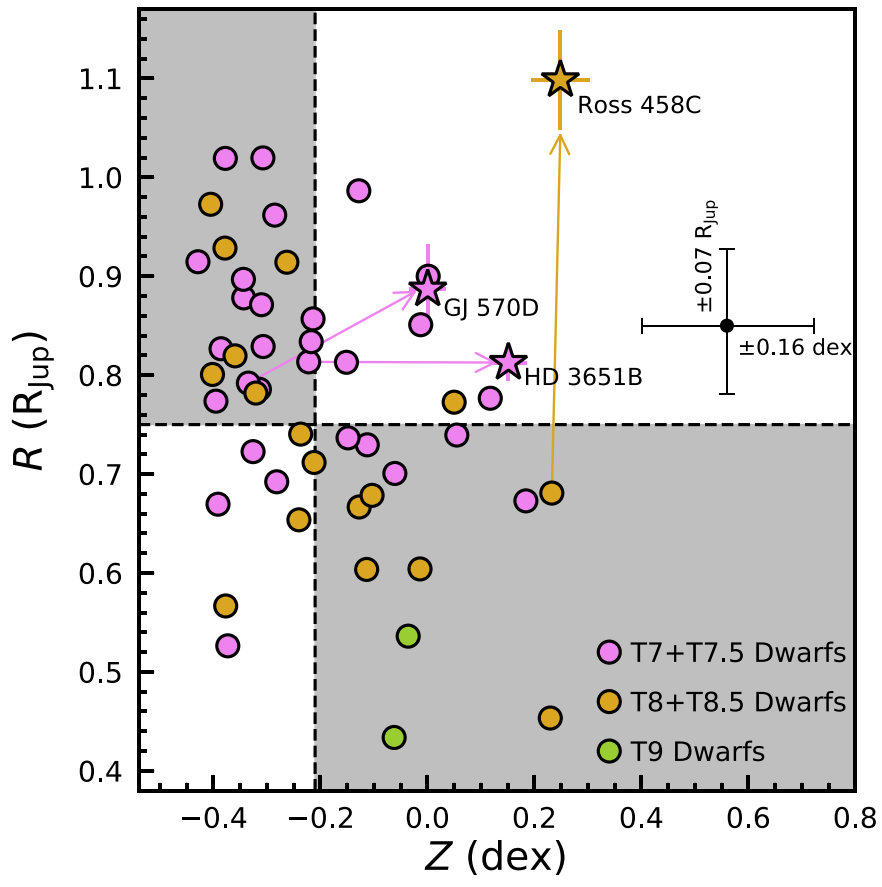


Figure 9. Our spectroscopically inferred R and Z for late-T dwarfs (binaries removed; violet for T7 and T7.5, orange for T8 and T8.5, and green for T9), with typical uncertainties shown as black error bars. We use two dashed lines for Z = -0.21 dex and R = 0.75  $R_{\rm Jup}$  to divide the space into four parts. Objects located in the upper left area (i.e., Z < -0.21 dex and  $R \ge 0.75$   $R_{\rm Jup}$ ) have metallicities that are  $>1\sigma$  lower than those of Hypatia stars but their radii appear reasonable. They might be in similar situations to GJ 570D and HD 3651B, whose fitted Z are underestimated by  $\approx 0.35$  dex but whose R are reliable, as noted in Paper I. Objects located in the lower right area (i.e.,  $Z \ge -0.21$  dex and R < 0.75  $R_{\rm Jup}$ ) have solar-like metallicities but unphysically small radii. Some of them might be in a similar situation to Ross 458C, whose fitted Z is reliable but whose R is underestimated by a factor of  $\approx 1.6$ . The evolutionary model parameters of the three benchmark companions (derived from Paper I) are shown as stars and connected to their spectroscopically inferred parameters by arrows.

high tangential velocities (>100 km s<sup>-1</sup>; also see Schmidt et al. 2007).

Thanks to long-term astrometric monitoring, many brown dwarf binaries now have measured dynamical masses. These mass benchmarks (e.g., Liu et al. 2008) can disentangle the age-mass degeneracy of substellar objects and thus yield some of the most robust ages. Recently, Dupuy & Liu (2017; DL17) studied the largest sample of such benchmark binaries to date (31 systems) and derived ages from their measured dynamical masses and the Saumon & Marley (2008) evolutionary models. They derived the substellar age distribution from a high-quality subset of 10 systems (M8-T5 within 30 pc) and found a median and mean of 1.3 Gyr and 2.3 Gyr, respectively. This distribution is systematically younger than those in past population synthesis analyses of Burgasser (2004) and Allen et al. (2005), who found that mid-L to early-T dwarfs have ages of  $\approx$ 2–3 Gyr (although the modeled age distribution at a given spectral type has a large spread; e.g., see Figure 8 of Burgasser 2004). The DL17 age distribution is in accord with Galactic dynamic heating preferentially scattering older substellar objects out of the immediate region (\$50 pc) around the Earth, which has been the main focus of brown dwarf searches.

Here we compare the DL17 age distribution to that of our late-T dwarf sample, for which we compute ages using the fitted  $\{T_{\text{eff}}, \log g, Z\}$  values at each step of the MCMC chains

and the interpolated cloudless Sonora–Bobcat evolutionary models (Table 5). Both our analysis and that of DL17 are subject to any systematics of the evolutionary models (e.g., Dupuy et al. 2009; Dupuy & Liu 2014; Beatty et al. 2018; Bowler et al. 2018; Dieterich et al. 2018; Brandt et al. 2020), but ours is also impacted by those of the atmospheric models, which are likely more uncertain. Therefore, our derived ages are expected to be less accurate than the DL17 results.

The age distribution of our late-T dwarfs is shown in Figure 10, with a median of 50 Myr and 16th to 84th percentiles spanning 10 Myr–0.4 Gyr. This distribution is significantly younger than those of DL17 (with a median of 1.3 Gyr and 16th to 84th percentiles spanning 0.8–3.0 Gyr) and past kinematic studies. Such a young distribution is implausible, especially since the majority of our sample are not associated with any stars or clusters with such young ages. <sup>18</sup> The same effect is seen for the three benchmarks, HD 3651B,

 $<sup>\</sup>overline{^{18}}$  Based on the available astrometry and radial velocities of 694 T and Y dwarfs, Zhang et al. (2021) recently identified a number of T dwarfs as candidate members of nearby young moving groups, with their final membership assessment awaiting radial velocity measurements. Only three objects in our sample here are candidate young moving group members: WISE J024124.73–365328.0 (T7, Argus, 40–50 Myr; Zuckerman 2019), 2MASS 1553+1532 (T7, Carina-Near, 200  $\pm$  50 Myr; Zuckerman et al. 2006), and WISEPC J225540.74–311841.8 (T8,  $\beta$  Pictoris, 24  $\pm$  3 Myr; Bell et al. 2015).

GJ 570D, and Ross 458C, whose primary stars have ages of 4.5–8.3 Gyr, 1.4–5.2 Gyr, and 0.15–0.8 Gyr determined by various age-dating techniques (as summarized in Paper I). In contrast, our spectroscopically inferred ages of these objects are much younger,  $0.038^{+0.077}_{-0.025}$  Gyr,  $0.031^{+0.052}_{-0.020}$  Gyr, and  $0.077^{+0.314}_{-0.056}$  Gyr, respectively (Figure 11 and Table 5).

Our implausibly young age estimates represent another illustration that the assumptions made within our model atmospheres should be further improved. To derive more reliable ages of late-T dwarfs from near-infrared spectra, we could introduce more atmospheric processes into the models, e.g., clouds and/or disequilibrium chemistry (see Section 6).

#### 5.3. Effective Temperature versus Spectral Type

Now we study the relation between the atmospheric-based, spectroscopically inferred  $T_{\rm eff}$  and the spectral types of late-T dwarfs. First, we briefly review empirical  $T_{\text{eff}}$ -SpT relations that have been established using evolutionary models. Similar to earlier work by Leggett et al. (2002), Golimowski et al. (2004) compiled the parallaxes and infrared spectrophotometry of 51 M1-T9 dwarfs. They measured bolometric luminosities from the objects' spectral energy distributions (SEDs) and then converted these into  $T_{\rm eff}$  assuming an age range of 0.1–10 Gyr and using evolutionary models (Burrows et al. 1997; Baraffe et al. 1998; Chabrier et al. 2000). Looper et al. (2008) and Stephens et al. (2009) later modified this sample by removing binaries and/or adding companions discovered since the Golimowski et al. (2004) work and obtained tighter temperature scales as a function of spectral type. Focusing on the coolest substellar objects, Dupuy & Kraus (2013) computed  $L_{\text{bol}}$  for 21 T8-Y0 field dwarfs using parallaxes, broadband photometry, and bolometric corrections, and then derived  $T_{\rm eff}$  using the Baraffe et al. (2003) evolutionary models with age assumptions of 1 Gyr and 5 Gyr. The most recent  $T_{\text{eff}}$ -SpT relation has been derived by Filippazzo et al. (2015) using a much larger sample of nearly 200 M6-T9 dwarfs. They measured  $L_{bol}$  based on a homogeneous SED analysis and then estimated  $T_{\rm eff}$  using the Saumon & Marley (2008) hybrid models with an assumed age of 0.5–10 Gyr for most objects and narrower ranges for association members and companions. The Filippazzo et al. (2015) temperature scale of field dwarfs is consistent with the results of Stephens et al. (2009) and Dupuy & Kraus (2013).

Figures 12 and 13 compare the atmospheric-based  $T_{\rm eff}$  of our T7–T9 dwarfs to the evolutionary-based temperature scales from Stephens et al. (2009), Dupuy & Kraus (2013), and Filippazzo et al. (2015). At a given spectral type, our spectroscopically inferred  $T_{\rm eff}$  show a spread of  $\pm 100$  K, similar to the empirical relations. Our results are consistent with the empirical ones for T7 and T7.5 dwarfs, but appear 50–200 K hotter at later types, likely because our derived  $T_{\rm eff}$  for T8–T9 dwarfs are less reliable than those for T7 dwarfs. As found in Paper I and summarized in Section 3.2 in this work, our spectral fits of Ross 458C (T8) predict  $\approx$ 120 K higher  $T_{\rm eff}$  than that of evolutionary model analysis, while the two T7.5 benchmarks (HD 3651B and GJ 570D) have no such significant discrepancy.

Figure 12 explores whether the derived  $T_{\rm eff}$ -SpT relation of our sample is gravity-dependent. We focus on the T7, T7.5, and T8 objects in our sample, since we have only four T8.5 and T9 dwarfs. Studying the objects'  $T_{\rm eff}$  as a function of logg, we find lower-gravity T7.5 and T8 dwarfs have on average hotter effective temperatures at a given spectral type. Intriguingly, this phenomenon is not found in earlier-T dwarfs. Based on a sample

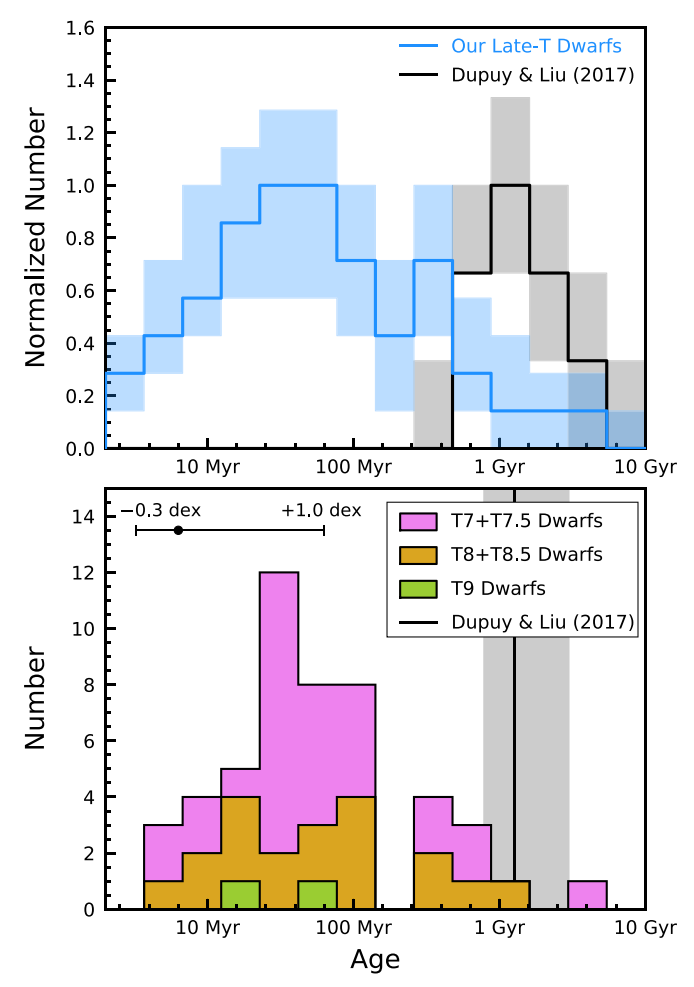


Figure 10. Top: Age distributions for our late-T dwarfs (binaries removed) and for benchmark binaries with dynamical masses from Dupuy & Liu (2017). We compute age posteriors for our late-T dwarfs using the spectroscopically inferred  $\{T_{\text{eff}}, \log g, Z\}$  values at each step of the MCMC chains and the interpolated Sonora-Bobcat evolutionary models. We then generate 10<sup>4</sup> distributions, each constructed by a random draw from each object's age posterior. We plot the median and the  $1\sigma$  confidence interval of these distributions using a blue line and shadow. The distributions for the Dupuy & Liu (2017) sample are produced in the same approach using the age posteriors of the mass benchmarks (T. Dupuy 2021, private communication). We normalize these two types of distributions so that their peaks correspond to one. Bottom: The distribution of our late-T dwarfs, with the violet color for T7 and T7.5, orange for T8 and T8.5, and green for T9. Our typical logarithmic age uncertainty is shown as a black error bar. We use a vertical black line and shadow to mark the median (1.3 Gyr) and the  $1\sigma$  spread (0.8–3.0 Gyr) of the Dupuy & Liu (2017) age distribution.

of 25 young ( $\leq$ 300 Myr) and old (>300 Myr) T0–T6 benchmarks, Zhang et al. (2020) demonstrated that lower-gravity objects tend to have  $\approx$ 100 K cooler  $T_{\rm eff}$  than their high-gravity counterparts at the same spectral types (also see Metchev & Hillenbrand 2006; Filippazzo et al. 2015; Faherty et al. 2016; Liu et al. 2016), which is the opposite of the  $T_{\rm eff}$ –logg relation for late-T dwarfs seen in Figure 12. For T7–T9 spectral types, there is only one low-gravity benchmark with direct spectroscopy, i.e., Ross 458C, for which our evolutionary model analysis derives  $T_{\rm eff} = 682^{+16}_{-17}$  K (Paper I). This temperature is consistent with those of higher-gravity field T8 dwarfs (678  $\pm$  113 K based on the  $T_{\rm eff}$ –SpT relation of Filippazzo et al. 2015) and thus not in accord with the  $T_{\rm eff}$ -logg relation from our results, which predicts its  $T_{\rm eff}$  to be much hotter. More discoveries of such

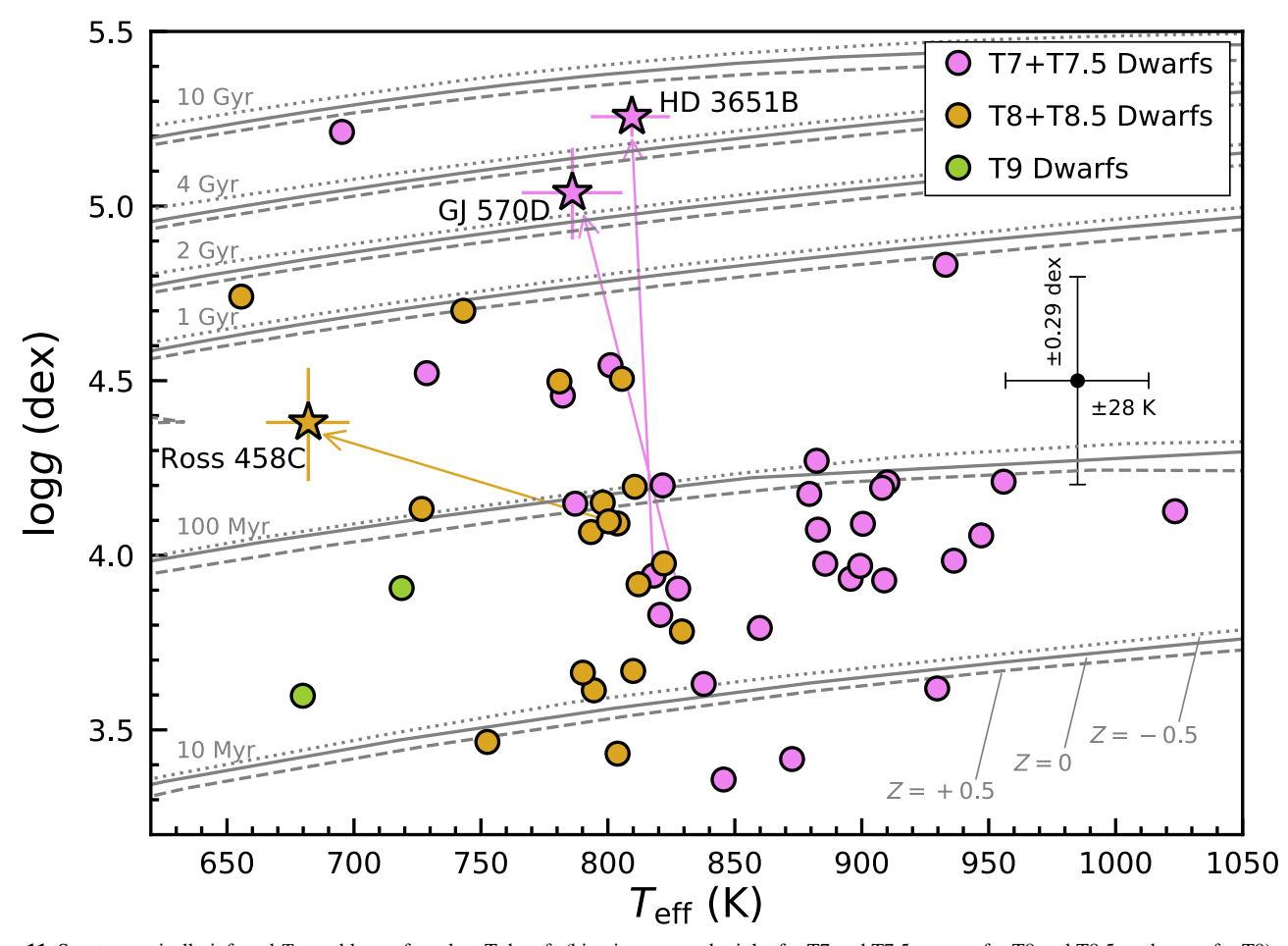


Figure 11. Spectroscopically inferred  $T_{\rm eff}$  and logg of our late-T dwarfs (binaries removed; violet for T7 and T7.5, orange for T8 and T8.5, and green for T9) and the cloudless Sonora–Bobcat isochrones (gray lines) with different ages (10 Myr, 100 Myr, 1 Gyr, 2 Gyr, 4 Gyr, and 10 Gyr) and metallicities (-0.5 dex, 0 dex, and +0.5 dex). The typical uncertainties for our fitted  $T_{\rm eff}$  and logg are shown as black error bars. The evolutionary model parameters of the three benchmark companions (derived from Paper I) are shown as stars and connected to their spectroscopically inferred parameters by arrows. Our forward-modeling analysis underestimates these benchmarks' logg and Z or overestimates their  $T_{\rm eff}$ , likely due to systematics of the cloudless Sonora–Bobcat models, and consequently, their ages derived from atmospheric model parameters are implausibly younger than the ages of their primary stars. Many of our late-T dwarfs might be in similar situations to these three companions, and thus their true ages should be systematically older.

young, late-type benchmarks will help us investigate the gravity dependence of late-T dwarfs' effective temperatures.

In fact, the possible relation between the fitted  $T_{\rm eff}$  and  $\log g$  of our sample is likely due to these parameters being overand/or underestimated. Some of the T7.5 dwarfs in our sample might be similar to HD 3651B and GJ 570D, whose fitted  $T_{\rm eff}$  are reliable but whose  $\log g$  are underestimated by  $\approx 1.2$  dex when compared to the more robust evolutionary model predictions. Also, some of the T8 dwarfs might be similar to Ross 458C, whose fitted  $\log g$  is reliable but whose  $T_{\rm eff}$  is overestimated by  $\approx 120$  K. Correcting their inaccurate atmospheric-based parameters would be the equivalent of shifting their  $\log g$  toward higher values and/or their  $T_{\rm eff}$  toward cooler values, which could alter the  $T_{\rm eff}$ -log relation in Figure 12.

Figure 13 explores whether the derived  $T_{\rm eff}$ -SpT relation of our sample is metallicity-dependent. Studying the objects'  $T_{\rm eff}$  as a function of Z, we find lower-metallicity T7, T7.5, and T8 dwarfs have on average cooler effective temperatures at a given spectral type. The validity of this metallicity dependence is uncertain. For the two late-T subdwarf benchmarks BD +01° 2920B (T8,  $Z=-0.38\pm0.06$  dex; Valenti & Fischer 2005) and Wolf 1130C (T8,  $Z=-0.70\pm0.12$ ; Mace et al. 2018), previous work has found their effective temperatures are similar to those

of the field population, which has on average higher metallicities (Pinfield et al. 2012; Mace et al. 2013b), and are thus not in accord with the  $T_{\rm eff}$ –Z relation seen in our results. Similar to the aforementioned  $T_{\rm eff}$ –logg trend, this  $T_{\rm eff}$ –Z relation for late-T dwarfs in Figure 13 might be related to modeling systematics. To further validate this potential metallicity dependence for late-T dwarfs, we need models with modified physical assumptions and more benchmarks over a wide range of metallicities.

#### 6. Discussion of the Cloudless Sonora-Bobcat Models

Our forward-modeling analysis shows the cloudless Sonora–Bobcat models match the general spectroscopic appearance of late-T dwarfs, but the fitted physical parameters can be under- or overestimated, suggesting the models' assumptions might be inadequate for fully interpreting late-T dwarf spectra (Section 5). Here we explore specific shortcomings, by focusing on 49 late-T dwarfs in our sample, as the other six objects are resolved or likely binaries (Section 4).

## 6.1. Starfish Covariance Hyperparameters

As discussed in Paper I, we can assess the systematic difference between data and models using the fitted

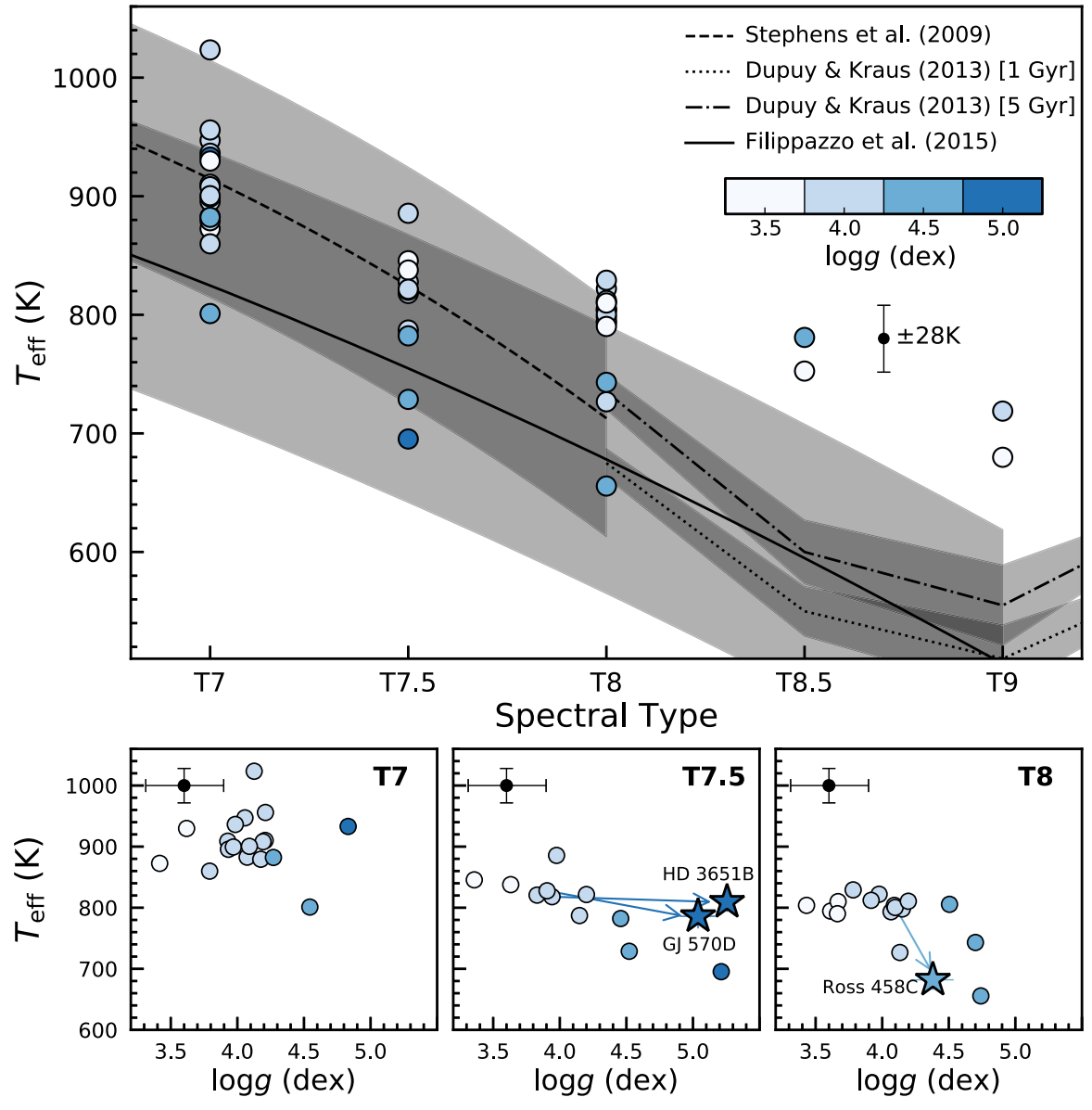


Figure 12. Top plot:  $T_{\rm eff}$ -SpT relation of our late-T dwarfs (binaries removed), with spectroscopically inferred logg encoded with blue shading. The median  $T_{\rm eff}$  uncertainty is shown as a black error bar. We overlay the evolutionary-based effective temperature scales from Stephens et al. (2009; dashed) and Filippazzo et al. (2015; solid). We also plot the Dupuy & Kraus (2013)  $T_{\rm eff}$ -SpT relations corresponding to assumed ages of 1 Gyr (dotted) and 5 Gyr (dashed–dotted). The gray shadow shows the rms of each empirical  $T_{\rm eff}$ -SpT relation. Bottom plots:  $T_{\rm eff}$  of our T7, T7.5, and T8 dwarfs as a function of logg. The median  $T_{\rm eff}$  and logg uncertainties are shown as black error bars. The evolutionary model parameters of the three benchmarks (derived from Paper I) are shown as stars and connected to their spectroscopically inferred parameters by arrows.

covariance hyperparameters  $\{a_N, a_G, \ell\}$  of our late-T dwarfs. The parameter  $\ell$  characterizes the autocorrelation wavelength of data—model residuals, caused by (1) an oversampled instrumental LSF and (2) the systematics of model assumptions. If the correlated residuals of an object are solely due to the instrumental LSF, then its fitted  $\ell$  should be within [820, 1840] km s<sup>-1</sup> and [425, 1115] km s<sup>-1</sup> for spectra taken by the SpeX 0."5 and 0."8 slits, respectively (see appendix of Paper I). However, the spectroscopically inferred  $\ell$  of almost all our late-T dwarfs are significantly higher than the range expected from the LSF, suggesting the correlated residuals of our sample do not arise from the instrument's spectral resolution but are rather shortcomings of the model

predictions (Figure 14). Figure 14 also shows the inferred  $\ell$  of our sample have no correlations with the objects' spectral types or fitted  $\{T_{\rm eff}, \log g, Z\}$ .

Given that the modeling systematics dominate the correlated residuals, we can use the other two hyperparameters  $(a_N$  and  $a_G)$  to quantify the modeling systematics. Specifically, we can compute  $\sqrt{a_G/a_N}$  and regard it as an equivalent flux that describes the average model uncertainties (as opposed to measurement uncertainties). Normalizing this value by the object's peak *J*-band flux (Equation (7) of Paper I), we define the normalized model uncertainty as  $\epsilon_J = \sqrt{a_G/a_N}/\max(f_{\rm obs},J)$ , with higher values suggesting more significant data—model discrepancies.

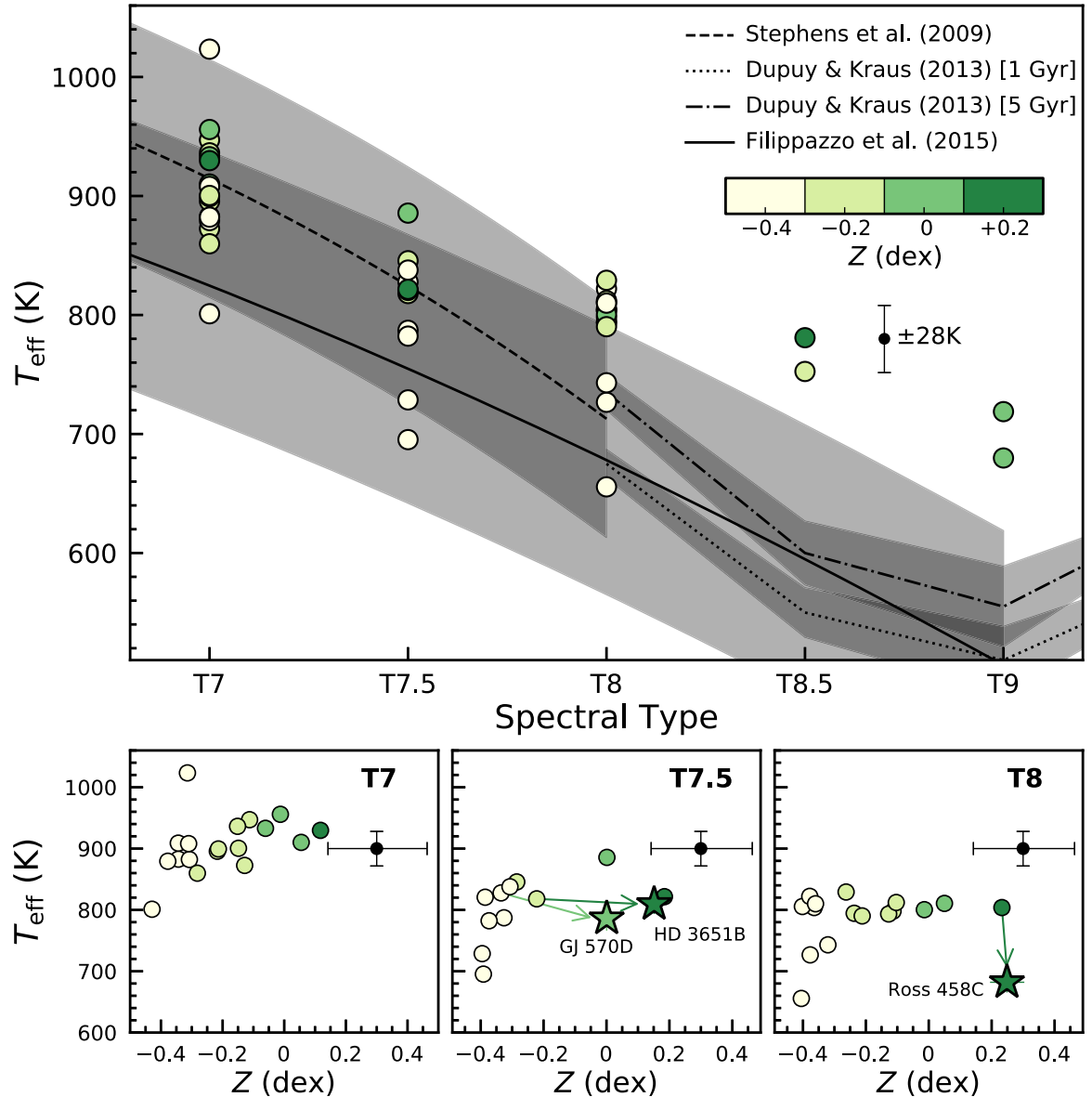


Figure 13. The effect of metallicity on the  $T_{\rm eff}$ -SpT relation of our late-T dwarfs (binaries removed), with the same format as Figure 11. The spectroscopically inferred Z are encoded with green shading. The bottom plots show the objects'  $T_{\rm eff}$  as a function of Z.

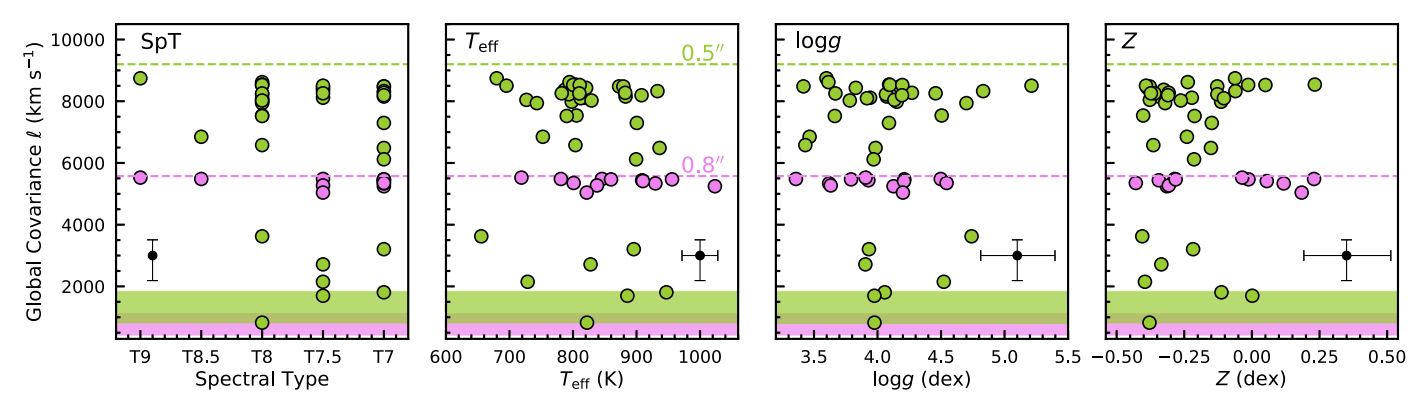


Figure 14. The covariance hyperparameter  $\ell$  of our 49 late-T dwarfs (binaries removed) as a function of spectral type and fitted  $\{T_{\rm eff}, \log g, Z\}$ , with the median uncertainties shown as black error bars. We use green and violet for  $\ell$  inferred from spectra taken from the 0... 5 and 0... 8 slits, respectively. For a given slit, we use a shaded area to mark the  $\ell$  range expected from the instrumental LSF (820–1840 km s<sup>-1</sup> for the 0... 5 slit and 425–1115 km s<sup>-1</sup> for the 0... 8 slit) and use dashed lines to mark the upper boundaries of our adopted  $\ell$  prior.

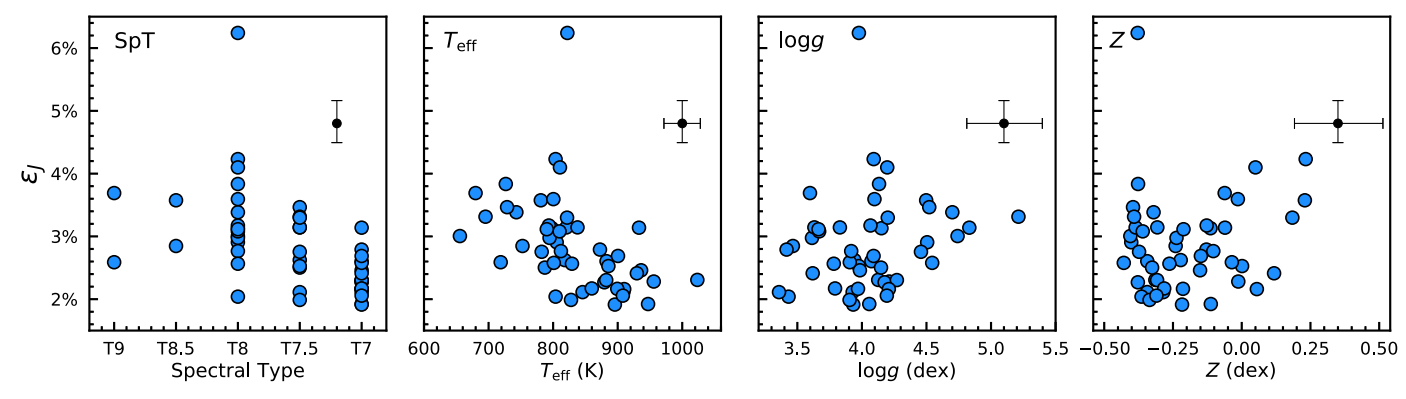


Figure 15. The  $\epsilon_J$  values of our 49 late-T dwarfs (binaries removed) computed from their covariance hyperparameters  $a_G$  and  $a_N$  and the observed spectra (Section 6.1). The  $\epsilon_J$  describes the fraction of model uncertainties (i.e., the systematic flux difference between the cloudless Sonora–Bobcat models and late-T dwarf spectra) relative to the objects' observed peak J-band fluxes. The median uncertainties are shown as black error bars. The object with the highest  $\epsilon_J$  among our sample is WISE 1322–2340. The  $\epsilon_J$  values, namely the model systematics, tend to become larger at later spectral types, cooler spectroscopically inferred  $T_{\rm eff}$ , and possibly higher logg and Z.

We summarize the derived  $\epsilon_J$  of our sample in Table 5 and find the systematic difference between the cloudless Sonora–Bobcat models and late-T dwarf spectra is on average  $\approx 2\%$ –4% of the observed peak *J*-band fluxes over 1.0– $2.5~\mu m$  wavelengths, <sup>19</sup> equivalent to an S/N (the ratio of the signal to the model uncertainty) of 50–25. This is in accord with our conclusion in Paper I based on the three late-T benchmarks, which are also included in the analysis here. This result implies that model uncertainties exceed measurement uncertainties when fitting the cloudless Sonora–Bobcat models to late-T dwarf spectra with S/N  $\gtrsim 50$  per pixel in the *J* band. As a consequence, increasing the S/N of observations does not necessarily improve the precision of the fitted physical parameters, as also seen in Figure 4 and discussed in Section 3.2.1.

Figure 15 plots our objects'  $\epsilon_J$  as a function of their spectral types and fitted physical parameters. We find the data–model difference tends to be larger toward later spectral types, cooler effective temperatures, and possibly higher logg and Z. These trends indicate some important atmospheric processes are likely missing in the model assumptions, which we discuss in the following section.

## 6.2. Spectral-fitting Residuals

Missing physical processes in the model assumptions should leave footprints in our objects' spectral-fitting residuals. Thanks to our large sample of late-T dwarfs, we can investigate these residuals and assess how models deviate from the observations as a function of wavelength and atmospheric parameters. In Figure 16, we normalize the fitting residuals for each object by its observed peak *J*-band flux and then stack them together. The resulting stack has a tight distribution as a function of wavelength and exhibits prominent features in the *YJHK* bands.

In order to study how the residuals are correlated with atmospheric properties, we plot the residuals sorted by the objects' spectral types and fitted  $\{T_{\rm eff}, \log g, Z\}$  in Figure 17. We further define the quantities  $q_Y$ ,  $q_J$ ,  $q_H$ , and  $q_K$  to evaluate the data–model difference in the YJHK bands for each object

(Table 5):

$$q(\lambda\lambda) = 1 - \frac{\int_{\lambda\lambda} f_{\text{model},\lambda} d\lambda}{\int_{\lambda\lambda} f_{\text{obs},\lambda} d\lambda}$$
such that  $q_Y \equiv q([1.00 \,\mu\text{m}, 1.10 \,\mu\text{m}])$   $q_J \equiv q([1.18 \,\mu\text{m}, 1.35 \,\mu\text{m}])$   $q_H \equiv q([1.50 \,\mu\text{m}, 1.65 \,\mu\text{m}])$   $q_K \equiv q([2.03 \,\mu\text{m}, 2.20 \,\mu\text{m}]).$  (2)

Here  $\lambda\lambda$  corresponds to the wavelength range of prominent *YJHK*-band features seen in Figure 16 and does not follow the standard definition of the filters. In addition,  $f_{\text{model},\lambda}$  and  $f_{\text{obs},\lambda}$  are the fitted model and the observed spectrum of the object, respectively. The sign of q indicates whether the models underpredict (positive) or overpredict (negative) the data, with larger absolute values of q indicating larger data-model discrepancies. By definition, model atmospheres that perfectly match the data will have q=0 for all wavelength ranges.

In the Y band ( $\approx 1.0-1.1~\mu m$ ), our fitted models slightly underpredict the spectra of most late-T dwarfs (Figures 16 and 17). This is likely related to the potassium resonance doublet at 0.77  $\mu m$  (Allard et al. 1999; Burrows et al. 2000), whose pressure-broadened wings can extend to the Y and J bands. The K line profile depends on the treatment of collisions between H<sub>2</sub> molecules and K atoms (e.g., Baudino et al. 2017; Phillips et al. 2020). The cloudless Sonora–Bobcat models adopt the K line shape theory by Allard et al. (2007). Allard et al. (2016) have improved calculations of the K–H<sub>2</sub> potential, which might predict more accurate shapes for the K I doublet and thereby the Y-band fluxes (e.g., Phillips et al. 2020).

In the J band ( $\approx 1.18-1.35~\mu m$ ), our fitted models overpredict the spectra of all late-T dwarfs, and we find  $q_J$  is correlated with spectral type and  $T_{\rm eff}$  (Figure 18), as the J-band residuals increase for later-type and cooler objects. This residual plausibly arises from clouds (e.g., Morley et al. 2012), given that fluxes at near-infrared spectral peaks are emitted from the deep atmosphere and are thus more sensitive to cloud opacity. Including clouds in the Sonora-Bobcat models might therefore produce spectra that better match the observations. Also, with lower effective temperatures, condensates of various species are expected to form (e.g., Na<sub>2</sub>S,

 $<sup>\</sup>overline{^{19}}$  We note these values describe an average systematic difference between the observed spectra and Sonora–Bobcat models over the 1.0–2.5  $\mu$ m range. As shown in Figure 16, such a systematic difference can be as large as 10%–20% of the objects' peak *J*-band fluxes over narrow wavelength ranges in the *J* and *H* bands.

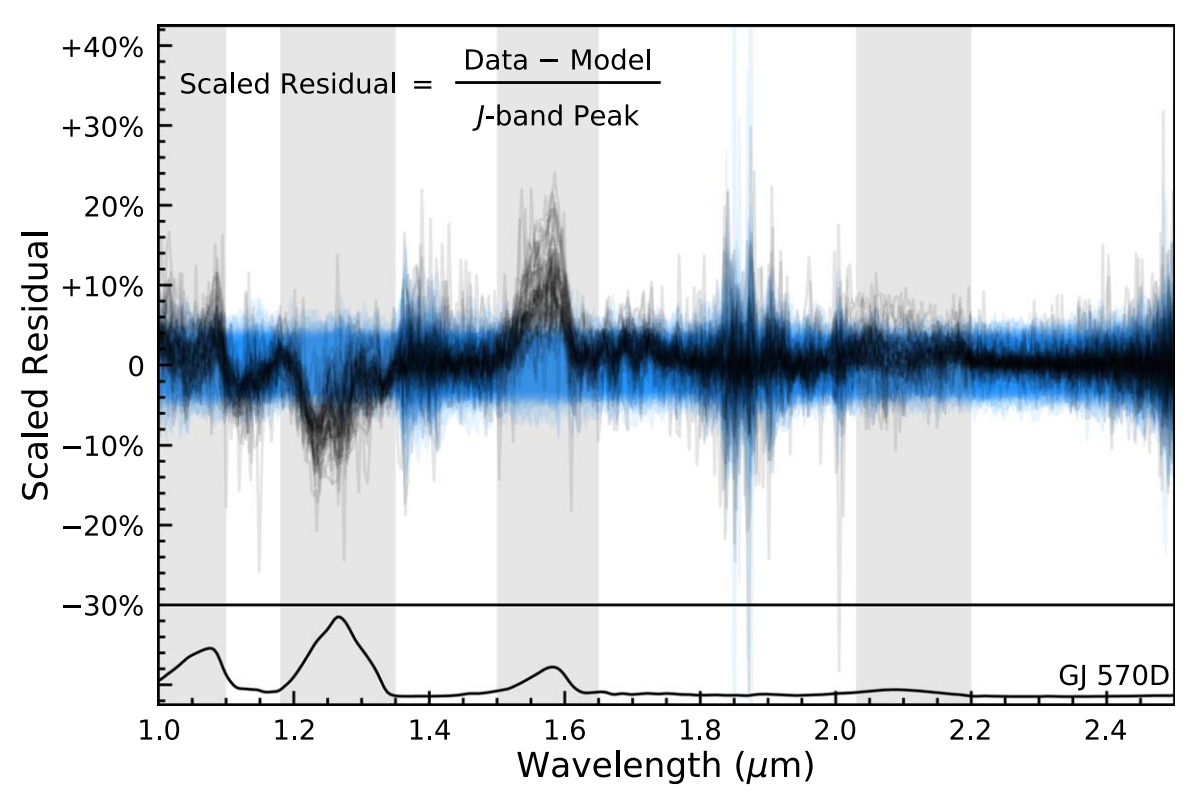


Figure 16. Stacked spectral-fitting residuals of our 49 late-T dwarfs (binaries removed), with each residual (i.e., data-model; black) normalized by the object's observed peak *J*-band flux. The  $1\sigma$  and  $2\sigma$  dispersions of  $5 \times 10^4$  draws from Starfish's full covariance matrix are shown as deep and light blue shadows, respectively, and they are normalized by the same peak flux for each object. The resulting stack has a tight distribution at each wavelength and exhibits prominent features in the *YJHK* bands (gray shadow, with the specific wavelength ranges shown in Equation (2)). The spectrum of GJ 570D is plotted at the bottom as a reference.

KCl, MnS, or ZnS; Lodders 1999; Morley et al. 2012), leading to a larger *J*-band discrepancy between data and the cloudless models. This is consistent with the  $q_{\mathcal{F}}T_{\text{eff}}$  correlation in Figure 18.

Alternatively, the overpredicted *J*-band flux of the cloudless Sonora-Bobcat models might be related to the assumption that the deep temperature gradient in convective regions lies along an adiabatic. As demonstrated by Tremblin et al. (2015, 2019), cloudless disequilibrium models with (1) atmospheric mixing (described by the eddy diffusion coefficients  $K_{zz}$ ) and (2) reduced vertical temperature gradients (as compared to the adiabatic lapse rate) are more appropriate for spectra of T/Y dwarfs than cloudless, chemical-equilibrium models. While these models can explain the *J*-band residuals of our sample, they will need to explain the  $q_J$ -SpT and  $q_J$ - $T_{\rm eff}$  correlations seen in Figure 18. One implication from these correlations is that the thermochemical instability in the Tremblin et al. (2015) models should be more significant with later spectral types and cooler Teff for late-T dwarfs. To examine this hypothesis, further investigation is needed to study such instability in brown dwarf atmospheres as a function of physical properties.

In the H band ( $\approx 1.50-1.65~\mu m$ ), our fitted models underpredict the spectra of all late-T dwarfs, and we find the residuals ( $q_H$ ) become more significant with later spectral types, cooler effective temperatures, and higher metallicities (Figure 18). These can be related to the disequilibrium abundance of NH<sub>3</sub>, which would be less than the amount assumed by the equilibrium chemistry within the cloudless Sonora–Bobcat models and would thus lead to weaker absorption in the blue wing of the H band (Saumon et al. 2006, 2012; Cushing et al. 2011; Zahnle & Marley 2014).

However, the NH<sub>3</sub> cross section is peaked around 1.5  $\mu$ m (wavenumbers of 6600–6700 cm<sup>-1</sup>; e.g., Yurchenko et al. 2011; Coles et al. 2019), slightly offset from the *H*-band residuals of our late-T dwarfs, which are peaked near 1.58  $\mu$ m. Alternatively, the underpredicted *H*-band spectra could well be a consequence of the spectral-fitting procedure responding to the overpredicted *J*-band flux by choosing models that underpredict the *H*-band flux. Studying our late-T dwarf spectra using (1) cloudless models with disequilibrium chemistry or (2) cloudy models with equilibrium chemistry will help better understand this *H*-band residual.

In the K band ( $\approx 2.03-2.20~\mu m$ ), our fitted models only slightly underpredict the spectra of most late-T dwarfs. Similar to the J-band residuals, such K-band residuals may arise from clouds and/or reductions in the vertical temperature gradient. As shown by Morley et al. (2012, their Figure 11) and Tremblin et al. (2015, their Figure 1), either of these two processes can reduce fluxes in the YJ bands and increase the flux in the K band.

## 7. Summary and Future Work

We have conducted a forward-modeling analysis for 55 late-T (T7–T9) dwarfs using low-resolution ( $R \approx 50$ –250) near-infrared (1.0–2.5  $\mu$ m) spectra and state-of-the-art, cloudless Sonora–Bobcat model atmospheres with  $T_{\rm eff} = 600$ –1200 K, log g = 3.25 - 5.5 dex, and  $Z = \{-0.5, 0, +0.5\}$  dex. Our sample contains 90% of the nearby T7–T9 population with distances  $\leq 25$  pc, J-band magnitudes  $\leq 17.5$  mag, and declinations from  $-40^{\circ}$  to  $+70^{\circ}$ . Our work is the largest analysis of brown dwarf spectra using multimetallicity models to date, as well as the most systematic test of any set of ultracool model

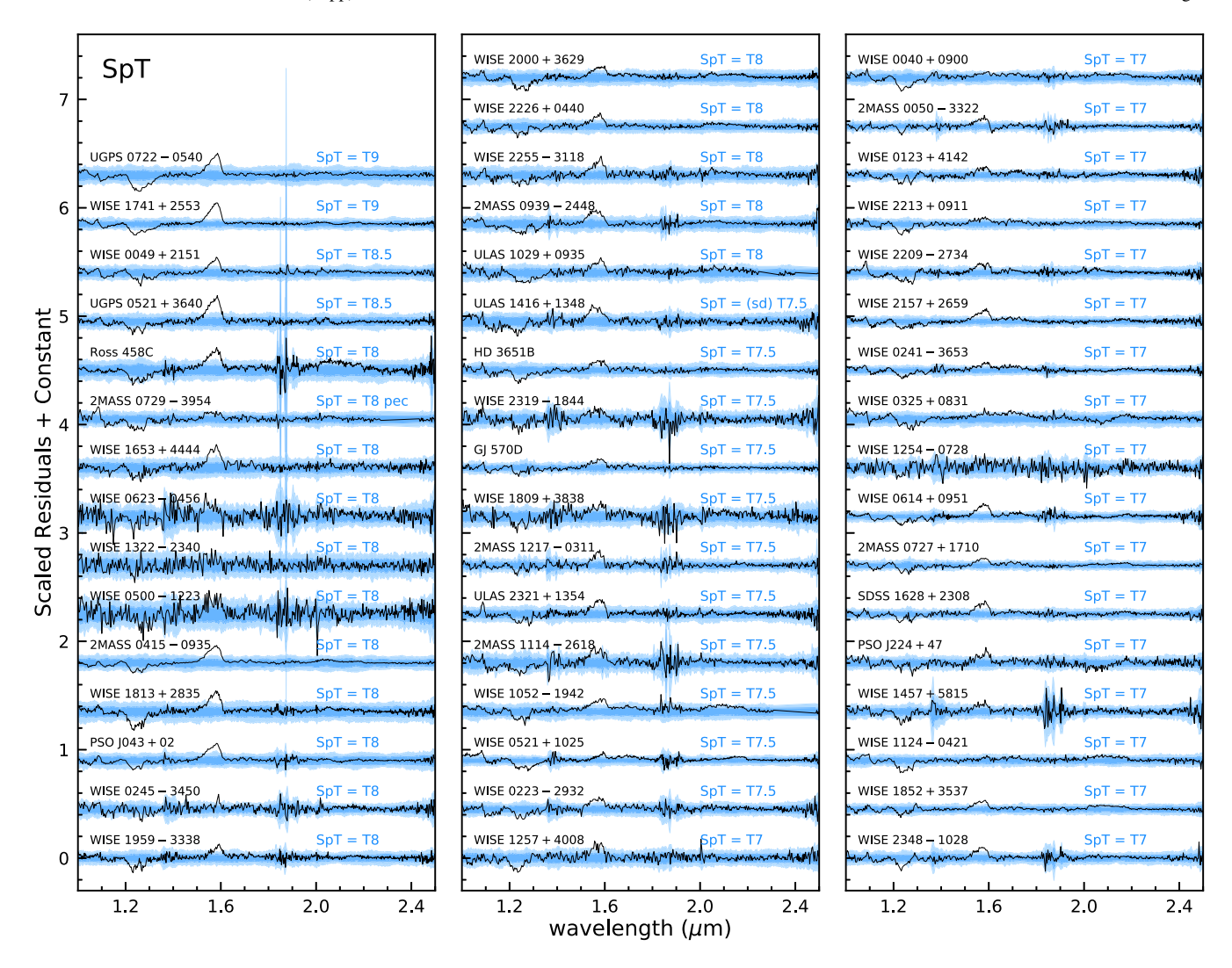


Figure 17. Residuals of our 49 late-T dwarfs (binaries removed) shown in order of spectral type and spectroscopically inferred  $T_{\rm eff}$ , logg, and Z. We use each object's observed peak J-band flux to normalize its residual (black), as well as the  $1\sigma$  and  $2\sigma$  dispersions of  $5\times10^4$  draws from Starfish's full covariance matrix (blue shadows). The J-band and H-band residuals tend to be more significant with later spectral types and cooler effective temperatures. The H-band residual also becomes more prominent with increasing metallicities.

atmospheres. Our forward-modeling framework was constructed and validated in Paper I, which uses the Bayesian inference tool Starfish (Czekala et al. 2015). Compared to traditional forward-modeling studies, our analysis produces more realistic error estimates since we account for uncertainties from model interpolation and correlated residuals due to instrumental effects and systematics of model assumptions.

We have inferred effective temperatures  $(T_{\rm eff})$ , surface gravities  $(\log g)$ , metallicities (Z), radii (R), masses (M), and bolometric luminosities  $(L_{\rm bol})$  for our late-T dwarfs, with the typical resulting  $\{T_{\rm eff}, \log g, Z\}$  uncertainties being approximately a third to a half of the Sonora–Bobcat model grid spacing. We have found no difference in the precision of these physical parameters for spectra with two different spectral resolutions  $(R \approx 80-250 \text{ and } 50-160)$ . Combining the resulting parameter posteriors of our entire sample, we have found some fitted parameters are correlated, including  $T_{\rm eff}$  and R, R and M, and  $\log g$  and R. Correlations within the first two pairs are expected by the Stefan–Boltzmann law and the calculation of mass from spectroscopic parameters, respectively. The third correlation illustrates that  $\log g$  and R are degenerate in the

cloudless Sonora–Bobcat models, and we provide a quantification of this  $\log g - Z$  dependence. For late-T dwarfs, the degeneracy acts such that an increase in Z, combined with a  $3.4 \times$  larger increase in  $\log g$ , results in a spectrum that has similar fitted atmospheric parameters. Consequently, using solar-metallicity model atmospheres to study late-T dwarfs whose metallicities are in fact nonsolar will bias the inferred  $\log g$ , but probably not other parameters.

By virtue of having a large sample of spectra within a focused spectral type range (as opposed to a smaller sample of objects over a wide spectral type range), we can study population properties of T7–T9 dwarfs to provide useful diagnostics about our set of grid models, which assume cloudless and chemical-equilibrium atmospheres:

1. The spectroscopically inferred metallicities of our entire sample and a volume-limited subset within 25 pc are 0.3–0.4 dex lower than those of nearby FGKM stars (e.g., Hinkel et al. 2014). This significant discrepancy is unlikely to be a real difference between the substellar and stellar populations, but rather due to our fitted metallicities being underestimated, which is also seen

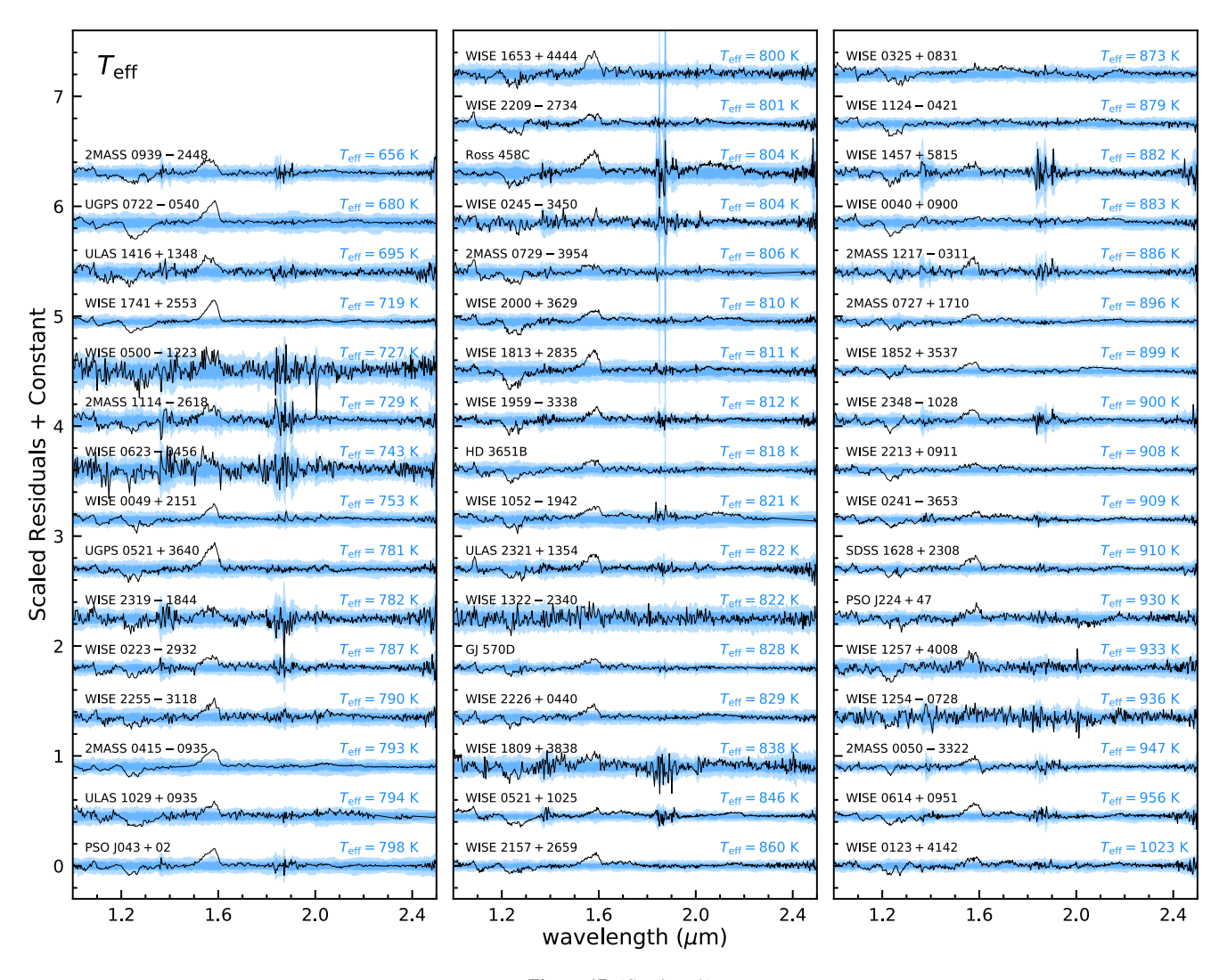


Figure 17. (Continued.)

from our Paper I analysis of the late-T benchmarks HD 3651B and GJ 570D.

- 2. The inferred ages of our sample, based on their fitted  $\{T_{\rm eff}, \log g, Z\}$  and evolutionary models, have a median of 50 Myr and a  $1\sigma$  confidence interval of 10 Myr–0.4 Gyr. These values are implausibly younger than the robustly determined ages of nearby M8–T5 binaries (Dupuy & Liu 2017) and thus are likely to be underestimated.
- 3. The spectroscopically inferred effective temperatures of our sample show a similar spread (±100 K) at a given spectral type as compared to empirical effective temperature scales, but our T<sub>eff</sub> appear systematically hotter (by 50–200 K) for ≥T8 dwarfs. Also, our derived T<sub>eff</sub>-SpT relation for late-T dwarfs is weakly correlated with the fitted logg and Z, as objects with either lower logg or higher Z have on average hotter T<sub>eff</sub> at a given spectral type. The possible gravity and metallicity dependence seen in this work might be caused by over- and/or underestimated physical parameters from spectral fitting, but it should be further validated using more late-T benchmarks with diverse ages and metallicities.

4. The spectroscopically inferred masses of our sample are unphysically small (mostly  $1-8~M_{\rm Jup}$ ), due to the underestimation of their fitted logg and/or R.

Using the hyperparameters from our spectral-fitting results, we have quantified that the systematic difference between the observed late-T dwarf spectra and the Sonora–Bobcat models is on average  $\approx 2\%$ –4% of the objects' peak *J*-band fluxes over the 1.0–2.5  $\mu$ m range (as high as 10%–20% of the objects' peak *J*-band fluxes over narrow wavelength ranges in the *J* and *H* bands), equivalent to an S/N of 50–25. Therefore, model uncertainties exceed measurement uncertainties when fitting the Sonora–Bobcat models to late-T dwarf spectra with S/N higher than these values. This can also explain why the fitted parameter precision of our sample does not improve with an increasing S/N once it is above  $\approx 50$  per pixel in the *J* band.

In order to investigate how to improve model assumptions, we have stacked the spectral-fitting residuals of our entire sample and investigated these as a function of wavelength and the inferred atmospheric properties. We have found common, prominent residual features in the *YJHK* bands:

1. In the *Y* band, the cloudless Sonora–Bobcat models tend to underpredict the observed fluxes, which is likely

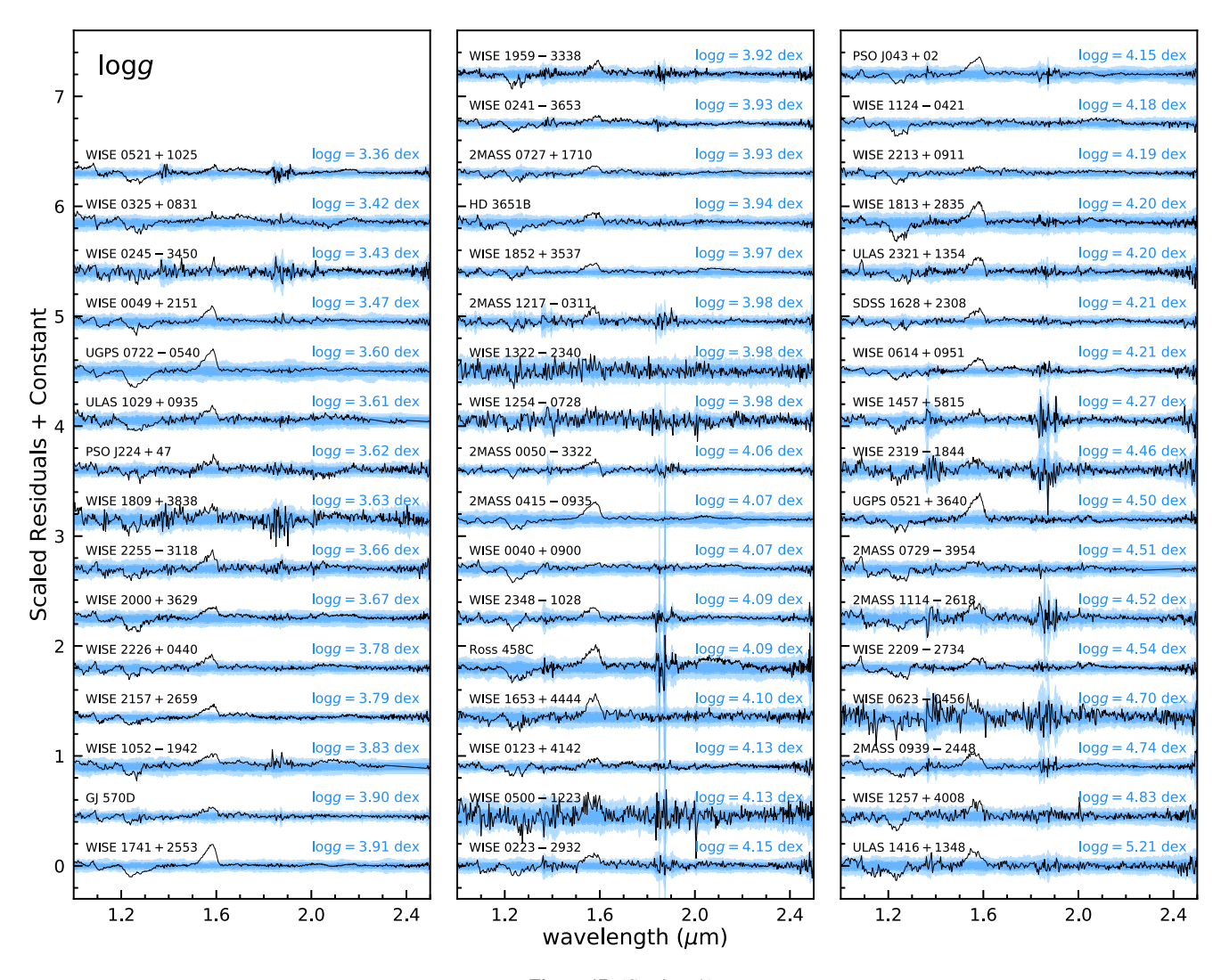


Figure 17. (Continued.)

related to the potassium line profiles. Further improvements of the alkali opacities might help reduce this residual (e.g., Allard et al. 2016).

- 2. In the J band, the cloudless Sonora–Bobcat models tend to overpredict the observed fluxes by an amount that is larger for later spectral types and cooler  $T_{\rm eff}$ . This effect is likely caused by missing opacity from clouds (e.g., Morley et al. 2012) or by the model assumption that the deep temperature gradient in convective regions lies along an adiabat (e.g., Tremblin et al. 2015). Including clouds or assuming a reduced temperature gradient could result in spectra that better match the observations.
- 3. In the *H* band, the cloudless Sonora–Bobcat models tend to underpredict the observed fluxes by an amount that is larger for later spectral types, cooler *T*<sub>eff</sub>, and higher *Z*. This residual might be explained by the disequilibrium abundance of NH<sub>3</sub> (e.g., Saumon et al. 2006; Cushing et al. 2011), which is not included by the Sonora–Bobcat assumption of equilibrium chemistry, although our residuals do not seem to precisely coincide with the expected wavelength for NH<sub>3</sub> opacities. Also, this *H*-band residual could merely be a consequence of the spectral-fitting procedure responding to the overpredicted *J*-band flux.

4. In the *K* band, the cloudless Sonora–Bobcat models tend to underpredict the observed fluxes, which likely arises from the same reason that causes the *J*-band residuals.

In future work, spectroscopic analysis of late-T dwarfs will benefit from models that include improved opacities, clouds, reduced vertical temperature gradients, and/or chemical disequilibrium. Such will also be essential to studying ultracool dwarfs with higher or lower effective temperatures than late-T dwarfs, for which there are already numerous spectra. The James Webb Space Telescope can further extend spectroscopic observations down to cooler temperatures and wider wavelength coverage. In addition, the analysis conducted in our work can be extended to other sets of grid models to verify whether the physical assumptions made by those models can reproduce the observations, and what atmospheric processes might be included to improve data-model consistency. Since brown dwarfs harbor atmospheric processes similar to those of imaged exoplanets, models employed to interpret both classes of objects are generated from the same theoretical framework. Dedicated analyses of brown dwarf atmospheres will therefore help us to robustly characterize direct spectroscopy of exoplanets and thereby understand their appearance, formation, and evolution.

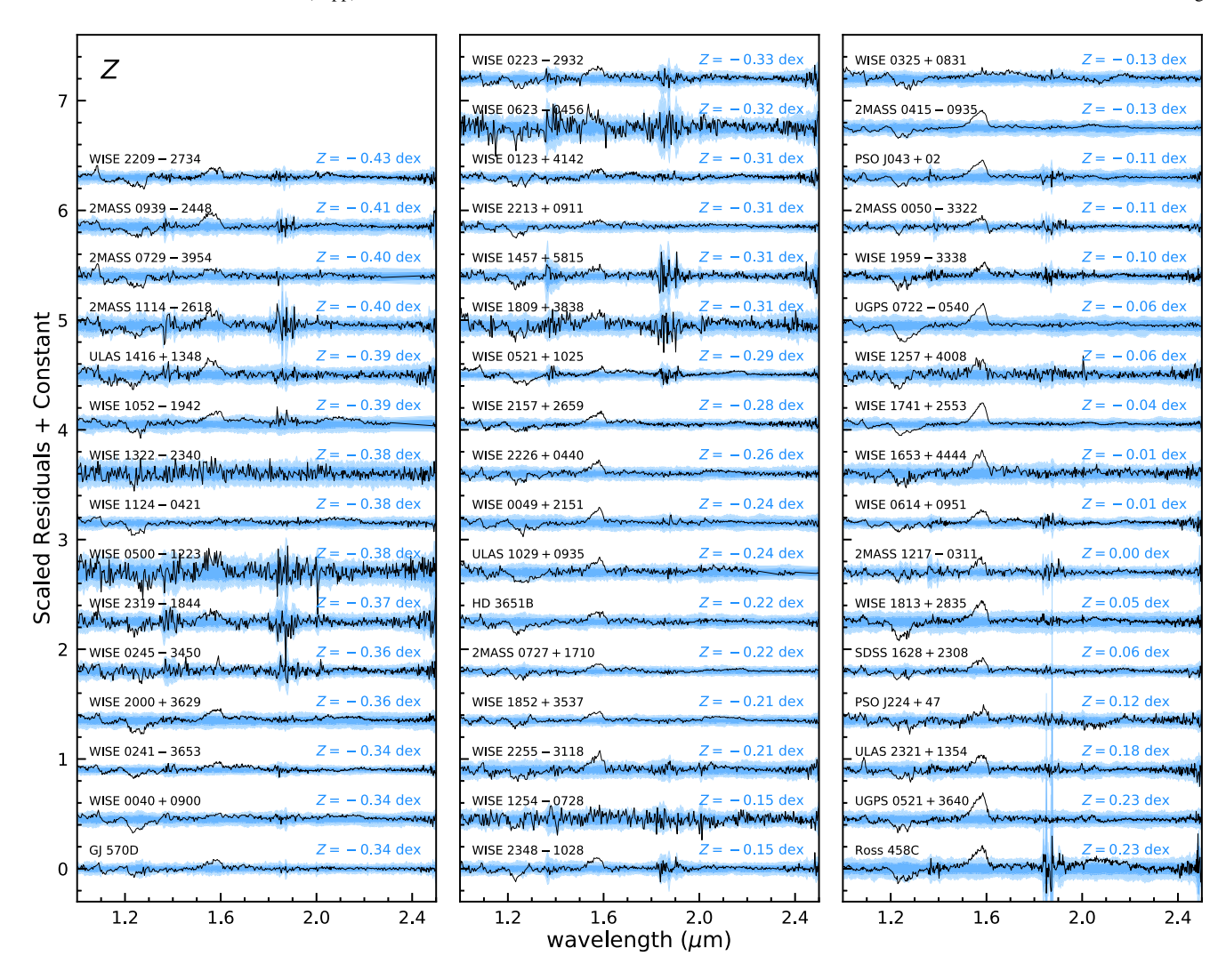


Figure 17. (Continued.)

We thank Mark Phillips, Didier Saumon, Caroline Morley, Eugene Magnier, Paul Mollière, Joe Zalesky, Trent Dupuy, and Ehsan Gharib-Nezhad for insightful discussions and comments on this work. We thank Ian Czekala, Michael Gully-Santiago, and Miles Lucas for helpful discussions about Starfish. We also thank Michael Gully-Santiago for implementing Starfish for the IRTF/SpeX prism data and sharing initial work on spectroscopic analysis for T dwarfs (https://github.com/gully/ jammer-Gl570D). We thank Trent Dupuy for providing age posteriors of brown dwarf binaries with dynamical mass measurements. This work has benefited from The Ultracool-Sheet at http://bit.ly/UltracoolSheet, maintained by Will Best, Trent Dupuy, Michael Liu, Rob Siverd, and Zhoujian Zhang, and developed from compilations by Dupuy & Liu (2012), Dupuy & Kraus (2013), Liu et al. (2016), and Best et al. (2018, 2021). This work benefited from the 2017 to 2019 Exoplanet Summer Program in the Other Worlds Laboratory at the University of California, Santa Cruz, a program funded by the Heising-Simons Foundation. M.C.L. acknowledges the National Science Foundation grant AST-1518339. This work is

funded in part by the Gordon and Betty Moore Foundation through the grant GBMF8550 to M.C.L. The advanced computing resources from the University of Hawaii Information Technology Services—Cyberinfrastructure are greatly acknowledged and Z.Z. thanks the technical support received from Curt Dodds. This research was greatly facilitated by the TOPCAT software written by Mark Taylor (http://www.starlink.ac.uk/topcat/). Finally, the authors wish to recognize and acknowledge the very significant cultural role and reverence that the summit of Maunakea has always had within the indigenous Hawaiian community. We are most fortunate to have the opportunity to conduct observations from this mountain.

Facility: IRTF (SpeX).

Software: Starfish (Czekala et al. 2015), emcee (Foreman-Mackey et al. 2013), Spextool (Cushing et al. 2004), TOPCAT (Taylor 2005), Astropy (Astropy Collaboration et al. 2013, 2018), IPython (Pérez & Granger 2007), NumPy (Oliphant 2006), SciPy (Jones et al. 2001), Matplotlib (Hunter 2007).

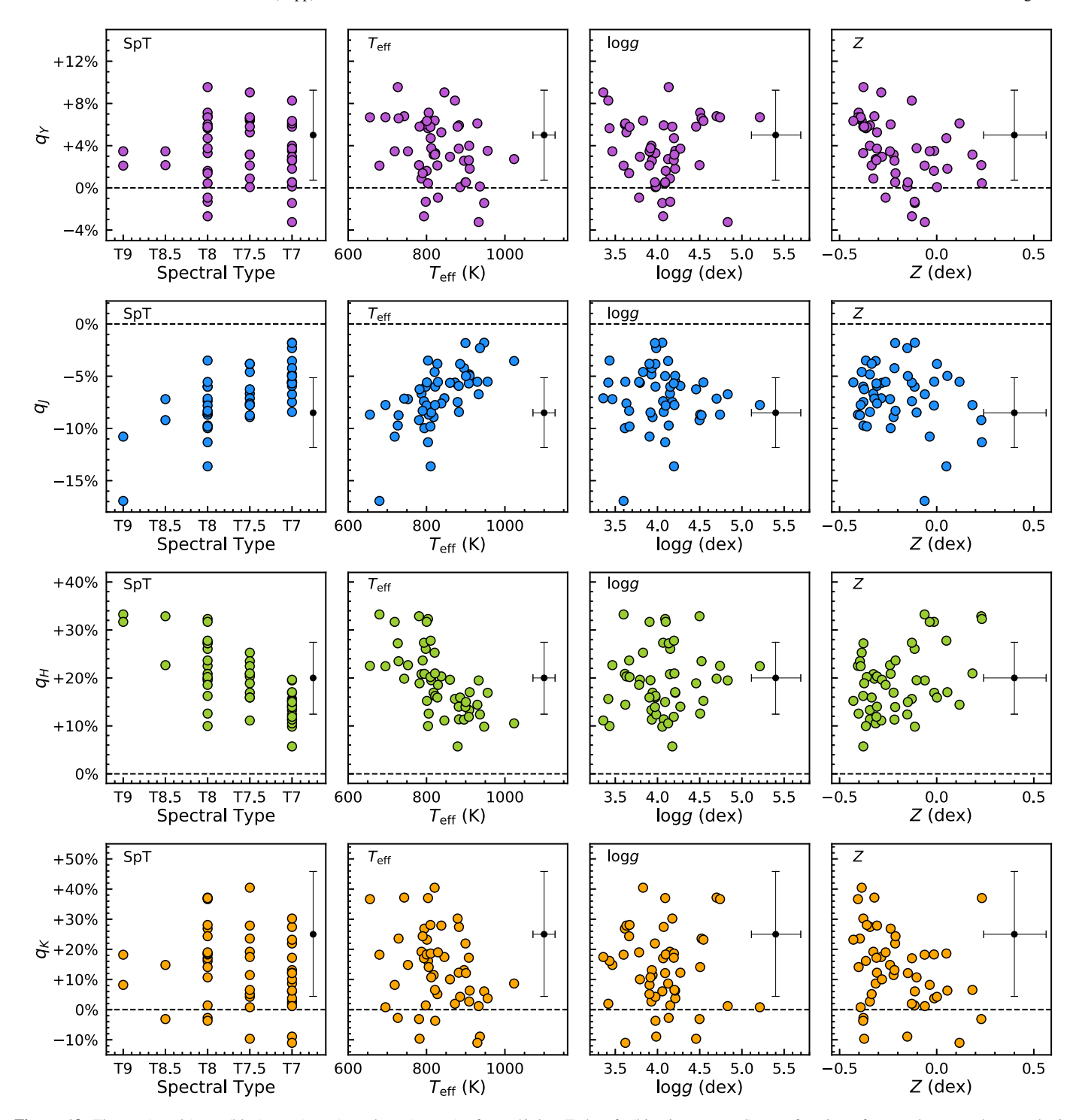


Figure 18. The  $q_Y$  (purple),  $q_I$  (blue),  $q_H$  (green), and  $q_K$  (orange) of our 49 late-T dwarfs (binaries removed) as a function of spectral type and atmospheric  $\{T_{\rm eff}, \log g, Z\}$ , with the median uncertainties shown by black error bars. The q values (Equation (2)) quantify the fitted residuals of the object in the YJHK bands. The sign of q indicates whether the models underpredict (positive) or overpredict (negative) the observed spectra over a given bandpass, with larger absolute values of q indicating larger data—model discrepancies. By definition, perfect models should have q=0 at all wavelengths (horizontal dashed lines).

## Appendix A Bolometric Luminosities: Comparison with Literature

Among our sample, 15 late-T dwarfs have bolometric luminosities in the literature. Filippazzo et al. (2015) constructed SEDs for 14 of our T7–T9 dwarfs by combining optical, near-infrared, and mid-infrared photometry and spectroscopy, and then computed bolometric luminosities by integrating their SEDs, with

short-wavelength fluxes linearly extrapolated to zero-wavelength and long-wavelength fluxes approximated by a Rayleigh–Jeans tail. Line et al. (2017) performed a retrieval analysis for SpeX prism spectra of 11 of our T7–T8 dwarfs and computed  $L_{\rm bol}$  by integrating the fitted models. Six objects in these two studies now have newer parallaxes with much higher precisions: HD 3651B, PSO J043.5395+02.3995, 2MASS J1217110–031113, Ross 458C, ULAS 1416+1348, and GJ 570D. We thereby scale

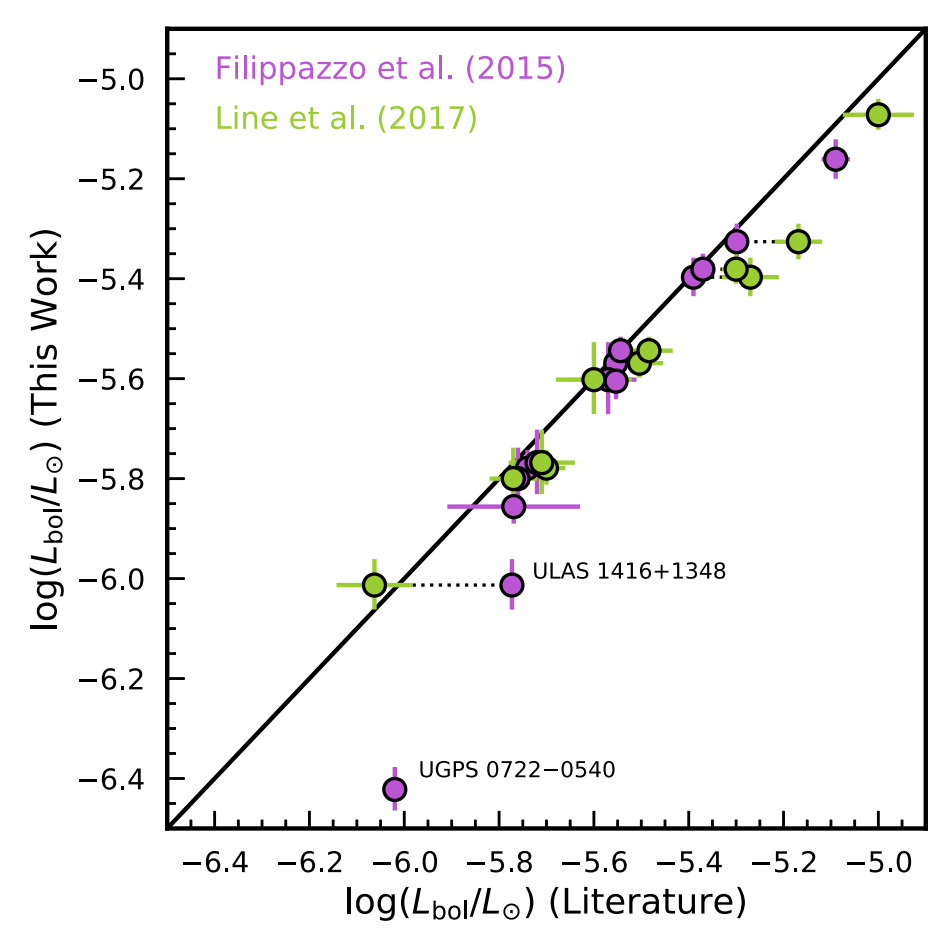


Figure 19. Comparison of bolometric luminosities for 15 late-T dwarfs with measurements both by us and by the literature (Appendix A). We use dotted lines to connect results for the same object. Our computed  $L_{\text{bol}}$  of these objects are generally consistent with the literature values but are systematically fainter by 0.06-0.07 dex.

these objects' literature  $L_{\rm bol}$  values with the new parallaxes, without modifying the published uncertainties.

Figure 19 and Table 7 compare our  $L_{\rm bol}$  values for these 15 late-T dwarfs with the literature values and suggest a general consistency. Our work produces slightly fainter  $L_{\rm bol}$ , with the differences having a weighted mean and weighted rms of  $0.057 \pm 0.099$  dex as compared to Filippazzo et al. (2015) and  $0.075 \pm 0.044$  dex as compared to Line et al. (2017). For UGPS J072227.51–054031.2 (UGPS 0722–0540), our estimated  $L_{\rm bol}$  is fainter than the value in Filippazzo et al. (2015) by  $8.4\sigma$ . As shown in Figure 2, our fitted cloudless models do not well match this object's observed spectrum and our

spectroscopically inferred  $T_{\rm eff}=680\pm26~{\rm K}$  is much higher than the values of 500–580 K suggested by Morley et al. (2012) and Tremblin et al. (2015), whose models account for sulfide clouds or diabatic convection (also see Section 6.2) and can better match this object's spectrum. Our overestimated  $T_{\rm eff}$  for UGPS 0722–0540 might lead to a lower ratio between the integrated fluxes in mid-infrared wavelengths (approximated by our fitted models) and in near-infrared wavelengths (indicated by our SpeX prism data), resulting in an underestimated  $L_{\rm bol}$ . For ULAS 1416+1348, our derived  $L_{\rm bol}=-6.013^{+0.052}_{-0.049}$  dex is  $4.7\sigma$  fainter than the value in Filippazzo et al. (2015), but is consistent with that in Line et al. (2017).

 Table 7

 Bolometric Luminosities from This Work, Filippazzo et al. (2015), and Line et al. (2017)

		This '	Work			Lite	rature Values <sup>a</sup>		
						Filippazzo e $\log(L_{ m b}$	et al. (2015) $_{ m ol}/L_{\odot}$ )	Line et al. (201	7) $\log(L_{\rm bol}/L_{\odot})$
Object	SpT	Parallax (mas)	$\log(L_{ m bol}/L_{\odot}) \ ({ m dex})$	Parallax (mas)	Par. Ref.	Original (dex)	Modified (dex)	Original (dex)	Modified (dex)
HD 3651B	T7.5	$89.79 \pm 0.06$	$-5.569^{+0.026}_{-0.029}$	$90.42 \pm 0.32$	2	$-5.56 \pm 0.01$	$-5.55 \pm 0.01$	$-5.51 \pm 0.05$	$-5.50 \pm 0.05$
2MASS J00501994-3322402	T7	$94.60 \pm 2.40$	$-5.397^{+0.039}_{-0.038}$	$94.60 \pm 2.40$	4	$-5.39\pm0.02$	$-5.39 \pm 0.02$	$-5.27 \pm 0.06$	$-5.27\pm0.06$
PSO J043.5395+02.3995	Т8	$146.10 \pm 1.50$	$-5.856^{+0.034}_{-0.034}$	$166.00 \pm 26.00$	6	$-5.88 \pm 0.14$	$-5.77 \pm 0.14$		
2MASSI J0415195-093506	Т8	$175.20 \pm 1.70$	$-5.779^{+0.036}_{-0.033}$	$175.20 \pm 1.70$	4	$-5.74 \pm 0.01$	$-5.74 \pm 0.01$	$-5.70 \pm 0.04$	$-5.70\pm0.04$
UGPS J072227.51-054031.2	Т9	$242.80 \pm 2.40$	$-6.422^{+0.045}_{-0.042}$	$242.80 \pm 2.40$	7	$-6.02 \pm 0.02$	$-6.02 \pm 0.02$		
2MASSI J0727182+171001	T7	$112.50 \pm 0.90$	$-5.381^{+0.031}_{-0.029}$	$112.50 \pm 0.90$	4	$-5.37 \pm 0.01$	$-5.37 \pm 0.01$	$-5.30 \pm 0.03$	$-5.30\pm0.03$
2MASS J07290002-3954043	T8 pec	$126.30 \pm 8.30$	$-5.602^{+0.075}_{-0.069}$	$126.30 \pm 8.30$	5	$-5.57 \pm 0.06$	$-5.57 \pm 0.06$	$-5.60 \pm 0.08$	$-5.60 \pm 0.08$
2MASS J09393548-2448279	Т8	$187.30 \pm 4.60$	$-5.768^{+0.066}_{-0.063}$	$187.30 \pm 4.60$	3	$-5.72\pm0.02$	$-5.72 \pm 0.02$	$-5.71 \pm 0.07$	$-5.71 \pm 0.07$
2MASS J11145133-2618235	T7.5	$179.20 \pm 1.40$	$-5.800^{+0.062}_{-0.049}$	$179.20 \pm 1.40$	4	$-5.76\pm0.01$	$-5.76 \pm 0.01$	$-5.77 \pm 0.05$	$-5.77\pm0.05$
2MASSI J1217110-031113	T7.5	$91.70 \pm 2.20$	$-5.326^{+0.036}_{-0.035}$	$90.80 \pm 2.20$	1	$-5.29 \pm 0.02$	$-5.30 \pm 0.02$	$-5.16 \pm 0.05$	$-5.17 \pm 0.05$
Ross 458C	Т8	$86.86 \pm 0.15$	$-5.605^{+0.032}_{-0.036}$	$85.54 \pm 1.53$	5	$-5.54 \pm 0.02$	$-5.55 \pm 0.02$	•••	
ULAS J141623.94+134836.3	(sd) T7.5	$107.56 \pm 0.30$	$-6.013^{+0.052}_{-0.049}$	$109.70 \pm 1.30$	4	$-5.79 \pm 0.01$	$-5.77 \pm 0.01$	$-6.08 \pm 0.08$	$-6.06\pm0.08$
GJ 570D	T7.5	$170.01 \pm 0.09$	$-5.544^{+0.028}_{-0.031}$	$171.22 \pm 0.94$	2	$-5.55 \pm 0.01$	$-5.54 \pm 0.01$	$-5.49 \pm 0.05$	$-5.48\pm0.05$
SDSS J150411.63+102718.4	T7	$46.10 \pm 1.50$	$-5.161^{+0.040}_{-0.039}$	$46.10 \pm 1.50$	4	$-5.09 \pm 0.03$	$-5.09 \pm 0.03$		
2MASSI J1553022+153236	T7	$75.10 \pm 0.90$	$-5.072^{+0.032}_{-0.030}$	$75.10 \pm 0.90$	4	•••	•••	$-5.00 \pm 0.08$	$-5.00 \pm 0.08$

#### Notes.

<sup>&</sup>lt;sup>a</sup> We compute the modified bolometric luminosities by scaling the original literature *L*<sub>bol</sub> to the more precise parallaxes adopted in this work without modifying the uncertainties provided by the literature. **References.** (1) Tinney et al. (2003), (2) van Leeuwen (2007), (3) Burgasser et al. (2008b), (4) Dupuy & Liu (2012), (5) Faherty et al. (2012), (6) Kirkpatrick et al. (2012), and (7) Leggett et al. (2012).

#### Appendix B Bolometric Corrections

Table 8 presents our bolometric corrections for late-T dwarfs in the  $J_{\rm MKO}$ ,  $H_{\rm MKO}$ , and  $K_{\rm MKO}$  bands computed using their bolometric fluxes (with  $M_{\rm bol,\odot} = +4.74$ ). For this calculation, we exclude six objects that are resolved or candidate binaries, as well as two objects with peculiar spectra (2MASS J0939

-2448 and ULAS J1416+1348; see Section 4). Comparison with the bolometric corrections of Liu et al. (2010) demonstrates a  $1\sigma$  consistency. Filippazzo et al. (2015) provided bolometric corrections using 2MASS bands, so we cannot compare directly to their results. Following Dupuy & Liu (2012), we also compute an estimate of the intrinsic (astrophysical) scatter in the bolometric correction at a given spectral type and band.

 Table 8

 Bolometric Corrections for T7–T9 Dwarfs

			BC.	$J_{ m MKO}$			$BC_I$	$H_{MKO}$			BC	K <sub>MKO</sub>	
Spectral Type	$N_{ m obj}$	Mean (mag)	Error (mag)	$\sigma_{ m add}$ (mag)	Rms (mag)	Mean (mag)	Error (mag)	$\sigma_{ m add}$ (mag)	Rms (mag)	Mean (mag)	Error (mag)	$\sigma_{ m add}$ (mag)	Rms (mag)
[T7, T7.5)	18	2.67	0.02	0.09	0.10	2.32	0.02	0.00	0.07	2.35	0.02	0.17	0.17
[T7.5, T8)	10	2.58	0.03	0.07	0.10	2.21	0.03	0.00	0.06	2.17	0.03	0.32	0.26
[T8, T8.5)	14	2.57	0.03	0.15	0.16	2.20	0.03	0.00	0.08	2.21	0.03	0.29	0.29
[T8.5, T9)	3	2.59	0.07	0.23	0.18	2.16	0.05	0.20	0.15	2.17	0.09	0.20	0.18
[T9, T9.5)	2	2.29	0.07	0.02	0.05	2.04	0.08	0.11	0.07	1.69	0.11	0.37	0.17

Notes. For each spectral type bin and photometric band, we tabulate the weighted average, weighted error, and weighted rms of the bolometric corrections, by excluding resolved or candidate binaries and two objects with peculiar spectra (Appendix B). The  $\sigma_{add}$  column gives the additional uncertainty needed to make the reduced  $\chi^2 \approx 1$  for the weighted average, as an estimate of intrinsic (astrophysical) variations. When using these bolometric corrections, we recommend adopting the larger of the weighted error and  $\sigma_{add}$  for the uncertainty on the correction.

## Appendix C Forward-modeling Analysis with the Traditional Approach

We also conduct forward-modeling analysis for our late-T dwarfs following the traditional approach described in Paper I. We use the cloudless Sonora–Bobcat model atmospheres over their entire parameter space of [200, 2400] K in  $T_{\rm eff}$ , [3.25, 5.5] dex in logg, and [-0.5, +0.5] dex in Z, and use linear interpolation to synthesize model spectra with an arbitrary set of grid parameters. We determine six physical parameters { $T_{\rm eff}$ ,  $\log g$ , Z,  $v_{\rm r}$ ,  $v \sin i$ ,  $\log \Omega$ } with the same priors as those of our Starfish-based analysis (Section 3.1), and construct our covariance matrix by simply placing squared flux uncertainties of spectra along its diagonal axis.

We use *emcee* to fit our 1.0– $2.5~\mu m$  spectra with 24 walkers and terminate the fitting process with  $3\times 10^4$  iterations given that such a number of iterations exceeds 50 times the autocorrelation length of all the fitted parameters. We incorporate a systematic error of  $180~km~s^{-1}$  into the inferred radial velocity to account for the uncertainty in the wavelength calibration of the SpeX prism data (Section 3.1). We also incorporate a systematic error of  $0.4\sigma_{H_{\rm MKO}}$  into the inferred  $\log\Omega$  to account for the uncertainty in flux calibration (Section 3.1), where  $\sigma_{H_{\rm MKO}}$  is the photometric error in the object's H-band magnitude. We compute the objects' radii (R) and masses (M) using their parallaxes and  $\log g$  and  $\log \Omega$  posteriors and also compute ages by interpolating the Sonora–Bobcat evolutionary models using the fitted { $T_{\rm eff}$ ,  $\log g$ , Z}. We summarize all inferred parameters and their uncertainties in Table 9.

Figure 20 compares the parameter posteriors and the fitted model spectra (interpolated at parameters drawn from the MCMC samples) derived from the traditional approach to those from the Starfish analysis. While the fitted model spectra by these two methods both match the data, the residuals from the traditional approach significantly exceed measurement uncertainties in some wavelength ranges, indicating that the more sophisticated Starfish covariance matrix better describes the difference between the data and models (also see Figure 5 of Czekala et al. 2015). Also, the fitted models from the two methods are not always identical at several wavelengths, primarily because of their vastly different covariance matrices, which weight residuals and compute likelihoods differently given the same set of physical parameters.

Figure 21 compares eight physical parameters  $\{T_{\rm eff}, \log g, Z, v_{\rm r}, v \sin i, \log \Omega, R, M\}$  of late-T dwarfs inferred from the

two approaches. The weighted mean and weighted rms of the Starfish—traditional parameter differences are  $-16\pm23~\rm K$  for  $T_{\rm eff}, -0.09\pm0.23$  dex for  $\log g, -0.09\pm0.10$  dex for  $Z, 45\pm125~\rm km~s^{-1}$  for  $v_{\rm r}, -1\pm6~\rm km~s^{-1}$  for  $v\sin i, 0.040\pm0.061$  dex for  $\log\Omega, 0.03\pm0.06$  dex for R, and  $-0.17\pm1.14$  dex for M. Therefore, the results from these two spectral-fitting methods are generally consistent. Several objects have significantly different properties based on the two methods: WISE 2209–2734, ULAS 1416+1348, WISE 0500–1223, 2MASS 0939–2448, and WISE 0458+6434.

For WISE 2209–2734, the Starfish analysis derives  $\log g$  and Z that are smaller than those of the traditional method by  $0.95 \pm 0.34$  dex and  $0.33 \pm 0.10$  dex, respectively. However, the fitted model spectra from the two methods are similar, given that these parameter offsets follow the  $\log g - Z$  degeneracy of the cloudless Sonora–Bobcat models that we find based on the stacked posteriors of our late-T dwarf sample (Section 3.2.2). The different results from the two methods are thus likely caused by the different covariance matrices used to compute the likelihood.

ULAS 1416+1348 is a wide-orbit companion to a low-metallicity late-L dwarf (see Section 4.2). Its  $\{T_{\rm eff}, \log g, \log \Omega, R, M\}$  are different between the two methods by  $1\sigma$ -6 $\sigma$ , but we find the fitted model spectra from Starfish better match the data especially for the blue wing of the Y band (Figure 20).

Among the remaining three objects, WISE 0458+6434 is a resolved 0."51 T8.5+T9 binary (Section 4.1). Binarity can result in spectral peculiarity and cause the two forward-modeling approaches to derive different parameters. The binarity of WISE 0500–1223 and 2MASS 0939–2448 is uncertain (Section 4.2). In addition, the parameter posteriors of WISE 0500–1223 inferred from the traditional method show two peaks, with one peak consistent with the Starfish results. This anomaly might also be related to the low S/N of the data ( $\approx$ 13 in the *J* band).

Table 6 compares the typical parameter uncertainties between the two methods. The traditional forward-modeling approach produces artificially small parameter errors by factors of 2–15 in  $\{T_{\rm eff}, \log g, Z, \log \Omega, R, M\}$  and factors of 1–2 in  $v_{\rm r}$  and  $v \sin i$  (also see Figure 4). We note that the larger error estimates from Starfish are more realistic, given that Starfish accounts for uncertainties from model interpolation and correlated residuals.

Table 9 Traditional Forward-modeling Analysis: Fitted and Derived Properties of T7-T9 Dwarfs

				F	itted Parameters <sup>a</sup>			I	Derived Parameters <sup>b</sup>	
Object	Slit (")	T <sub>eff</sub> (K)	logg (dex)	Z (dex)	$(\text{km s}^{-1})$	vsini (km s <sup>-1</sup> )	$\log\Omega$ (dex)	$R \over (R_{\rm Jup})$	$M \ (M_{ m Jup})$	Age (Myr)
HD 3651B	0.5	$824^{+2}_{-3}$	$4.00^{+0.01}_{-0.12}$	$-0.14^{+0.02}_{-0.02}$	$-252^{+188}_{-197} \stackrel{(23)}{_{(29)}}$	28+17	$-19.572^{+0.021}_{-0.018} {\scriptstyle{(0.006)}\atop{(0.005)}}$	$0.79^{+0.02}_{-0.02}$	$2.47^{+0.16}_{-0.54}$	47 <sup>+1</sup> <sub>-17</sub>
WISE 0040+0900	0.5	$926^{+1}_{-1}$	$3.87^{+0.00}_{-0.00}$	$-0.23^{+0.01}_{-0.01}$	$-291^{+188}_{-202}{}^{(20)}_{(24)}$	$23^{+18}_{-14}$	$-19.762^{+0.010}_{-0.009} \stackrel{(0.002)}{(0.001)}$	$0.80^{+0.04}_{-0.03}$	$1.90^{+0.20}_{-0.15}$	$20^{+0}_{-0}$
WISE 0049+2151	0.5	$768^{+2}_{-2}$	$3.67^{+0.02}_{-0.02}$	$-0.13^{+0.01}_{-0.01}$	$-345^{+193}_{-184}$ (19)	$18^{+12}_{-12}$	$-19.401^{+0.010}_{-0.009} \stackrel{(0.005)}{_{(0.004)}}$	$0.62^{+0.01}_{-0.01}$	$0.71^{+0.04}_{-0.04}$	$16^{+1}_{-1}$
	0.8	$760^{+2}_{-2}$	$3.75^{+0.04}_{-0.03}$	$-0.02^{+0.02}_{-0.02}$	$-157^{+181}_{-181} \stackrel{(29)}{_{(29)}}$	$19^{+13}_{-13}$	$-19.402^{+0.011}_{-0.011} \stackrel{(0.007)}{_{(0.007)}}$	$0.61^{+0.01}_{-0.01}$	$0.86^{+0.09}_{-0.07}$	$23^{+4}_{-2}$
2MASS 0050-3322	0.5	$950^{+1}_{-1}$	$4.23^{+0.01}_{-0.02}$	$-0.02^{+0.01}_{-0.01}$	$-615^{+180}_{-180}_{(19)}^{(18)}$	$35^{+25}_{-24}$	$-19.600^{+0.040}_{-0.040}^{+0.040}_{(0.003)}^{+0.040}$	$0.72^{+0.04}_{-0.04}$	$3.56^{+0.42}_{-0.37}$	$79^{+5}_{-6}$
WISE 0123+4142	0.8	$1025^{+1}_{-1}$	$3.93^{+0.01}_{-0.01}$	$-0.35^{+0.01}_{-0.01}$	$-97^{+182}_{-181}{}^{(27)}_{(25)}$	$28^{+17}_{-19}$	$-20.281^{+0.024}_{-0.024} \stackrel{(0.003)}{_{(0.002)}}$	$0.79^{+0.06}_{-0.05}$	$2.20_{-0.28}^{+0.37}$	$19^{+1}_{-0}$
VISE 0223-2932	0.5	$820^{+2}_{-3}$	$4.12^{+0.02}_{-0.02}$	$-0.28^{+0.02}_{-0.01}$	$-476^{+200}_{-187}^{(35)}_{(32)}$	$31^{+19}_{-21}$	$-19.833^{+0.049}_{-0.045} \stackrel{(0.006)}{_{(0.006)}}$	$0.65^{+0.04}_{-0.04}$	$2.25^{+0.35}_{-0.27}$	$73^{+7}_{-5}$
WISE 0241-3653	0.8	$914^{+1}_{-1}$	$3.94^{+0.00}_{-0.00}$	$-0.37^{+0.01}_{-0.01}$	$-204^{+181}_{-181} \stackrel{(25)}{_{(25)}}$	$29^{+19}_{-20}$	$-19.941^{+0.028}_{-0.028} \stackrel{(0.002)}{_{(0.002)}}$	$0.88^{+0.06}_{-0.05}$	$2.71^{+0.36}_{-0.31}$	$27^{+1}_{-0}$
WISE 0245-3450	0.5	$813^{+10}_{-8}$	$3.78^{+0.04}_{-0.17}$	$-0.17^{+0.03}_{-0.04}$	$-129^{+190}_{-190}^{(64)}_{(64)}$	$146^{+103}_{-100}$	$-20.117^{+0.045}_{-0.045} \stackrel{(0.021)}{_{(0.025)}}$			$21^{+4}_{-9}$
PSO J043+02	0.5	$815^{+1}_{-2}$	$4.34^{+0.02}_{-0.01}$	$-0.02^{+0.01}_{-0.01}$	$-64^{+180}_{-180}_{(18)}^{(15)}$	$32^{+27}_{-20}$	$-19.438^{+0.011}_{-0.009} \stackrel{(0.004)}{_{(0.004)}}$	$0.56^{+0.01}_{-0.01}$	$2.81^{+0.14}_{-0.11}$	$222_{-18}^{+32}$
WISE 0325+0831	0.5	$932^{+2}_{-2}$	$3.82^{+0.00}_{-0.00}$	$-0.14^{+0.01}_{-0.01}$	$-498^{+198}_{-185}{}^{(26)}_{(23)}$	$24^{+17}_{-15}$	$-19.624^{+0.036}_{-0.033}^{(0.004)}_{(0.004)}$	$0.85^{+0.05}_{-0.04}$	$1.93^{+0.24}_{-0.20}$	$17^{+0}_{-0}$
2MASS 0415-0935	0.5	$824^{+1}_{-1}$	$4.26^{+0.00}_{-0.01}$	$-0.03^{+0.00}_{-0.00}$	$-66^{+179}_{-179} \stackrel{(8)}{_{(8)}}$	$29^{+24}_{-20}$	$-19.227^{+0.012}_{-0.012} \stackrel{(0.002)}{(0.002)}$	$0.60^{+0.01}_{-0.01}$	$2.64^{+0.10}_{-0.11}$	$133^{+2}_{-4}$
WISE 0458+6434	0.5	$584^{+147}_{-17}$	$5.46^{+0.03}_{-1.74}$	$-0.11^{+0.03}_{-0.37}$	$-769^{+437}_{-309}^{(514)}_{(123)}$	$55^{+243}_{-43}$	$-19.047^{+0.109}_{-0.587} \stackrel{(0.088)}{(0.593)}$	$1.18^{+0.17}_{-0.58}$	$165.86^{+58.38}_{-165.08}$	$23^{+7}_{-5}$
VISE 0500-1223	0.5	$640^{+110}_{-24}$	$5.46^{+0.04}_{-1.47}$	$-0.15^{+0.06}_{-0.35}$	$-211^{+314}_{-303} \stackrel{(282)}{(220)}$	$46^{+201}_{-33}$	$-19.604^{+0.136}_{-0.386}^{(0.097)}_{(0.395)}$	$0.80^{+0.14}_{-0.29}$	$78.00^{+32.51}_{-76.94}$	$62^{+25}_{-17}$
VISE 0521+1025	0.8	$873^{+7}_{-2}$	$3.61^{+0.01}_{-0.11}$	$-0.14^{+0.01}_{-0.04}$	$-124^{+182}_{-182} \stackrel{(20)}{_{(49)}}$	$19^{+13}_{-13}$	$-19.072^{+0.024}_{-0.024}^{+0.004}_{(0.008)}$	$0.89^{+0.04}_{-0.04}$	$1.27^{+0.15}_{-0.25}$	$9^{+0}_{-3}$
GPS 0521+3640	0.8	$777^{+3}_{-2}$	$4.50^{+0.01}_{-0.00}$	$-0.24^{+0.01}_{-0.01}$	$-212^{+184}_{-187}{}^{(31)}_{(34)}$	$38^{+28}_{-28}$	$-19.777^{+0.019}_{-0.018} \stackrel{(0.006)}{(0.007)}$	$0.46^{+0.01}_{-0.01}$	$2.69^{+0.15}_{-0.13}$	$434^{+8}_{-6}$
VISE 0614+0951	0.8	$966^{+1}_{-1}$	$4.01^{+0.01}_{-0.01}$	$-0.06^{+0.01}_{-0.01}$	$-647^{+180}_{-180}^{(15)}_{(15)}$	$29^{+21}_{-20}$	$-19.920^{+0.024}_{-0.024} \stackrel{(0.002)}{(0.002)}$	$0.83^{+0.04}_{-0.04}$	$2.90^{+0.28}_{-0.25}$	$32^{+1}_{-1}$
VISE 0623-0456	0.5	$827^{+13}_{-13}$	$4.10^{+0.12}_{-0.09}$	$-0.31^{+0.06}_{-0.04}$	$-155^{+216}_{-220}^{(116)}_{(121)}$	$28^{+18}_{-19}$	$-19.850^{+0.051}_{-0.041} \stackrel{(0.033)}{(0.030)}$	$0.59^{+0.04}_{-0.03}$	$1.80^{+0.66}_{-0.38}$	$64^{+27}_{-17}$
JGPS 0722-0540	0.5	$709_{-1}^{+1}$	$3.43^{+0.02}_{-0.01}$	$-0.04^{+0.01}_{-0.01}$	$-194^{+180}_{-179}^{(15)}_{(15)}$	$10^{+7}_{-7}$	$-19.333^{+0.009}_{-0.009} \stackrel{(0.003)}{_{(0.003)}}$	$0.38^{+0.01}_{-0.01}$	$0.16^{+0.01}_{-0.01}$	$9^{+1}_{-0}$
MASS 0727+1710	0.5	$911^{+1}_{-1}$	$4.12^{+0.01}_{-0.01}$	$-0.11^{+0.00}_{-0.00}$	$-5^{+179}_{-179} \stackrel{(9)}{(9)}$	$32^{+23}_{-22}$	$-19.362^{+0.012}_{-0.012} \stackrel{(0.002)}{(0.002)}$	$0.80^{+0.01}_{-0.01}$	$3.40^{+0.14}_{-0.13}$	$57^{+2}_{-2}$
MASS 0729-3954	0.5	837+5	$4.15^{+0.04}_{-0.04}$	$-0.45^{+0.01}_{-0.01}$	$-320^{+182}_{-183} \stackrel{(32)}{_{(32)}}$	$32^{+22}_{-22}$	$-19.358^{+0.041}_{-0.041} \stackrel{(0.011)}{_{(0.012)}}$	$0.72^{+0.06}_{-0.05}$	$2.92^{+0.62}_{-0.51}$	$76^{+13}_{-12}$
MASS 0939-2448	0.5	$667^{+0}_{-0}$	$5.16^{+0.00}_{-0.00}$	$-0.32^{+0.00}_{-0.00}$	$-80^{+182}_{-182} \stackrel{(29)}{_{(20)}}$	$82^{+92}_{-57}$	$-18.799^{+0.039}_{-0.046}^{+0.039}_{(0.002)}^{(0.002)}$	$0.92^{+0.05}_{-0.05}$	$49.15^{+5.44}_{-6.95}$	6551+43
JLAS 1029+0935	0.5	$818^{+3}_{-5}$	$3.70^{+0.02}_{-0.02}$	$-0.08^{+0.02}_{-0.02}$	$-1^{+182}_{-182} \stackrel{(31)}{_{(35)}}$	$21^{+10}_{-15}$	$-19.923^{+0.014}_{-0.010} {}^{(0.012)}_{(0.008)}$	$0.69^{+0.03}_{-0.02}$	$0.96^{+0.09}_{-0.06}$	$16^{+1}_{-1}$
VISE 1039-1600	0.5	$860^{+6}_{-6}$	$3.84^{+0.05}_{-0.14}$	$-0.24^{+0.03}_{-0.04}$	$-381^{+190}_{-190} \stackrel{(64)}{_{(65)}}$	$28^{+19}_{-19}$	$-19.836^{+0.021}_{-0.021} \stackrel{(0.013)}{_{(0.013)}}$	$1.15^{+0.06}_{-0.05}$	$3.67^{+0.66}_{-1.05}$	$22^{+5}_{-10}$
VISE 1052–1942	0.5	$883^{+1}_{-2}$	$3.83^{+0.01}_{-0.00}$	$-0.15^{+0.01}_{-0.01}$	$-303^{+205}_{-189}^{(28)}_{(23)}$	$25^{+17}_{-17}$	$-19.887^{+0.031}_{-0.025} \stackrel{(0.003)}{(0.002)}$	$0.73^{+0.04}_{-0.03}$	$1.43^{+0.17}_{-0.12}$	$20^{+0}_{-0}$
MASS 1114-2618	0.5	$809^{+2}_{-2}$	$4.06^{+0.02}_{-0.02}$	$-0.45^{+0.01}_{-0.01}$	$-292^{+180}_{-180}_{(23)}^{(23)}$	$27^{+18}_{-18}$	$-19.218^{+0.021}_{-0.021} \stackrel{(0.005)}{(0.005)}$	$0.59^{+0.02}_{-0.01}$	$1.62^{+0.10}_{-0.10}$	$59^{+4}_{-4}$
/ISE 1124-0421	0.5	$921^{+1}_{-2}$	$3.88^{+0.01}_{-0.00}$	$-0.26^{+0.01}_{-0.01}$	$-545^{+185}_{-199}^{(22)}_{(24)}$	$25^{+20}_{-16}$	$-19.820^{+0.027}_{-0.025} \stackrel{(0.004)}{(0.003)}$	$0.93^{+0.07}_{-0.06}$	$2.64^{+0.42}_{-0.32}$	$22^{+0}_{-0}$
MASS 1217-0311	0.5	$908^{+2}_{-2}$	$4.00^{+0.02}_{-0.01}$	$-0.02^{+0.01}_{-0.01}$	$-77^{+181}_{-181} \stackrel{(26)}{(27)}$	$30^{+21}_{-21}$	$-19.483^{+0.013}_{-0.013} \stackrel{(0.004)}{(0.004)}$	$0.85^{+0.02}_{-0.02}$	$2.95^{+0.24}_{-0.20}$	$37^{+4}_{-1}$
VISE 1254-0728	0.5	$938^{+9}_{-9}$	$4.27^{+0.08}_{-0.25}$	$-0.20^{+0.04}_{-0.06}$	$-219^{+199}_{-198} {}^{(85)}_{(85)}$	$36^{+26}_{-25}$	$-20.234^{+0.021}_{-0.020} \stackrel{(0.017)}{(0.017)}$	$0.80^{+0.06}_{-0.05}$	$4.49^{+1.46}_{-1.81}$	$93^{+105}_{-58}$
/ISE 1257+4008	0.5	$946^{+5}_{-6}$	$4.67^{+0.07}_{-0.06}$	$-0.04^{+0.02}_{-0.02}$	$-587^{+185}_{-185}^{(48)}_{(48)}$	$58^{+40}_{-39}$	$-20.104^{+0.026}_{-0.026} \stackrel{(0.017)}{(0.009)}$	$0.67^{+0.03}_{-0.03}$	$8.56^{+1.65}_{-1.22}$	$428^{+132}_{-78}$
oss 458C	0.5	$836^{+3}_{-3}$	$4.09^{+0.02}_{-0.01}$	$-0.50^{+0.00}_{-0.00}$	$-168^{+182}_{-183} \stackrel{(24)}{_{(29)}}$	$30^{+17}_{-21}$	$-19.805^{+0.021}_{-0.018} \stackrel{(0.006)}{(0.006)}$	$0.62^{+0.02}_{-0.01}$	$1.90^{+0.12}_{-0.10}$	$72^{+4}_{-4}$
/ISE 1322–2340	0.5	826+6	$4.02^{+0.09}_{-0.07}$	$-0.40^{+0.02}_{-0.02}$	$-104^{+186}_{-187}$ (53)	$33^{+22}_{-22}$	$-19.567^{+0.064}_{-0.059} \stackrel{(0.000)}{(0.015)}$	$0.92^{+0.09}_{-0.08}$	$3.61^{+1.14}_{-0.78}$	$49^{+21}_{-12}$
LAS 1416+1348	0.5	$612^{+1}_{-1}$	$5.50^{+0.00}_{-0.00}$	$-0.39^{+0.00}_{-0.00}$	$-598^{+183}_{-183} \stackrel{(33)}{(38)}$	$176^{+130}_{-123}$	$-19.190^{+0.013}_{-0.013} \stackrel{(0.006)}{(0.006)}$	$1.02^{+0.02}_{-0.02}$	$131.62^{+4.36}_{-4.36}$	
VISE 1457+5815	0.5	908 <sup>+4</sup> <sub>-7</sub>	$4.07^{+0.12}_{-0.04}$	$-0.30^{+0.04}_{-0.02}$	$-276^{+194}_{-188}$ (52)	$36^{+21}_{-25}$	$-19.978^{+0.029}_{-0.026}$ (0.003)	$0.95^{+0.15}_{-0.11}$	$4.39^{+2.11}_{-1.10}$	$45^{+20}_{-7}$
J 570D	0.5	$825^{+1}_{-1}$	$4.15^{+0.02}_{-0.01}$	$-0.27^{+0.01}_{-0.01}$	$-118^{+180}_{-180} \stackrel{(21)}{(22)}$	$35^{+23}_{-24}$	$-19.010^{+0.020}_{-0.020} \stackrel{(0.004)}{(0.004)}$	$0.79^{+0.02}_{-0.02}$	$3.62^{+0.21}_{-0.19}$	$82^{+5}_{-4}$
PSO J224+47	0.8	$921^{+4}_{-3}$	$3.67^{+0.32}_{-0.01}$	$-0.18^{+0.05}_{-0.02}$	$-360^{+219}_{-198}$ (59)	$24^{+11}_{-16}$	$-20.090^{+0.033}_{-0.029} \stackrel{(0.004)}{(0.021)}$	$0.79^{+0.07}_{-0.05}$	$1.23^{+1.12}_{-0.19}$	$10^{+23}_{-0}$
SDSS 1504+1027	0.8	$934^{+3}_{-4}$	$3.92^{+0.01}_{-0.01}$	$-0.33^{+0.01}_{-0.01}$	$-874^{+193}_{-240}$ (35)	$29_{-19}^{+19}$	$-19.966^{+0.027}_{-0.022} \stackrel{(0.021)}{_{(0.006)}}$	$0.98^{+0.05}_{-0.04}$	$3.17^{+0.36}_{-0.26}$	$23^{+1}_{-1}$

Table 9 (Continued)

			Fitted Parameters <sup>a</sup>						Derived Parameters <sup>b</sup>		
Object	Slit	$T_{ m eff}$	logg	Z	$v_{\rm r}$	vsini	$\log\Omega$	R	M	Age	
	(")	(K)	(dex)	(dex)	$(\text{km s}^{-1})$	$(km s^{-1})$	(dex)	$(R_{\mathrm{Jup}})$	$(M_{ m Jup})$	(Myr)	
2MASS 1553+1532	0.5	$909^{+2}_{-8}$	$4.12^{+0.17}_{-0.03}$	$-0.20^{+0.05}_{-0.01}$	$-129^{+181}_{-181} {}^{(30)}_{(28)}$	$41^{+30}_{-28}$	$-19.406^{+0.016}_{-0.015}$ (0.016)	$1.14^{+0.02}_{-0.02}$	$6.67^{+3.76}_{-0.46}$	$52^{+65}_{-4}$	
SDSS 1628+2308	0.8	$914^{+2}_{-2}$	$4.26^{+0.01}_{-0.01}$	$-0.11^{+0.01}_{-0.01}$	$-272^{+181}_{-180}{}^{(26)}_{(25)}$	$37^{+26}_{-25}$	$-19.794^{+0.013}_{-0.013} \stackrel{(0.005)}{_{(0.005)}}$	$0.73^{+0.01}_{-0.01}$	$3.92^{+0.16}_{-0.16}$	$108^{+9}_{-5}$	
WISE 1653+4444	0.5	$834^{+5}_{-5}$	$4.24^{+0.03}_{-0.05}$	$-0.09^{+0.02}_{-0.03}$	$-193^{+184}_{-184}{}^{(44)}_{(44)}$	$32^{+21}_{-21}$	$-20.040^{+0.023}_{-0.023}^{+0.023}_{(0.011)}^{+0.023}_{-0.011}$	$0.54^{+0.02}_{-0.02}$	$2.05^{+0.24}_{-0.24}$	$118^{+20}_{-21}$	
WISE 1711+3500	0.5	$807^{+9}_{-9}$	$3.90^{+0.12}_{-0.05}$	$-0.30^{+0.02}_{-0.03}$	$-358^{+223}_{-202}^{(88)}_{(72)}$	$26^{+21}_{-16}$	$-20.097^{+0.076}_{-0.063}^{+0.076}_{(0.025)}^{+0.076}_{(0.025)}$	$0.96^{+0.12}_{-0.09}$	$3.10^{+1.05}_{-0.66}$	$34^{+18}_{-6}$	
	0.8	$812^{+5}_{-5}$	$3.74^{+0.07}_{-0.09}$	$-0.37^{+0.04}_{-0.03}$	$-573^{+195}_{-233}^{(46)}_{(56)}$	$26^{+16}_{-18}$	$-20.062^{+0.073}_{-0.060}^{+0.073}_{(0.013)}^{(0.015)}$	$1.00^{+0.12}_{-0.09}$	$2.26^{+0.82}_{-0.52}$	$18^{+7}_{-5}$	
WISE 1741+2553	0.8	$748^{+1}_{-1}$	$4.00^{+0.00}_{-0.00}$	$-0.00^{+0.00}_{-0.00}$	$-267^{+179}_{-179}{}^{(10)}_{(10)}$	$21^{+16}_{-14}$	$-19.234^{+0.016\;(0.003)}_{-0.016\;(0.002)}$	$0.49^{+0.01}_{-0.01}$	$0.95^{+0.04}_{-0.04}$	$62^{+1}_{-1}$	
WISE 1809+3838	0.8	$856^{+5}_{-5}$	$3.71^{+0.10}_{-0.11}$	$-0.10^{+0.03}_{-0.04}$	$-339^{+190}_{-190}_{(63)}^{(61)}$	$20^{+14}_{-14}$	$-20.033^{+0.027}_{-0.027}^{(0.012)}_{(0.011)}$	$0.79^{+0.04}_{-0.04}$	$1.30^{+0.38}_{-0.31}$	$14^{+7}_{-5}$	
WISE 1813+2835	0.5	$838^{+3}_{-3}$	$3.95^{+0.03}_{-0.03}$	$-0.14^{+0.01}_{-0.01}$	$-66^{+181}_{-181}_{(25)}^{(25)}$	$26^{+18}_{-17}$	$-19.826^{+0.025}_{-0.025}{}^{(0.006)}_{(0.006)}$	$0.72^{+0.03}_{-0.03}$	$1.85^{+0.19}_{-0.17}$	$39^{+4}_{-4}$	
WISE 1852+3537	0.5	$923^{+2}_{-1}$	$4.11^{+0.02}_{-0.02}$	$-0.00^{+0.00}_{-0.00}$	$-157^{+180}_{-180}_{(15)}^{(15)}$	$34^{+23}_{-23}$	$-19.804^{+0.024}_{-0.024}_{(0.003)}^{(0.003)}$	$0.82^{+0.04}_{-0.04}$	$3.47^{+0.41}_{-0.36}$	$54^{+4}_{-3}$	
WISE 1959-3338	0.5	$832^{+3}_{-3}$	$4.00^{+0.01}_{-0.00}$	$-0.09^{+0.01}_{-0.01}$	$-99^{+183}_{-183}  {}^{(32)}_{(33)}$	$28^{+16}_{-19}$	$-19.793^{+0.023}_{-0.021}^{(0.007)}_{(0.007)}$	$0.64^{+0.03}_{-0.02}$	$1.68^{+0.15}_{-0.14}$	$47^{+2}_{-1}$	
WISE 2000+3629	0.5	$843^{+2}_{-2}$	$3.83^{+0.00}_{-0.00}$	$-0.17^{+0.00}_{-0.00}$	$-317^{+180}_{-180}{}^{(17)}_{(17)}$	$23^{+16}_{-16}$	$-19.283^{+0.006}_{-0.006}{}^{(0.004)}_{(0.004)}$	$0.75^{+0.02}_{-0.02}$	$1.55^{+0.07}_{-0.07}$	$23^{+0}_{-0}$	
WISE 2157+2659	0.8	$867^{+2}_{-2}$	$4.09^{+0.01}_{-0.01}$	$-0.19^{+0.01}_{-0.01}$	$-228^{+206}_{-191}{}^{(29)}_{(20)}$	$34^{+14}_{-23}$	$-20.017^{+0.026}_{-0.018}^{+0.026}_{(0.004)}$	$0.68^{+0.04}_{-0.03}$	$2.27^{+0.31}_{-0.19}$	$57^{+2}_{-2}$	
WISE 2209-2734	0.8	$763^{+4}_{-11}$	$5.50^{+0.00}_{-0.00}$	$-0.10^{+0.01}_{-0.01}$	$-359^{+185}_{-192}{}^{(22)}_{(24)}$	$104^{+119}_{-69}$	$-19.506^{+0.040}_{-0.032}^{+0.040}_{(0.012)}^{+0.040}$	$1.06^{+0.08}_{-0.07}$	$141.68^{+22.52}_{-17.26}$		
WISE 2213+0911	0.5	$934^{+3}_{-3}$	$4.32^{+0.01}_{-0.01}$	$-0.14^{+0.01}_{-0.01}$	$-44^{+180}_{-180}_{(24)}^{(29)}$	$40^{+29}_{-26}$	$-20.016^{+0.031}_{-0.026}^{+0.031}_{(0.005)}^{+0.031}_{(0.005)}$	$0.82^{+0.07}_{-0.05}$	$5.58^{+1.07}_{-0.73}$	$140^{+10}_{-12}$	
WISE 2226+0440	0.5	$848^{+2}_{-4}$	$4.04^{+0.04}_{-0.03}$	$-0.04^{+0.01}_{-0.02}$	$-36^{+181}_{-181} {}^{(25)}_{(32)}$	$30^{+21}_{-19}$	$-19.926^{+0.045}_{-0.031}^{(0.008)}_{(0.006)}$	$0.88^{+0.19}_{-0.10}$	$3.37^{+1.67}_{-0.73}$	$50^{+5}_{-4}$	
WISE 2255-3118	0.5	$807^{+3}_{-3}$	$3.73^{+0.03}_{-0.03}$	$-0.00^{+0.01}_{-0.01}$	$-865^{+183}_{-182}^{(37)}_{(37)}$	$20^{+13}_{-13}$	$-19.911^{+0.014}_{-0.014} {}^{(0.008)}_{(0.008)}$	$0.68^{+0.04}_{-0.04}$	$1.00^{+0.15}_{-0.13}$	$19^{+2}_{-2}$	
WISE 2319-1844	0.5	$805^{+8}_{-8}$	$4.16^{+0.07}_{-0.06}$	$-0.49^{+0.02}_{-0.01}$	$-676^{+195}_{-211}^{(66)}_{(72)}$	$28^{+16}_{-19}$	$-20.038^{+0.033\ (0.023)}_{-0.031\ (0.024)}$	$0.49^{+0.03}_{-0.02}$	$1.36^{+0.32}_{-0.25}$	$87^{+28}_{-20}$	
ULAS 2321+1354	0.8	$829^{+2}_{-3}$	$4.11^{+0.02}_{-0.01}$	$-0.19\substack{+0.01 \\ -0.01}$	$-462^{+186}_{-198}{}^{(29)}_{(31)}$	$31^{+19}_{-21}$	$-19.787^{+0.015}_{-0.013} \stackrel{(0.006)}{_{(0.005)}}$	$0.66^{+0.02}_{-0.02}$	$2.26^{+0.21}_{-0.17}$	$74^{+6}_{-4}$	
WISE 2340-0745	0.5	$953^{+1}_{-1}$	$4.41^{+0.02}_{-0.02}$	$-0.19\substack{+0.01 \\ -0.01}$	$-209^{+180}_{-180}_{(18)}^{(18)}$	$54^{+39}_{-37}$	$-19.783^{+0.012}_{-0.012} {\scriptstyle{(0.003)}\atop{(0.003)}}$	$1.16^{+0.08}_{-0.07}$	$13.97^{+2.13}_{-1.76}$	$280^{+23}_{-23}$	
WISE 2348-1028	0.5	$907^{+2}_{-3}$	$4.15^{+0.04}_{-0.03}$	$-0.03^{+0.01}_{-0.01}$	$-32^{+181}_{-181} {}^{(31)}_{(26)}$	$36^{+19}_{-24}$	$-19.895^{+0.031}_{-0.026}  {}^{(0.006)}_{(0.005)}$	$0.72^{+0.06}_{-0.05}$	$2.96^{+0.59}_{-0.40}$	$64^{+10}_{-7}$	

#### Notes.

<sup>&</sup>lt;sup>a</sup> We report the median and  $1\sigma$  errors of each parameter with the systematic errors in  $\nu_r$  and logΩ incorporated (Section 3.1). The formal  $1\sigma$  errors of  $\nu_r$  and logΩ directly from the spectral-fitting process are shown in parentheses.

<sup>&</sup>lt;sup>b</sup> Parameters are derived in the same approach as that in Table 5. WISE 0245-3450 lacks a parallax and thus has no radius or mass results. Ages >12 Gyr are shown as "...."

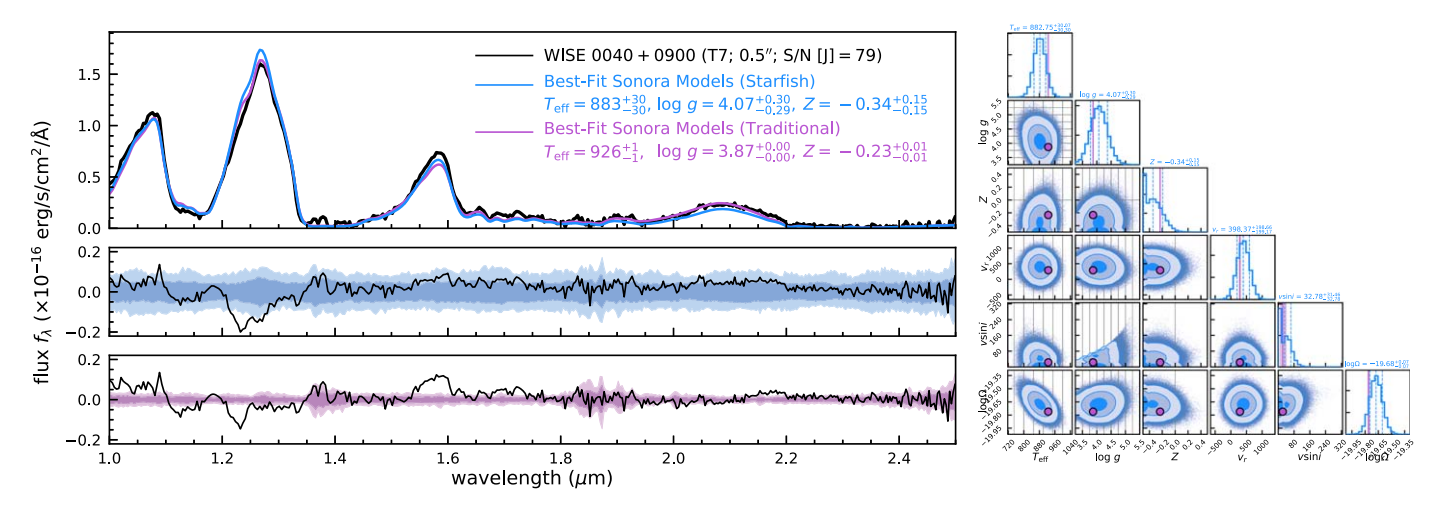


Figure 20. Comparisons of results from Starfish and traditional forward-modeling analyses, with a similar format to Figure 2. Left: The upper panel shows the observed spectrum (black) and the median model spectra of those interpolated at parameters drawn from the MCMC chains based on the Starfish (blue) and traditional (purple) methods. The middle and lower panels show the residual of each method (data—model; black). Right: Posteriors of the six physical parameters  $\{T_{\rm eff}, \log g, Z, v_{\rm r}, v \sin i, \log \Omega\}$  derived from the Starfish-based forward-modeling analysis (blue). We overlay the median values and uncertainties from the traditional method (purple), shown as vertical lines and shadows in the 1D histograms and as circles and error bars in the 2D histograms. We use gray vertical and horizontal lines to mark the  $\{T_{\rm eff}, \log g, Z\}$  grid points of the cloudless Sonora—Bobcat models. Figures of the spectral-fitting results for our entire sample (55 late-T dwarfs with 57 spectra) are accessible online.

(The complete figure set (57 images) is available.)

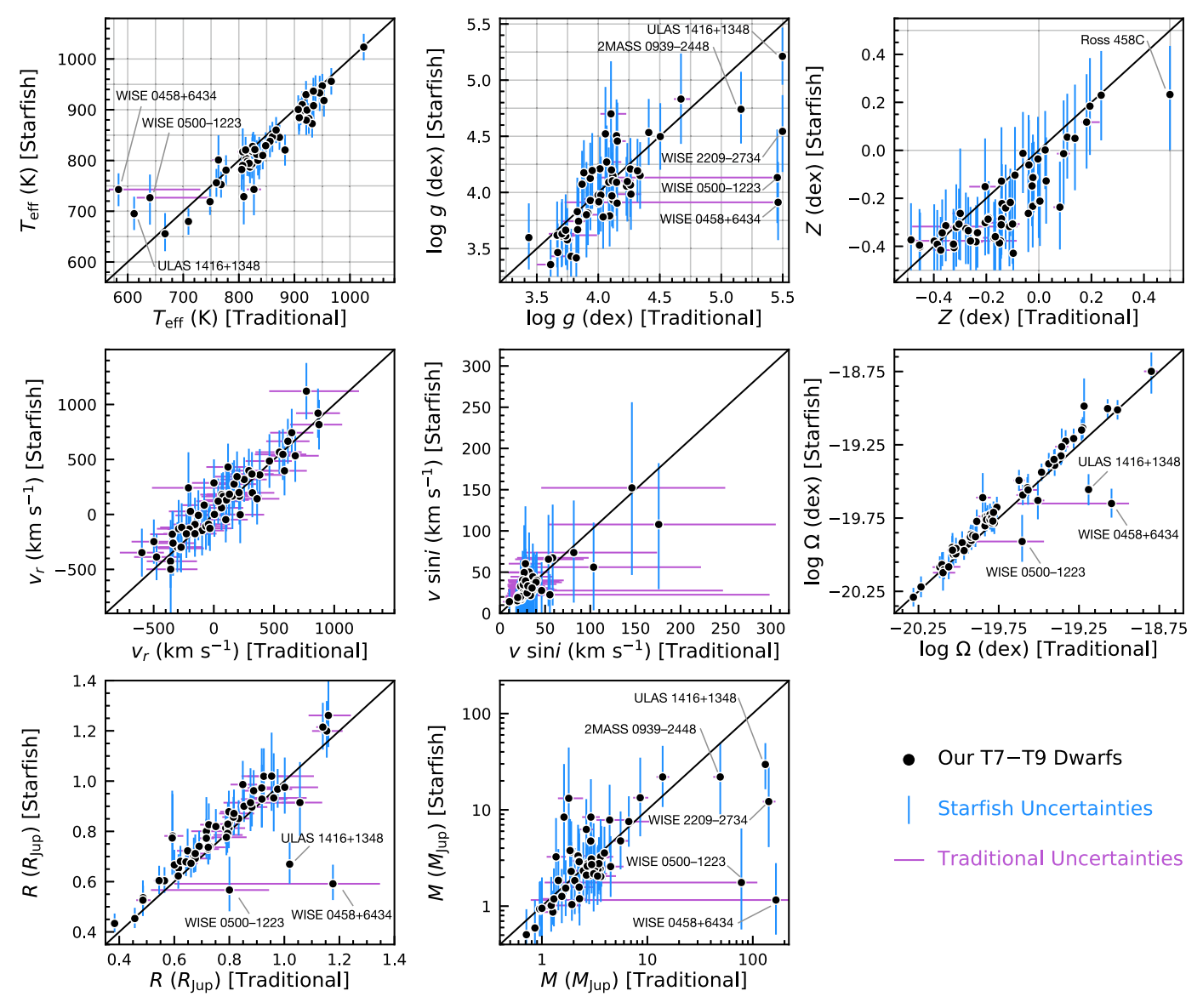


Figure 21. Comparison of eight physical parameters of our late-T dwarfs  $\{T_{\rm eff}, \log g, Z, v_{\rm r}, v \sin i, \log \Omega, R, M\}$  as inferred from Starfish and traditional forward-modeling analysis (masses are compared in the logarithmic scale). We use gray vertical and horizontal lines to mark the  $\{T_{\rm eff}, \log g, Z\}$  grids of the cloudless Sonora-Bobcat models. The results from the two methods are generally consistent within the uncertainties, although there are systematic differences in almost all parameters except for  $v_{\rm r}$  and  $v \sin i$ . We label the objects that have significantly different parameters from the two methods and discuss them in Appendix C.

## **ORCID iDs**

Zhoujian Zhang (张周健) <sup>©</sup> https://orcid.org/0000-0002-3726-4881

Michael C. Liu https://orcid.org/0000-0003-2232-7664 Mark S. Marley https://orcid.org/0000-0002-5251-2943 Michael R. Line https://orcid.org/0000-0002-2338-476X William M. J. Best https://orcid.org/0000-0003-0562-1511

## References

Aberasturi, M., Burgasser, A. J., Mora, A., et al. 2014, AJ, 148, 129
Allard, F. 2014, in IAU Symp. 299, Exploring the Formation and Evolution of Planetary Systems, ed. M. Booth, B. C. Matthews, & J. R. Graham (Cambridge: Cambridge University Press), 271

Allard, F., Homeier, D., & Freytag, B. 2011, in ASP Conf. Ser. 448, Model Atmospheres From Very Low Mass Stars to Brown Dwarfs, ed. C. Johns-Krull, M. K. Browning, & A. A. West (San Francisco, CA: ASP), 91

Allard, F., Homeier, D., & Freytag, B. 2012, RSPTA, 370, 2765

Allard, N. F., Royer, A., Kielkopf, J. F., & Feautrier, N. 1999, PhRvA, 60, 1021

Allard, N. F., Spiegelman, F., & Kielkopf, J. F. 2007, A&A, 465, 1085 Allard, N. F., Spiegelman, F., & Kielkopf, J. F. 2016, A&A, 589, A21 Allen, P. R., Koerner, D. W., Reid, I. N., & Trilling, D. E. 2005, ApJ, 625, 385 Allers, K. N., & Liu, M. C. 2013, ApJ, 772, 79

Astropy Collaboration, Price-Whelan, A. M., Sipőcz, B. M., et al. 2018, AJ, 156, 123

Astropy Collaboration, Robitaille, T. P., Tollerud, E. J., et al. 2013, A&A, 558, A33

Baraffe, I., Chabrier, G., Allard, F., & Hauschildt, P. H. 1998, A&A, 337, 403Baraffe, I., Chabrier, G., Barman, T. S., Allard, F., & Hauschildt, P. H. 2003, A&A, 402, 701

Barnes, J. W., & Fortney, J. J. 2003, ApJ, 588, 545 Baudino, J.-L., Mollière, P., Venot, O., et al. 2017, ApJ, 850, 150 Beatty, T. G., Morley, C. V., Curtis, J. L., et al. 2018, AJ, 156, 168

Bell, C. P. M., Mamajek, E. E., & Naylor, T. 2015, MNRAS, 454, 593
Best, W. M. J., Dupuy, T. J., Liu, M. C., Siverd, R. J., & Zhang, Z. 2020a, The UltracoolSheet: Photometry, Astrometry, Spectroscopy, and Multiplicity for 3000+ Ultracool Dwarfs and Imaged Exoplanets v 1.0.0, Zenodo, 10.5281/

Best, W. M. J., Liu, M. C., Magnier, E. A., et al. 2015, ApJ, 814, 118

```
Best, W. M. J., Liu, M. C., Magnier, E. A., et al. 2017, ApJ, 837, 95
Best, W. M. J., Liu, M. C., Magnier, E. A., & Dupuy, T. J. 2020b, AJ, 159, 257
Best, W. M. J., Liu, M. C., Magnier, E. A., & Dupuy, T. J. 2021, AJ, 161, 42
Best, W. M. J., Magnier, E. A., Liu, M. C., et al. 2018, ApJS, 234, 1
Bihain, G., Scholz, R. D., Storm, J., & Schnurr, O. 2013, A&A, 557, A43
Bond, J. C., Tinney, C. G., Butler, R. P., et al. 2006, MNRAS, 370, 163
Bowler, B. P., Dupuy, T. J., Endl, M., et al. 2018, AJ, 155, 159
Bowler, B. P., Liu, M. C., & Dupuy, T. J. 2010a, ApJ, 710, 45
Bowler, B. P., Liu, M. C., Dupuy, T. J., & Cushing, M. C. 2010b, ApJ, 723, 850
Brandt, T. D., Dupuy, T. J., Bowler, B. P., et al. 2020, AJ, 160, 196
Brewer, J. M., Fischer, D. A., Valenti, J. A., & Piskunov, N. 2016, ApJS,
   225, 32
Burgasser, A. J. 2004, ApJS, 155, 191
Burgasser, A. J. 2007, ApJ, 658, 617
Burgasser, A. J. 2014, in ASI Conf. Ser. 11, ed. H. P. Singh, P. Prugniel, &
   I. Vauglin (Bengalore: ASI), 7
Burgasser, A. J. & Splat Development Team 2017, in ASI Conf. Ser. 14,
   International Workshop on Stellar Spectral Libraries, ed. P. Coelho,
   L. Martins, & E. Griffin (Tavistock: ASI), 7
Burgasser, A. J., Burrows, A., & Kirkpatrick, J. D. 2006a, ApJ, 639, 1095
Burgasser, A. J., Cruz, K. L., Cushing, M., et al. 2010a, ApJ, 710, 1142
Burgasser, A. J., Geballe, T. R., Leggett, S. K., Kirkpatrick, J. D., &
   Golimowski, D. A. 2006b, ApJ, 637, 1067
Burgasser, A. J., Gelino, C. R., Cushing, M. C., & Kirkpatrick, J. D. 2012,
    ApJ, 745, 26
Burgasser, A. J., Kirkpatrick, J. D., Brown, M. E., et al. 1999, ApJL, 522, L65
Burgasser, A. J., Kirkpatrick, J. D., Brown, M. E., et al. 2002, ApJ, 564, 421
Burgasser, A. J., Kirkpatrick, J. D., Cruz, K. L., et al. 2006c, ApJS, 166, 585
Burgasser, A. J., Kirkpatrick, J. D., Cutri, R. M., et al. 2000, ApJL, 531, L57
Burgasser, A. J., Looper, D., & Rayner, J. T. 2010b, AJ, 139, 2448
Burgasser, A. J., Looper, D. L., Kirkpatrick, J. D., Cruz, K. L., & Swift, B. J.
   2008a, ApJ, 674, 451
Burgasser, A. J., McElwain, M. W., Kirkpatrick, J. D., et al. 2004, AJ,
Burgasser, A. J., Tinney, C. G., Cushing, M. C., et al. 2008b, ApJL, 689, L53
Burningham, B., Cardoso, C. V., Smith, L., et al. 2013, MNRAS, 433, 457
Burningham, B., Leggett, S. K., Lucas, P. W., et al. 2010a, MNRAS, 404, 1952
Burningham, B., Lucas, P. W., Leggett, S. K., et al. 2011, MNRAS, 414, L90
Burningham, B., Marley, M. S., Line, M. R., et al. 2017, MNRAS, 470, 1177
Burningham, B., Pinfield, D. J., Leggett, S. K., et al. 2008, MNRAS, 391, 320
Burningham, B., Pinfield, D. J., Leggett, S. K., et al. 2009, MNRAS, 395, 1237
Burningham, B., Pinfield, D. J., Lucas, P. W., et al. 2010b, MNRAS, 406, 1885
Burrows, A., Burgasser, A. J., Kirkpatrick, J. D., et al. 2002, ApJ, 573, 394
Burrows, A., Heng, K., & Nampaisarn, T. 2011, ApJ, 736, 47
Burrows, A., Hubbard, W. B., Lunine, J. I., & Liebert, J. 2001, RvMP, 73, 719
Burrows, A., & Liebert, J. 1993, RvMP, 65, 301
Burrows, A., Marley, M., Hubbard, W. B., et al. 1997, ApJ, 491, 856
Burrows, A., Marley, M. S., & Sharp, C. M. 2000, ApJ, 531, 438
Burrows, A., & Sharp, C. M. 1999, ApJ, 512, 843
Burrows, A., Sudarsky, D., & Hubeny, I. 2006, ApJ, 640, 1063
Chabrier, G., Baraffe, I., Allard, F., & Hauschildt, P. 2000, ApJ, 542, 464
Chambers, K. C., Magnier, E. A., Metcalfe, N., et al. 2016, arXiv:1612.05560
Chiu, K., Fan, X., Leggett, S. K., et al. 2006, AJ, 131, 2722
Coles, P. A., Yurchenko, S. N., & Tennyson, J. 2019, MNRAS, 490, 4638
Cushing, M. C., Kirkpatrick, J. D., Gelino, C. R., et al. 2011, ApJ, 743, 50
Cushing, M. C., Kirkpatrick, J. D., Gelino, C. R., et al. 2014, AJ, 147, 113
Cushing, M. C., Marley, M. S., Saumon, D., et al. 2008, ApJ, 678, 1372
Cushing, M. C., Vacca, W. D., & Rayner, J. T. 2004, PASP, 116, 362
Cutri, R. M., Wright, E. L., Conrow, T., et al. 2014, VizieR On-line Data
   Catalog: II/328
Czekala, I., Andrews, S. M., Mandel, K. S., Hogg, D. W., & Green, G. M.
   2015, ApJ, 812, 128
Dahn, C. C., Harris, H. C., Vrba, F. J., et al. 2002, AJ, 124, 1170
Day-Jones, A. C., Marocco, F., Pinfield, D. J., et al. 2013, MNRAS, 430, 1171
Deacon, N. R., Magnier, E. A., Liu, M. C., et al. 2017, MNRAS, 467, 1126
Del Burgo, C., Martín, E. L., Zapatero Osorio, M. R., & Hauschildt, P. H.
   2009, A&A, 501, 1059
Díaz, R. F., Damiani, C., Deleuil, M., et al. 2013, A&A, 551, L9
Dieterich, S. B., Weinberger, A. J., Boss, A. P., et al. 2018, ApJ, 865, 28
Dupuy, T. J., & Kraus, A. L. 2013, Sci, 341, 1492
Dupuy, T. J., & Liu, M. C. 2012, ApJS, 201, 19
Dupuy, T. J., & Liu, M. C. 2014, ApJ, 790, 133
Dupuy, T. J., & Liu, M. C. 2017, ApJS, 231, 15
Dupuy, T. J., Liu, M. C., & Ireland, M. J. 2009, ApJ, 692, 729
Edge, A., Sutherland, W. & Viking Team 2016, VizieR On-line Data Catalog:
   II/343
```

```
Edvardsson, B., Andersen, J., Gustafsson, B., et al. 1993, A&A, 500, 391
Eisenhardt, P. R. M., Marocco, F., Fowler, J. W., et al. 2020, ApJS, 247, 69
Faherty, J. K., Burgasser, A. J., Cruz, K. L., et al. 2009, AJ, 137, 1
Faherty, J. K., Burgasser, A. J., Walter, F. M., et al. 2012, ApJ, 752, 56
Faherty, J. K., Riedel, A. R., Cruz, K. L., et al. 2016, ApJS, 225, 10
Fegley, B. J., & Lodders, K. 1994, Icar, 110, 117
Filippazzo, J. C., Giorla Godfrey, P., Cruz, K. L., et al. 2016, The BDNYC
   Database v 1.0, Zenodo, 10.5281/zenodo.45169
Filippazzo, J. C., Rice, E. L., Faherty, J., et al. 2015, ApJ, 810, 158
Foreman-Mackey, D., Hogg, D. W., Lang, D., & Goodman, J. 2013, PASP,
Fortney, J. J., Marley, M. S., Saumon, D., & Lodders, K. 2008, ApJ, 683, 1104
Gagné, J., Mamajek, E. E., Malo, L., et al. 2018, ApJ, 856, 23
Gaia Collaboration, Brown, A. G. A., Vallenari, A., et al. 2016a, A&A,
Gaia Collaboration, Brown, A. G. A., Vallenari, A., et al. 2018, A&A, 616, A1
Gaia Collaboration, Prusti, T., de Bruijne, J. H. J., et al. 2016b, A&A, 595, A1
Gelino, C. R., Kirkpatrick, J. D., Cushing, M. C., et al. 2011, AJ, 142, 57
Goldman, B., Marsat, S., Henning, T., Clemens, C., & Greiner, J. 2010,
    INRAS, 405, 1140
Golimowski, D. A., Leggett, S. K., Marley, M. S., et al. 2004, AJ, 127, 3516
Gonzales, E. C., Burningham, B., Faherty, J. K., et al. 2020, ApJ, 905, 46
Gully-Santiago, M. A., Herczeg, G. J., Czekala, I., et al. 2017, ApJ, 836, 200
Hewett, P. C., Warren, S. J., Leggett, S. K., & Hodgkin, S. T. 2006, MNRAS,
Hinkel, N. R., Mamajek, E. E., Turnbull, M. C., et al. 2017, ApJ, 848, 34
Hinkel, N. R., Timmes, F. X., Young, P. A., Pagano, M. D., & Turnbull, M. C.
   2014, AJ, 148, 54
Hinkel, N. R., Young, P. A., Pagano, M. D., et al. 2016, ApJS, 226, 4
Hunter, J. D. 2007, CSE, 9, 90
Ivanyuk, O. M., Jenkins, J. S., Pavlenko, Y. V., Jones, H. R. A., &
   Pinfield, D. J. 2017, MNRAS, 468, 4151
Jenkins, J. S., Jones, H. R. A., Pavlenko, Y., et al. 2008, A&A, 485, 571
Jones, E., Oliphant, T., Peterson, P., et al. 2001, SciPy: Open Source Scientific
   Tools for Python, http://www.scipy.org/
Kirkpatrick, J. D., Cruz, K. L., Barman, T. S., et al. 2008, ApJ, 689, 1295
Kirkpatrick, J. D., Cushing, M. C., Gelino, C. R., et al. 2011, ApJS, 197, 19
Kirkpatrick, J. D., Gelino, C. R., Cushing, M. C., et al. 2012, ApJ, 753, 156
Kirkpatrick, J. D., Martin, E. C., Smart, R. L., et al. 2019, ApJS, 240, 19
Kirkpatrick, J. D., Reid, I. N., Liebert, J., et al. 1999, ApJ, 519, 802
Knapp, G. R., Leggett, S. K., Fan, X., et al. 2004, AJ, 127, 3553
Lawrence, A., Warren, S. J., Almaini, O., et al. 2007, MNRAS, 379, 1599
Lawrence, A., Warren, S. J., Almaini, O., et al. 2012, VizieR On-line Data
   Catalog: II/314
Leggett, S. K., Burningham, B., Saumon, D., et al. 2010, ApJ, 710, 1627
Leggett, S. K., Cushing, M. C., Saumon, D., et al. 2009, ApJ, 695, 1517
Leggett, S. K., Dupuy, T. J., Morley, C. V., et al. 2019, ApJ, 882, 117
Leggett, S. K., Golimowski, D. A., Fan, X., et al. 2002, ApJ, 564, 452
Leggett, S. K., Marley, M. S., Freedman, R., et al. 2007, ApJ, 667, 537
Leggett, S. K., Saumon, D., Marley, M. S., et al. 2012, ApJ, 748, 74
Leggett, S. K., Tremblin, P., Esplin, T. L., Luhman, K. L., & Morley, C. V.
   2017, ApJ, 842, 118
Liebert, J., & Burgasser, A. J. 2007, ApJ, 655, 522
Line, M. R., Marley, M. S., Liu, M. C., et al. 2017, ApJ, 848, 83
Line, M. R., Teske, J., Burningham, B., Fortney, J. J., & Marley, M. S. 2015,
   ApJ, 807, 183
Liu, M. C., Deacon, N. R., Magnier, E. A., et al. 2011a, ApJL, 740, L32
Liu, M. C., Delorme, P., Dupuy, T. J., et al. 2011b, ApJ, 740, 108
Liu, M. C., Dupuy, T. J., & Allers, K. N. 2016, ApJ, 833, 96
Liu, M. C., Dupuy, T. J., Bowler, B. P., Leggett, S. K., & Best, W. M. J. 2012,
     J, 758, 57
Liu, M. C., Dupuy, T. J., & Ireland, M. J. 2008, ApJ, 689, 436
Liu, M. C., Dupuy, T. J., & Leggett, S. K. 2010, ApJ, 722, 311
Liu, M. C., Leggett, S. K., & Chiu, K. 2007, ApJ, 660, 1507
Liu, M. C., Leggett, S. K., Golimowski, D. A., et al. 2006, ApJ, 647, 1393
Lodders, K. 1999, ApJ, 519, 793
Lodders, K. 2002, ApJ, 577, 974
Lodders, K., Palme, H., & Gail, H. P. 2009, Solar System, Landolt-Börnstein -
   Group VI Astronomy and Astrophysics, Vol. 4B (Berlin: Springer), 712
Lodieu, N. 2013, MNRAS, 431, 3222
Lodieu, N., Hambly, N. C., Jameson, R. F., et al. 2007, MNRAS, 374, 372
Looper, D. L., Gelino, C. R., Burgasser, A. J., & Kirkpatrick, J. D. 2008, ApJ,
   685, 1183
Looper, D. L., Kirkpatrick, J. D., & Burgasser, A. J. 2007, AJ, 134, 1162
Lucas, P. W., Tinney, C. G., Burningham, B., et al. 2010, MNRAS, 408, L56
```

Luhman, K. L. 2006, ApJ, 645, 676

```
Luhman, K. L., Loutrel, N. P., McCurdy, N. S., et al. 2012, ApJ, 760, 152
Luhman, K. L., & Mamajek, E. E. 2012, ApJ, 758, 31
Luhman, K. L., Mamajek, E. E., Allen, P. R., & Cruz, K. L. 2009, ApJ,
Luhman, K. L., Patten, B. M., Marengo, M., et al. 2007, ApJ, 654, 570
Mace, G. N., Kirkpatrick, J. D., Cushing, M. C., et al. 2013a, ApJS, 205, 6
Mace, G. N., Kirkpatrick, J. D., Cushing, M. C., et al. 2013b, ApJ, 777, 36
Mace, G. N., Mann, A. W., Skiff, B. A., et al. 2018, ApJ, 854, 145
Mainzer, A., Cushing, M. C., Skrutskie, M., et al. 2011, ApJ, 726, 30
Manjavacas, E., Apai, D., Zhou, Y., et al. 2019, AJ, 157, 101
Marley, M. S., & Robinson, T. D. 2015, ARA&A, 53, 279
Marley, M. S., Saumon, D., Fortney, J. J., et al. 2017, AAS Meeting, 230,
Marley, M. S., Saumon, D., & Goldblatt, C. 2010, ApJL, 723, L117
Marley, M. S., Saumon, D., Visscher, C., et al. 2021, arXiv:2107.07434
Marley, M. S., Seager, S., Saumon, D., et al. 2002, ApJ, 568, 335
Marocco, F., Eisenhardt, P. R. M., Fowler, J. W., et al. 2021, ApJS, 253, 8
McMahon, R. G., Banerji, M., Gonzalez, E., et al. 2013, Msngr, 154, 35
Meisner, A. M., Faherty, J. K., Kirkpatrick, J. D., et al. 2020, ApJ, 899, 123
Metchev, S. A., & Hillenbrand, L. A. 2006, ApJ, 651, 1166
Mollière, P., Wardenier, J. P., van Boekel, R., et al. 2019, A&A, 627, A67
Montet, B. T., Johnson, J. A., Muirhead, P. S., et al. 2015, ApJ, 800, 134
Morley, C. V., Fortney, J. J., Marley, M. S., et al. 2012, ApJ, 756, 172
Mugrauer, M., Seifahrt, A., Neuhäuser, R., & Mazeh, T. 2006, MNRAS,
   373, L31
Nakajima, T., Oppenheimer, B. R., Kulkarni, S. R., et al. 1995, Natur, 378, 463
Oliphant, T. 2006, NumPy: A Guide to NumPy (USA: Trelgol Publishing),
   http://www.numpy.org
Pérez, F., & Granger, B. E. 2007, CSE, 9, 21
Petigura, E. A., & Marcy, G. W. 2011, ApJ, 735, 41
Phillips, M. W., Tremblin, P., Baraffe, I., et al. 2020, A&A, 637, A38
Pinfield, D. J., Burningham, B., Lodieu, N., et al. 2012, MNRAS, 422, 1922
Pinfield, D. J., Gomes, J., Day-Jones, A. C., et al. 2014, MNRAS, 437, 1009
Ramírez, I., Allende Prieto, C., & Lambert, D. L. 2013, ApJ, 764, 78
Rayner, J. T., Toomey, D. W., Onaka, P. M., et al. 2003, PASP, 115, 362
Rice, E. L., Barman, T., Mclean, I. S., Prato, L., & Kirkpatrick, J. D. 2010,
    pJS, 186, 63
Riedel, A. R., Blunt, S. C., Lambrides, E. L., et al. 2017, AJ, 153, 95
Santos, N. C., Israelian, G., & Mayor, M. 2004, A&A, 415, 1153
Saumon, D., & Marley, M. S. 2008, ApJ, 689, 1327
Saumon, D., Marley, M. S., Abel, M., Frommhold, L., & Freedman, R. S.
  2012, ApJ, 750, 74
Saumon, D., Marley, M. S., Cushing, M. C., et al. 2006, ApJ, 647, 552
Saumon, D., Marley, M. S., Leggett, S. K., et al. 2007, ApJ, 656, 1136
Schmidt, S. J., Cruz, K. L., Bongiorno, B. J., Liebert, J., & Reid, I. N. 2007,
   AJ, 133, 2258
```

```
Schmidt, S. J., West, A. A., Burgasser, A. J., Bochanski, J. J., & Hawley, S. L.
  2010, AJ, 139, 1045
Schneider, A. C., Cushing, M. C., Kirkpatrick, J. D., et al. 2015, ApJ, 804, 92
Scholz, R. D. 2010a, A&A, 510, L8
Scholz, R. D. 2010b, A&A, 515, A92
Scholz, R. D., Bihain, G., Schnurr, O., & Storm, J. 2011, A&A, 532, L5
Siverd, R. J., Beatty, T. G., Pepper, J., et al. 2012, ApJ, 761, 123
Skrutskie, M. F., Cutri, R. M., Stiening, R., et al. 2006, AJ, 131, 1163
Smiljanic, R., Korn, A. J., Bergemann, M., et al. 2014, A&A, 570, A122
Soto, M. G., & Jenkins, J. S. 2018, A&A, 615, A76
Stephens, D. C., Leggett, S. K., Cushing, M. C., et al. 2009, ApJ, 702, 154
Taylor, M. B. 2005, in ASP Conf. Ser. 347, Astronomical Data Analysis
   Software and Systems XIV, ed. P. Shopbell, M. Britton, & R. Ebert (San
  Francisco, CA: ASP), 29
Thompson, M. A., Kirkpatrick, J. D., Mace, G. N., et al. 2013, PASP, 125, 809
Tinney, C. G., Burgasser, A. J., & Kirkpatrick, J. D. 2003, AJ, 126, 975
Tinney, C. G., Burgasser, A. J., Kirkpatrick, J. D., & McElwain, M. W. 2005,
    AJ, 130, 2326
Tinney, C. G., Kirkpatrick, J. D., Faherty, J. K., et al. 2018, ApJS, 236, 28
Torres, G., Fischer, D. A., Sozzetti, A., et al. 2012, ApJ, 757, 161
Tremblin, P., Amundsen, D. S., Chabrier, G., et al. 2016, ApJL, 817, L19
Tremblin, P., Amundsen, D. S., Mourier, P., et al. 2015, ApJL, 804, L17
Tremblin, P., Chabrier, G., Baraffe, I., et al. 2017, ApJ, 850, 46
Tremblin, P., Padioleau, T., Phillips, M. W., et al. 2019, ApJ, 876, 144
UKIDSS Consortium 2012, VizieR On-line Data Catalog: II/316
Valenti, J. A., & Fischer, D. A. 2005, ApJS, 159, 141
van Leeuwen, F. 2007, A&A, 474, 653
Wielen, R. 1977, A&A, 60, 263
Wright, E. L., Eisenhardt, P. R. M., Mainzer, A. K., et al. 2010, AJ, 140, 1868
Yurchenko, S. N., Barber, R. J., & Tennyson, J. 2011, MNRAS, 413, 1828
Zahnle, K. J., & Marley, M. S. 2014, ApJ, 797, 41
Zalesky, J. A., Line, M. R., Schneider, A. C., & Patience, J. 2019, ApJ, 877, 24
Zapatero Osorio, M. R., Martín, E. L., Béjar, V. J. S., et al. 2007, ApJ,
Zhang, Z., Liu, M. C., Best, W. M. J., et al. 2018a, ApJ, 858, 41
Zhang, Z., Liu, M. C., Best, W. M. J., Dupuy, T. J., & Siverd, R. J. 2021, ApJ,
Zhang, Z., Liu, M. C., Hermes, J. J., et al. 2020, ApJ, 891, 171
Zhang, Z., Liu, M. C., Marley, M. S., Line, M. R., & Best, W. M. J. 2021, ApJ,
  916, 53
Zhang, Z. H., Pinfield, D. J., Gálvez-Ortiz, M. C., et al. 2017, MNRAS,
  464, 3040
Zhang, Z. H., Pinfield, D. J., Gálvez-Ortiz, M. C., et al. 2018b, MNRAS,
  479, 1383
Zuckerman, B. 2019, ApJ, 870, 27
Zuckerman, B., Bessell, M. S., Song, I., & Kim, S. 2006, ApJL, 649, L115
```